TURUN
YLIOPISTO
UNIVERSITY
OF TURKU

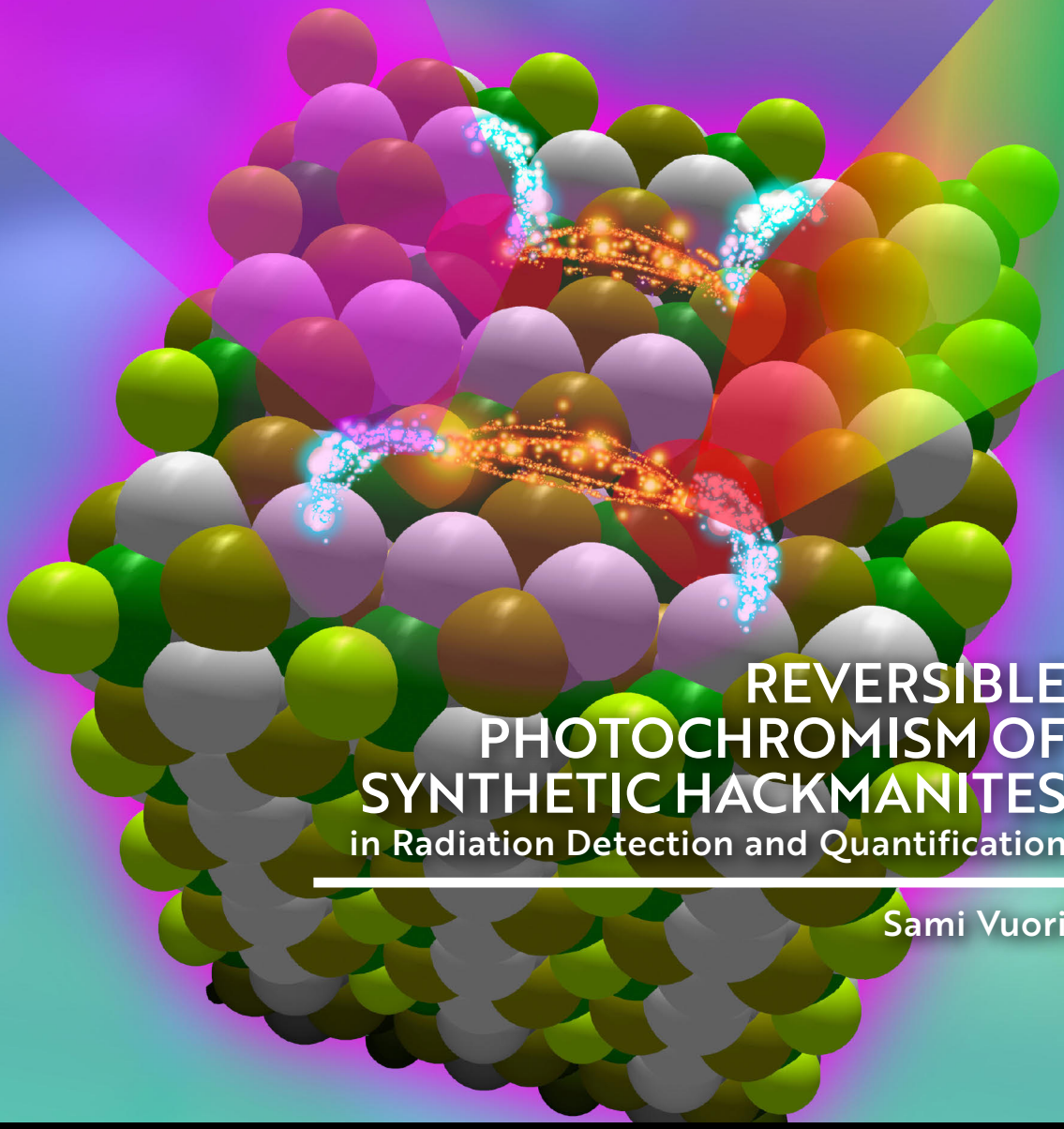

REVERSIBLE PHOTOCHROMISM OF SYNTHETIC HACKMANITES

in Radiation Detection and Quantification

Sami Vuori

TURUN YLIOPISTON JULKAISUJA – ANNALES UNIVERSITATIS TURKUENSIS
SARJA – SER. AI OSA – TOM. 691 | ASTRONOMICA – CHEMICA – PHYSICA – MATHEMATICA | TURKU 2023

TURUN
YLIOPISTO
UNIVERSITY
OF TURKU

REVERSIBLE PHOTOCHROMISM OF SYNTHETIC HACKMANITES

in Radiation Detection and Quantification

Sami Vuori

TURUN YLIOPISTON JULKAISUJA – ANNALES UNIVERSITATIS TURKUENSIS
SARJA – SER. AI OSA – TOM. 691 | ASTRONOMICA - CHEMICA - PHYSICA – MATHEMATICA | TURKU 2023

University of Turku

Faculty of Science
Department of Chemistry
Intelligent Materials Chemistry Research Group
Doctoral Programme in Exact Sciences (EXACTUS)

Supervised by

Professor Mika Lastusaari
Intelligent Materials Chemistry Research Group
Department of Chemistry
University of Turku
Turku, Finland

Reviewed by

Professor Klára Hernádi
Laboratory of Applied Nanomaterials
University of Miskolc, Miskolc, Hungary

Professor Andrew Beeby
Department of Chemistry
Durham University, Durham, UK

Opponent

Professor Adrian Finch
School of Earth & Environmental Sciences
University of St Andrews
St Andrews, UK

The originality of this publication has been checked in accordance with the University of Turku quality assurance system using the Turnitin OriginalityCheck service.

Cover Image: Sami Vuori

ISBN 978-951-29-9279-9 (PRINT)
ISBN 978-951-29-9280-5 (PDF)
ISSN 0082-7002 (Print)
ISSN 2343-3175 (Online)
Painosalama, Turku, Finland 2023

UNIVERSITY OF TURKU
Faculty of Science
Department of Chemistry
Intelligent Materials Chemistry Research Group
SAMI VUORI: Reversible Photochromism of Synthetic Hackmanites in Radiation Detection and Quantification
Doctoral Dissertation, 187 pp.
Doctoral Programme in Exact Sciences (EXACTUS)
June 2023

ABSTRACT

The subject of this thesis is centered on a mineral called hackmanite, also known as photochromic sodalite. It is found naturally in remote, mountainous places in Afghanistan, Pakistan, Greenland, Russia, Canada, and the United States. The natural mineral is costly to extract and – depending on the location – its optical properties and chemical impurities vary arbitrarily. Thus, it is not only more predictable, but also sustainable to synthesize the mineral in a laboratory from traceable reagents that contain known amounts of impurities. The synthesis route used in the experimental section in this work is a solid-state method where the reagents are mixed and heated in an oven at 850 °C and reduced with a hydrogen–nitrogen gas mixture.

The product, hackmanite ($Na_8Al_6Si_6O_{24}(Cl,S)_2$), shows properties including luminescence, persistent luminescence, and reversible photochromism upon exposure to UV, X, gamma, nuclear, or particle radiation. Hackmanite's photochromism is of particular interest since the coloration from white to pink can be reversed with visible light or heat, and this cycle can be repeated indefinitely. Hackmanite is thus able to react to its surrounding radiation atmosphere, and what makes the property even more interesting is that upon high-energy gamma radiation exposure the material "remembers" the exposure with a change of its color centers. In UV-induced coloration, the mechanism involves an electron transfer from a disulfide anion to a nearby chloride vacancy, which is a defect in the lattice due to the requirement of charge neutrality in the crystal. However, in X-ray- or other high-energy radiation-induced coloration the incident energies are so high that the coloration is caused by core-shell electrons and subsequent holes trapping after thermalization.

Due to the nature of the coloration process, hackmanite's application region spans from the high-energy gamma radiation to UV, however the material can also be used to detect visible light since the bleaching process (electrons returning to disulfide ions from the trap) occurs in the visible wavelength region. This property can be used for taking a photograph, as is shown in this thesis.

KEYWORDS: hackmanite, photochromism, radiation detection, dosimetry, photography

TURUN YLIOPISTO
Matemaattis-luonnontieteellinen tiedekunta
Kemian laitos
Älykkäiden materiaalien kemian tutkimusryhmä
Sami Vuori: Synteettisten hackmaniittien palautuva fotokromismi säteilyn havainnoinnissa ja määrityksessä
Väitöskirja, 187 s.
Eksaktien tieteiden tohtoriohjelma (EXACTUS)
Kesäkuu 2023

TIIVISTELMÄ

Tämän väitöskirjan aiheena on hackmaniitti-niminen mineraali, joka tunnetaan myös nimellä fotokrominen sodaliitti. Sitä esiintyy luonnossa syrjäisillä vuoristoseuduilla Afganistanissa, Pakistanissa, Grönlannissa, Venäjällä, Kanadassa ja Yhdysvalloissa. Luonnonmineraalin louhinta on kallista ja kestämätöntä, ja sen optiset ominaisuudet ja kemialliset epäpuhtaudet vaihtelevat satunnaisesti riippuen sijainnista. Näin ollen on ennakoitavampaa ja kestävämpää syntetisoida mineraalia laboratoriossa reagensseista, jotka ovat jäljitettäviä ja sisältävät tunnetut määrät epäpuhtauksia. Tämän työn kokeellisessa osassa synteesit toteutettiin kiinteän olomuodon menetelmällä, jossa lähtöaineiden seos kuumennetaan uunissa 850 °C:ssa ja pelkistetään vetytyppikaasuseoksella.

Tuotteella eli hackmaniitilla ($Na_8Al_6Si_6O_{24}(Cl,S)_2$), on ominaisuuksinaan luminesenssi, jälkiloiste ja palautuva fotokromismi altistuessaan UV-, röntgen-, gamma-, ydin- ja hiukkassäteilylle. Hackmaniitin fotokromismi on erityisen kiinnostava ominaisuus, sillä vaaleanpunaiseksi värjätty hackmaniitti voidaan palauttaa takaisin valkoiseksi näkyvällä valolla tai lämmöllä, ja tätä sykliä voidaan toistaa loputtomasti. Tämän ominaisuuden tekee vielä mielenkiintoisemmaksi se, että gammasäteilyaltistuksen yhteydessä materiaali ”muistaa” korkeaenergisen altistuksensa värikeskuksensa – joka on olennainen rakenne värjäytymismekanismissa – muutoksella. UV-värjäytymisessä mekanismi sisältää elektronin virittymisen disulfidianionista läheiseen kloridivakanssiin, mikä on kiteen varaustasapainovaatimuksen mukaisesti muodostunut hilavirhe. Röntgen- tai muun korkeaenergisen säteilyn aiheuttamassa värjäytymisessä energiat ovat kuitenkin niin suuria, että värjäytymisen aiheuttaa sisäkuorten elektronien ja aukkojen loukkuuntuminen termalisaation jälkeen.

Värjääntymisprosessin ansiosta hackmaniitin käyttöalue ulottuu korkeaenergisestä gammasäteilystä UV-säteilyyn, mutta materiaalia voidaan käyttää myös näkyvän valon havaitsemiseen, sillä haalenemisprosessi (elektronien palaaminen loukuista takaisin disulfidi-ioneihin) tapahtuu näkyvällä aallonpituusalueella. Tätä ominaisuutta voidaan käyttää valokuvaamisessa.

ASIASANAT: hackmaniitti, fotokromismi, säteilyn havainnointi, dosimetria, valokuvaus

Table of Contents

Abbreviations and symbols

□	a vacancy in a structure
a.u.	arbitrary unit
B3LYP	Becke, 3-parameter, Lee–Yang–Parr (a hybrid functional)
DOS	density of states
E	energy
EPR	electron paramagnetic resonance
I	intensity
PBE0	Perdew–Burke-Ernzerhof 0 functional (a hybrid functional)
PCB	periodic boundary conditions
PeL	persistent luminescence i.e. afterglow
PES	potential energy surface
(P)XRD	(powder) X-ray diffraction
RIJCOSX	resolution for identity approximation for Coulomb integrals and COSX numerical integration for Hartree–Fock exchange
RMS	root mean square
SCF	self consistent field
SVP	split valence polarization (a basis set)
UV	ultraviolet
V_{Cl}	a chloride vacancy (Kröger−Vink notation)
V_O	an oxygen vacancy in a structure (Kröger−Vink notation)
VUV	vacuum ultraviolet
XANES	X-ray absorption near-edge structure
XAS	X-ray absorption spectroscopy
XEOL	X-ray-excited optical luminescence
XPS	X-ray photoelectron spectroscopy
XRF	X-ray fluorescence
ZORA	zeroth order regular approximation

List of Original Publications

This dissertation is based on the following original publications, which are referred to in the text by their Roman numerals:

I **Vuori, S.**, Colinet, P., Norrbo, I., Steininger, R., Saarinen, T., Palonen, H., Paturi, P., Rodrigues, L. C. V., Göttlicher, J., Le Bahers, T., Lastusaari, M. Detection of X-Ray Doses with Color-Changing Hackmanites: Mechanism and Application. *Advanced Optical Materials*, 2021; 9: 2100762.

II **Vuori, S.**, Colinet, P., Lehtiö, J.-P., Lemiere, A., Norrbo, I., Granström, M., Konu, J., Ågren, G., Laukkanen, P., Petit, L., Airaksinen, A. J., Van Goethem, L., Le Bahers, T., Lastusaari, M. Reusable radiochromic hackmanite with gamma exposure memory. *Materials Horizons*, 2022; 9: 2773–2784.

III **Vuori, S.**, Byron, H., Norrbo, I., Tuomisto, M., Lastusaari, M. Photochromic photography with hackmanite obtained by large-scale synthesis. *Journal of Industrial and Engineering Chemistry,* 2023; 120: 361–373.

List of Related Publications not Included in the Thesis

Agamah, C., **Vuori, S.**, Colinet, P., Norrbo, I., Carvalho, J. M., Nakamura, L., Lindblom, J., Van Goethem, L., Emmermann, A., Saarinen, T., Laihinen, T., Laakkonen, E., Lindén, J., Konu, J., Vrielinck, H., Van der Heggen, D., Smet, P. F., Le Bahers, T., Lastusaari, M. Hackmanite—The Natural Glow-in-the-Dark Material. *Chemistry of Materials*, 2022; 32: 8895–8905.

Fang, W., Sairanen, E., **Vuori, S.**, Rissanen, M., Norrbo, I., Lastusaari, M., Sixta, H. UV-Sensing Cellulose Fibers Manufactured by Direct Incorporation of Photochromic Minerals. *ACS Sustainable Chemistry & Engineering*, 2021; 9: 16338–16346.

Colinet, P., Byron, H., **Vuori, S.**, Lehtiö, J-P., Laukkanen, P., Van Goethem, L., Lastusaari, M., Le Bahers, T. The structural origin of the efficient photochromism in natural minerals. *PNAS,* 2022; 119: e2202487119.

1 Introduction

Hackmanite is a naturally occurring mineral found in remote, mountainous places in countries such as Afghanistan, Greenland, Russia, Canada, and the United States. It is named after the Finnish geologist Victor Axel Hackman (1866–1941) [1,2], but currently the recommended form is *photochromic sodalite* according to the International Mineralogical Association [3]. Photochromism means that the mineral's color can be altered with light. Hackmanite is a variety of a tectosilicate mineral group called *sodalites*, and sodalite itself is also a name of a mineral with a chemical formula of $Na_8Al_6Si_6O_{24}Cl_2$. Hackmanite's general chemical formula is very close to sodalite by only the addition of small amount of sulfur, i.e. $Na_8Al_6Si_6O_{24}Cl_{2-\delta}S_{\delta/2}$, where δ varies between 0 and 0.25 depending on the literature source. [1,2,4–6] The disulfide ion is the key in the coloration process, as it has a valence electron bound in a way that ultraviolet light can excite it into a defect in the lattice, and this coloration property is the main topic of this work. Other sodalite minerals are e.g. haüyne ($Na_3Ca(Si_3Al_3)O_{12}(SO_4)$), nosean ($Na_8Al_6Si_6O_{24}(SO_4)\cdot H_2O$), and lazurite ($(Na,Ca)_8[(S,Cl,SO_4,OH)_2|(Al_6Si_6O_{24})]$), and while the chemical composition seems very different between the group members, they all share a mutual crystallographic tectosilicate group unit, which contains silicate tetrahedrons ($(SiO_4)^{4-}$). [7] Hackmanite's unit cell is shown in Figure 1.

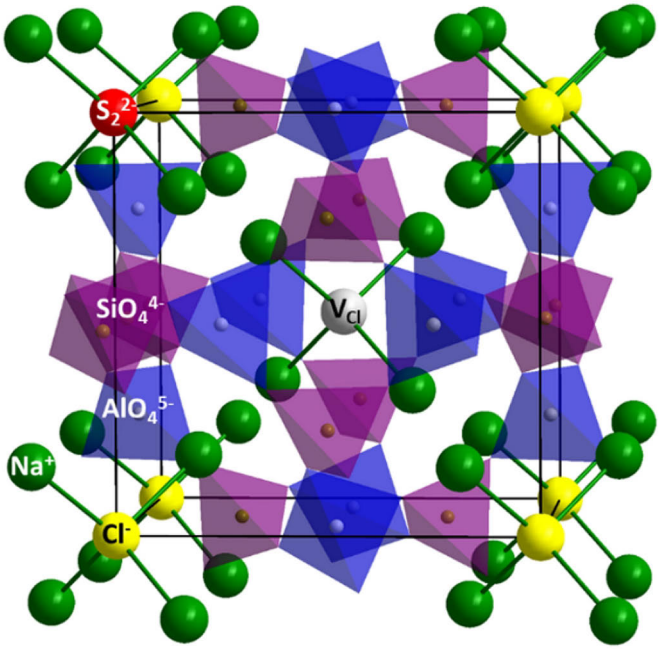

Figure 1. The unit cell of hackmanite, showing the disulfide dopant in red, and a chloride vacancy in gray, which are responsible for the coloration.

Hackmanite gained scientific interest in the 1950–1970s when Medved, Kirk, Doorn, Takeda, and Williams *et al*. reported about its optical properties. [8–13] After that, a UK-based research group led by Professor Mark Weller published compositional articles about the mineral in the early 2000s [6,14], but complete scientific resurgence occurred in the 2010s when Zahoransky *et al*. published their report about natural sodalites [15], followed by several papers about synthetic hackmanites from the research group led by Professor Mika Lastusaari in Turku, Finland. [3,16–22] During the past decade, significant progress has also been made in the development and refinement of computational methods regarding hackmanite. As a result of these advancements, they have particularly leveraged the understanding of hackmanite's structural and electronic properties to a new level. The simulations have proven to be a valuable complement to experimental techniques, providing insights and predictions that can be tested and verified through laboratory experimentation. While earlier studies on hackmanite have been on the structural and optical property side, the new openings in this field of study have been accompanied with scientific applications where hackmanite plays a key role. [21,23,24]

While the synthesis of hackmanite can be anything incorporating high temperatures, such as solid-state, microwave, or hydrothermal reaction routes

[3,6,8,12,14,16–20,22,25], the solid-state method is undoubtedly the most commonly used, which is the case in this work as well, since all synthetic samples were prepared using it. The method comprises mixing the starting materials (in pristine hackmanite's case only zeolite, sodium chloride, and sodium sulfate) gently, then heating them at 850 °C in air, and another time in a moderately reducing atmosphere at the same temperature. This particular reaction route is favoured because of its reliability, yielding consistent products and reproducible properties, especially reversible photochromism.

The main properties that make hackmanite interesting in terms of practical applications are photoluminescence, afterglow, and reversible photochromism. These are all phenomena where the result is clearly visible by a naked eye but are also quantifiable with instrumentation such as spectrometers or even a digital camera. Photoluminescence is a term for a phenomenon where the material emits light spontaneously as a result of absorbing high-energy radiation, typically ultraviolet. In hackmanite, photoluminescence emission occurs with excitation wavelengths throughout the whole UV range. [18,26] Particularly in natural hackmanite, UVA excites the orange emission from sulfur (Figure 2a), whereas shorter wavelengths give rise to activation of the titanium–oxygen vacancy system which is responsible for the more blue luminescence and afterglow (Figure 2b).

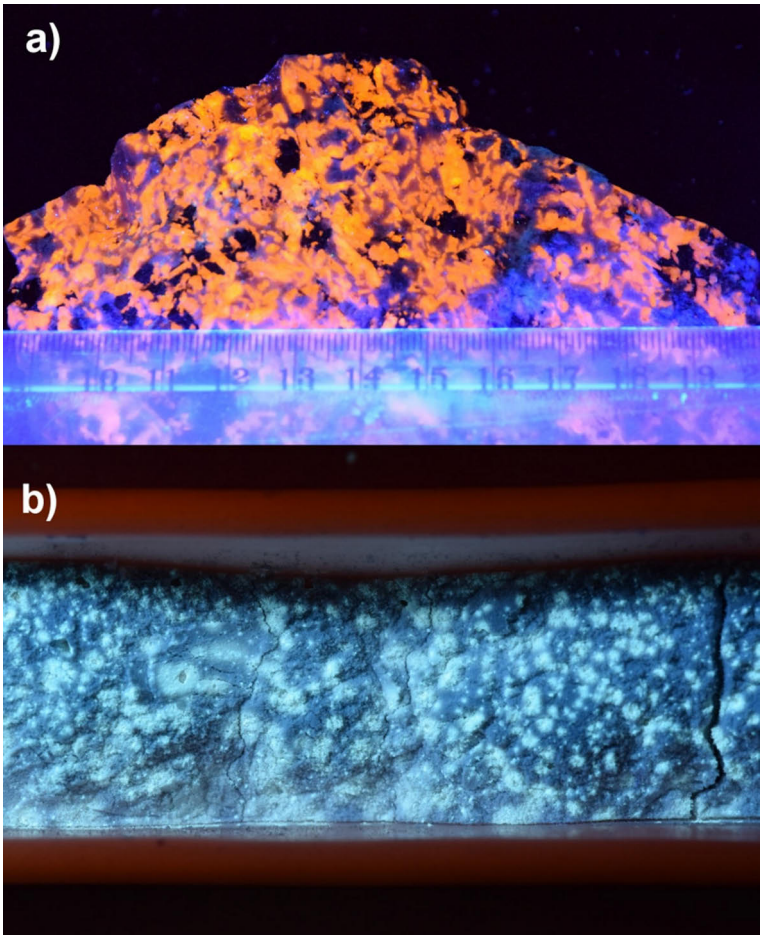

Figure 2. **a)** A natural hackmanite specimen from Mt. St. Hilaire, Canada exposed to 365 nm UVA, showing hackmanite's characteristic, strong orange photoluminescence. **b)** Synthetic hackmanite's luminescence under 302 nm UVB exposure.

Upon UV excitation, another important optical property is activated, namely photochromism. [3,7–9,11–13,15,16,18,19,23–25,27–31] In hackmanites, photochromism is a phenomenon where the material changes its color to pink after absorbing UV photons. The color can be reverted to original off-white by exposing the material to visible light or heat [19], after which it is once again ready to change to pink upon UV excitation. For the practical applications, this reversible coloration is of high importance since it renders easily-synthesizable artificial hackmanite a sustainable material – together with the fact that it contains only abundant elements; if the material gets damaged or is not needed any more, hackmanite can be disposed of as general household waste.

2 Literature review

The literature review consists of the scientific foundation of the work, including the following chapters and sections:

1. Theory of the solid-state synthesis method, which was the method used in synthesizing the samples in the experimental section of this work. Other synthesis methods are outside the scope of this thesis and are thus excluded.
2. An introduction to reversible photochromism and its industrial and consumer applications.
3. Information about several materials that exhibit reversible photochromism, including natural and synthetic.
4. The mechanism of tenebrescence in hackmanites explaining the quantum physical and chemical processes that lead to the coloration and subsequent bleaching of the material.
5. Information about coloration depth and its relation to the traps in the crystal lattice, with a special focus on hackmanite.
6. Introduction to high-energy radiation including X-, gamma, alpha, and beta radiation, their absorption and scattering, scintillation and XEOL phenomena, high-energy radiation detection methods, minerals with photochromism upon high-energy radiation, and lastly an overview of current passive detection materials for high-energy radiation. In this sense, passive means that the material does not need electricity to generate a response, and thus the signal is an integral of the whole radiation dose.

2.1 The solid-state reaction method

Many inorganic photochromic materials, including hackmanite, are easily synthesized via the solid-state reaction route, which involves chemical reactions that occur within the boundaries of the reactants and products being in a solid phase throughout the whole synthesis. These reactions are of particular interest to materials

scientists because they can be used to synthesize a wide variety of materials with unique optical properties, to which photochromism belongs.

Solid-state reactions can occur via several different routes, including diffusion [32], phase transformation (nucleation, growth, and impingement) [33–35], and solid-state metathesis [36,37]. In diffusion-controlled solid-state reactions, the reaction occurs through the diffusion of reactants into each other. This can occur either homogeneously or heterogeneously, and the rate of the reaction is determined by the diffusion coefficient of the reactants in the solid state. In this, several interfaces of different materials form a joint where the diffusion profile of each interface forms a Gaussian distribution related to each other. After a certain time, the diffusion has proceeded to a point where a finite amount of each substance has diffused into the other, and vice versa. At high temperatures the diffusion rate is increased, i.e., at room temperature while there is a non-zero rate, there is practically no reaction between substances that have a melting point of several hundreds of degrees in Celsius. However, the temperature must not reach the melting point of any of the materials, as the Tammann rule states that the most optimal temperature for heat-generated point defects in a solid is ¾ of the melting temperature. [32–35,38,39]

Figure 3 shows a simplistic overview of the solid-state reaction route, where the grinding lets the starting material powder particles distribute evenly in the mixture mass, and heating induces a reaction between the interfaces, the reaction rate depending on the size of the surface joints. When the sample is ground and heated again, a pure phase is obtained.

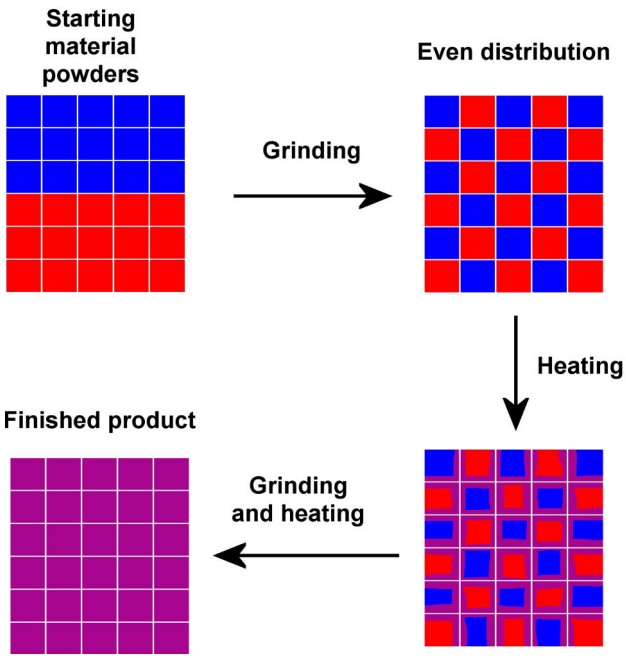

Figure 3. A simplistic overview of the solid-state process, which involves mixing the starting materials to form an even distribution, then heating and repeating the process until the finished product is uniformly the desired phase.

Phase-transforming solid-state reactions occur when the reactants undergo a phase change during the reaction. For example, a solid-state reaction between a metal oxide and a reducing agent may result in the reduction of the oxide to a metal. In this case, the reaction occurs via a phase transformation from an oxide to a metal. One example is a solid-state reduction reaction of magnetite (iron oxide) or titanomagnetite to elemental metals using hydrogen or methane. [40–42]

Solid-state metathesis reactions occur when two solid-state compounds react to form two new solid-state compounds, which can be solid solutions with a high thermodynamic stability. This type of reaction is commonly used in the synthesis of complex materials, such as borides, silicides, pnictides and chalcogenides, or nitridoborates, carbodiimides, tetracyanoborates, tetracyanamidosilicates, and carbon-nitride materials. [36,37]

There are a number of factors that can influence the rate and extent of solid-state reactions, including temperature, pressure, and the nature of the reactants, including the possible reducing atmosphere. For example, high temperatures can accelerate the diffusion of reactants and increase the rate of the reaction. Pressure can also have an effect on the reaction, particularly in cases where the reaction is accompanied by a change in volume, leading to a change in interatomic distances. [43,44]

Solid-state reactions have been extensively studied in a variety of materials systems, including oxides, nitrides, and intermetallics. One example is the solid-state reaction between aluminum and titanium oxides leading to a formation of their solid solution. [45–47]

2.2 Reversible photochromism

Reversible photochromism is a property of matter where it changes its color upon photon irradiation. Although the word "photon" renders the definition vague and implicitly includes photons of all energy, typically the phenomenon has been researched in materials with excitation in the UV range, although not limited to it. The reversibility of the property means that there is no irreversible damage inflicted on the atomic level, meaning that the material does not proceed to a state where reversing the phenomenon to original would require substantial energy barrier crossing. Hackmanite shows this type of reversible coloration from white to pink, as depicted in Figure 4.

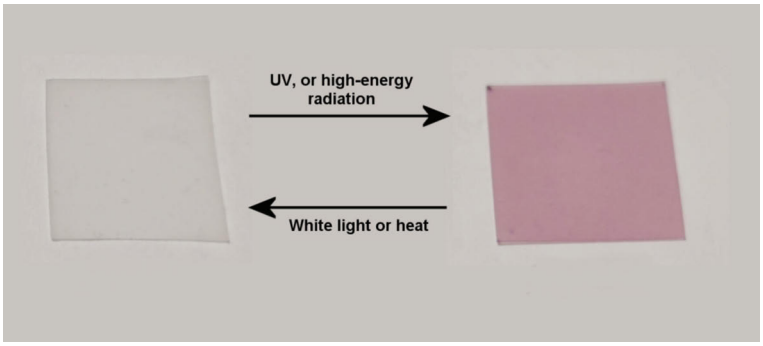

Figure 4. A silicone film with 20% of hackmanite powder. When the film is exposed to UV or high-energy radiation, it changes its color from white to pink due to hackmanite's remarkable coloration ability. When the film is kept in light or given heat, it reverts to its original white color.

Currently, photochromic materials are used in glasses, eyewear, building materials, information storage devices, and windows (including automotive), where their observed color darkens in response to the presence of e.g. UV radiation that is found in sunlight. In windows and glasses, darkening provides a number of benefits, including reducing glare, improving contrast, and especially protecting against UV radiation. In addition to their practical benefits, photochromic materials also have aesthetic value, as they allow for the creation of unique color-changing designs. [48–52]

Photochromic glasses and windows have been developed using a number of different materials, including silver halides, organic dyes, and metal oxides. One of the most commonly used materials are silver halides (e.g. AgBr), which undergo a reversible photochemical reaction in response to UV radiation. When exposed to UV radiation, the silver halides form small clusters of metallic silver, which cause the glass to darken. This darkening is reversible, meaning that the glass will return to its clear state when the UV radiation is removed. The windows can also be made into flexible shapes, e.g. for use as motorcycle visors. [53–58]

Organic dyes, e.g. diarylethene, fulgide, azobenzene, spiropyran, spirooxazine, benzopyran, and naphthopyran and organic-inorganic hybrid materials (organic molecule adhesion onto e.g. pores of a silica matrix) are another commonly used material in photochromic glasses and windows. These dyes absorb UV radiation and undergo a photochemical reaction (e.g. photocyclization, trans-cis isomerisation, or heterolytic cleavage or bond scission) that results in a change in color. The use of organic dyes allows for a wider range of colors to be produced, as well as a great control over the rate of color change. However, their disadvantage is the finite cycles the coloration can undergo. [59–62]

The production of photochromic glasses and windows involves a number of steps, including the deposition of the photochromic material onto the glass or plastic substrate, the incorporation of a protective layer to prevent scratching, and the addition of a UV-blocking layer to provide protection against harmful UV radiation, although with many photochromic materials the absorption of UV is enough to act as the UV protection layer, depending on their optical density in the UV region. [57]

2.3 Materials exhibiting reversible UV coloration

In addition to hackmanite, some reversibly colorable, laboratory-synthesizable inorganic materials that have been reported are e.g.

1. $Sr_3YNa(PO_4)_3F:Eu^{2+}$, synthesized by the solid-state reaction method using $SrCO_3$, Na_2CO_3, $(NH_4)_2HPO_4$, SrF_2, and Ln_2O_3 (Ln = Y, La–Nd, Sm–Lu) as starting materials. After grinding the materials, they are preheated at 600 °C for 2 h in air atmosphere, after which the product is reground and reduced at 1100 °C for 3 h in a 15%/85% H_2/N_2 atmosphere. After exposure to 254 nm UV, the reflectance spectrum reveals absorption bands at 422 and 606 nm, which renders the color of the irradiated material from white to cyan. [63]
2. $Na_{0.5}Bi_{2.5}Nb_2O_9:Sm$, synthesized using Na_2CO_3, Bi_2O_3, Nb_2O_5, and Sm_2O_3 as starting materials. The solid-state synthesis involves mixing the powders with alcohol and heating at 900 °C for 4 h in air. After the first heating, the product is mixed with alcohol and polyvinyl alcohol (PVA) binder, and

finally pressed into pellets sized 15 mm in diameter and 1 mm in thickness. The last heating is conducted at 1100 °C for 2 h. The color change was reported to occur under sunlight, where the original green coloration turned into dark gray. The reflectance spectrum shows a broad absorption band peaking at 458 nm. [64]

3. $Sr_3GdNa(PO_4)_3F:Eu^{2+}$, where the starting materials $SrCO_3$, Na_2CO_3, $(NH_4)_2HPO_4$, SrF_2, and Ln_2O_3 are given the same solid-state treatment as in 2. The coloration properties are also the same. [65]
4. $Mg_4Ga_8Ge_2O_{20}:Cr^{3+}$ (MGG:Cr), synthesized from MgO, Ga_2O_3, GeO_2, Cr_2O_3, and H_3BO_3 (flux) by milling in an agate mortar and heated at 1100 °C for 2 h in air. After heating, the product was ground again and heated at 1400 °C for 6 h in air. Six compositions of MGG:*x*Cr where the *x* varied from 0.0005 to 0.02 showed increasing photochromism when the dopant concentration decreased; of all samples, the 0.0005 specimen showed the deepest rosy brown photochromism upon 280 nm UV irradiation. The reflectance spectra showed absorption bands at 350 and 550 nm. [66]
5. $KSr_2Nb_5O_{15}$, synthesized using a molten salt synthesis method using $SrCO_3$, Nb_2O_5, and KCl, along with Bi_2O_3 as a material for aiding the sintering process. After ball-milling the powders for 10 h in alcohol, the dried mixture was granulated using polyvinyl alcohol and pressed into pellets of 12 mm in diameter and 1.6 mm in thickness. The first heating was conducted for 3 h at 650 °C in air to remove the PVA binder, and subsequently heated at 1250 °C for 2 h in air, and finally at 1350 °C for 2 h in a flowing oxygen atmosphere. The resulting products showed a coloration reaction under 395 nm irradiation, from green to darker shade of green. The irradiated sample showed a reflectance minimum at 532 and 689 nm. [67–70]
6. $BaMgSiO_4$, a material with a stuffed tridymite structure that can be synthesized via solid-state reaction route using $BaCO_3$, $MgCO_3$, SiO_2, metal oxides (dopants), and H_2BO_3 (flux). The powder mixture is ground in a mortar with ethanol and pressed into pellet (diameter 20 mm, thickness 5 mm) after drying. The pellets are then heated in a 5%/95% (H_2/Ar) reduction atmosphere at 1250 °C for 4 h. The product shows deep pink reversible coloration that changes from white under blue light (405 nm) or UV (365 nm) irradiation. The absorption band is centered at 523 nm. [71,72]
7. $Sr_2SnO_4:Eu^{3+}$, synthesized via the solid-state reaction route using $SrCO_3$, Eu_2O_3, and SnO_2 powders as the starting materials and mixed with the help of ethanol. The mixture is heated at 800 °C for 1 h in air, and then pressed into pellets and heated again in air at 1100–1600 °C for 5 h. When the

products are subjected to 254 nm UV radiation, they show white-to-purple reversible coloration with an absorption band located at 578 nm. [73–75]

8. $Ba_{10}(PO_4)_6ClF:Eu^{2+},Gd^{3+}$, synthesized by mixing $BaCO_3$, $(NH_4)_2HPO_4$, $BaCl_2 \cdot 2H_2O$, BaF_2, Eu_2O_3, and Gd_2O_3 and using solid-state reaction as the synthesis method. The mixture of these powder is ground in an agate mortar and then heated at 1100 °C in a 15%/85% (H_2/N_2) atmosphere for 3 h. The products showed a color transition from white to pink after irradiation with 254 nm, and reverted to white with 532 nm laser, heat, sunlight, or ambient light. The absorption band in this material is located at 530 nm. [76] Also another haloapatite form, $Ba_5(PO_4)_3Cl:Eu^{2+},R^{3+}$ (R = Y, La–Nd and Sm–Lu), shows this reversible photochromism. [77]
9. WO_3 and MoO_3, which are synthesized as thin films by sublimating pure WO_3 or MoO_3 in high vacuum. The optimal coloration excitation wavelength is in the UVA range, and the resulting broad absorption band peaks at in the near-infrared region (800–1050 nm depending on the film's properties). [78–82]
10. V_2O_5, which is synthesized by pressing pure V_2O_5 into a pellet and heating it at 500–580 °C for 4–15 h in air or flowing O_2 atmosphere, or by preparing it as thin films via wet chemistry methods. The photochromism can be induced with UV or visible light laser, which turns the material's color to pale blue, which is a result of a broad absorption band peaking at ~700 nm. [83–85]
11. Other metal oxide and hybrid materials, including Ag/TiO_2 [86], $W\text{-}TiO_2$ [87], TiO_2 / $Ni(OH)_2$ [88], Nb_2O_5 [89], and WO_3–TiO_2–ZnO [90,91].

As can be seen from the synthesis procedures from the materials listed above, solid-state reaction route is mostly used when producing inorganic photochromic materials. Although there may currently still be an abundance of the elements found in the aforementioned materials, most of them pose challenges when considering them to be used in practical applications. As for natural materials, tugtupite ($Na_8Al_2Be_2Si_8O_{24}Cl_2$) (photochromism shown in Figure 5a and c) contains beryllium, which is a toxic element, and the reversal of its coloration is very slow compared to hackmanite, and its synthesis is also very difficult. Although scapolite ($[Na,Ca]_4Al_3Si_9O_{24}[Cl,CO_3]_2$) consists of non-endangered elements, its reversal to the original color proceeds spontaneously quickly in room temperature after irradiation. Figure 5b and d shows polished scapolite samples where the characteristic blue photochromism is clearly visible. [21,92,93]

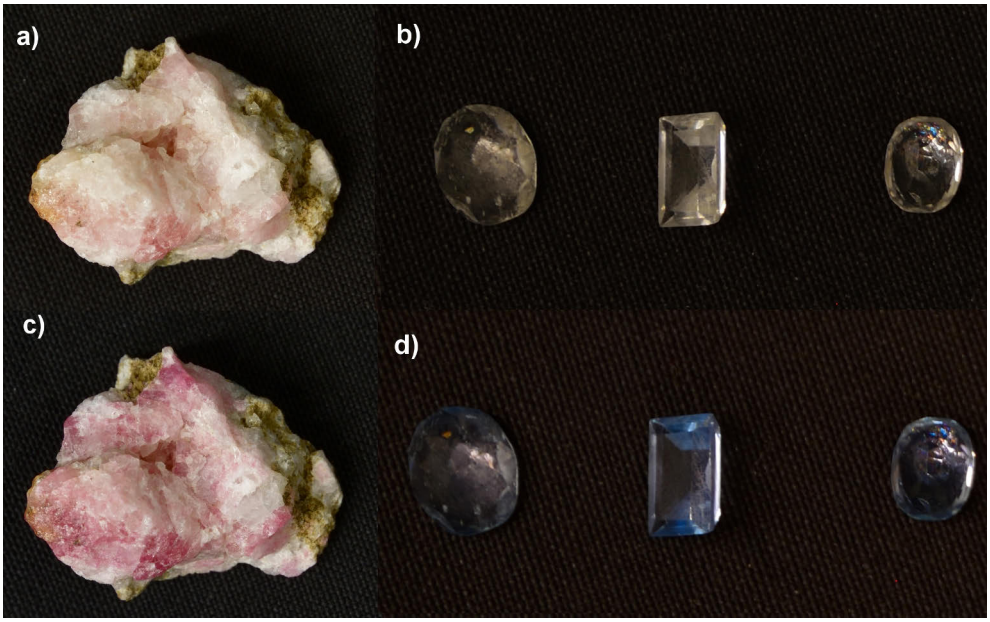

Figure 5. **a)** Tugtupite and **b)** scapolite rocks before and **c)**, **d)** after exposure to 254 nm UV, exhibiting reversible photochromism.

Most of the listed photochromic materials contain toxic and/or rare or expensive elements, such as strontium, tin, europium, bismuth, niobium, samarium, gallium, germanium, barium and/or gadolinium etc. [94] In addition to these, some other notable inorganic reversibly photochromic materials are also Zn_2GeO_4:Eu [95], $CaAl_2O_4$:Eu,Nd [96], $ZnGa_2O_4$:Bi [97], sapphire [98] and diamond [99,100].

2.4 Mechanism of tenebrescence in hackmanite

In hackmanite's photochromism, often referred to as tenebrescence (from Latin *tenebrae*, "darkness") [101], the coloration is induced with UV radiation and reverting it to its original state is achieved with visible light – or heat.

The mechanism of tenebrescence involves a system with a dopant amount of sulfide anions S_2^{2-} and chloride vacancies (V_{Cl}). Compared to sodalite, introducing a sulfide ion with a valence state of −II in hackmanite creates a charge imbalance, which must be neutralized by having one chloride ion (valence −I) left out of the structure due to the aliovalent nature of the two species. The resulting sulfide ion then acts as an electron donor for the chloride vacancy upon exposure to UV radiation. [3,8,9,12,16–19,21,23,24] Both the S_2^{2-} and V_{Cl} are located in the centers of their respective Na_4 tetrahedra in the sodalite lattice. [6,14,21,23,24,102] When an electron lands on the V_{Cl}, the tetrahedron reorganizes to form a metastable

geometry by contracting itself slightly due to the trapped electron attracting the Na^+ ions, whereas the tetrahedron around the S_2^- expands slightly compared to its initial state due to the loss of one Na^+-attracting electron. [21] The V_{Cl}^- now acts as a color center by absorbing photons at ~540 nm and is thus the origin of the observed purple or pink coloration of the material. Mechanistically, the electronic transitions of the system proceed as depicted in Figure 6, and in [19,21,23,24]:

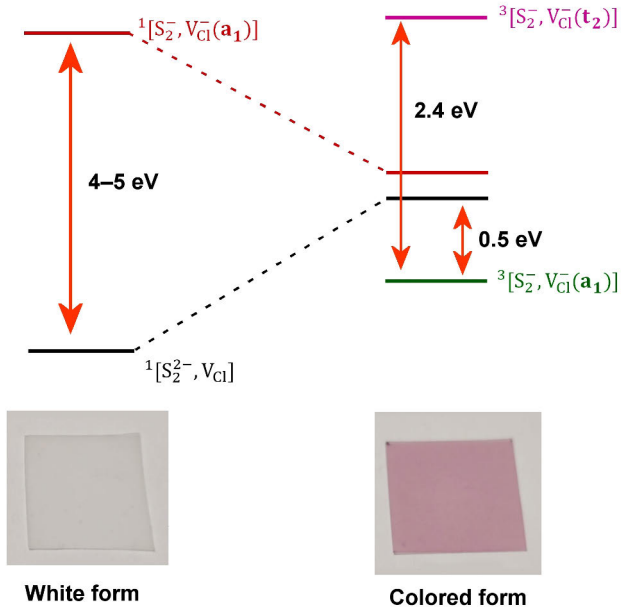

Figure 6. The mechanism of tenebrescence in hackmanites, explained in detail below.

1. A UV photon (energy ~4−5 eV) excites a valence electron in the S_2^{2-} ion, and the electron then lands on the V_{Cl}. This means an electronic transition from $^1[S_2^{2-},V_{Cl}]$ to $^1[S_2^-,V_{Cl}^-(\mathbf{a_1})]$.
2. The Na^+ tetrahedron containing the V_{Cl} in its center reorganizes to form a metastable triplet state, $^3[S_2^-,V_{Cl}^-(\mathbf{a_1})]$, which now becomes the color center's ground state. The reorganization is due to the trapped electron attracting the Na^+ ions, leading to a minute contraction of the tetrahedron.
3. The color center absorbs a photon of energy ~2.4 eV (~540 nm), which excites the electron to the V_{Cl}'s excited state $^3[S_2^-,V_{Cl}^-(\mathbf{t_2})]$. This leads to the observation of the material's coloration, which is strong due to the allowed $A_1 \rightarrow T_2$ transition.

4. When the electron deexcites to the ground state $^3[S_2^-,V_{Cl}^-(\mathbf{a_1})]$, this route also crosses the probability density of the original electronic state $^1[S_2^{2-},V_{Cl}]$ although by a small degree due to weak coupling of the two systems. Still, there is some probability for this to occur, and when it happens, the geometry reorganizes again to conform to the global PES minimum of the system, leading to the original, non-colored white form.
5. The bleaching can also be induced by heating the sample, which increases the probability of the electronic states to overlap as a function of temperature. As a result, the required energy for bleaching the material with heating is lower than with visible light; only ~0.5 eV since there is no need for the discrete amount of energy for the electron excitation first into the excited triplet state and then to the original electronic state. [19]

2.5 Coloration depth and traps

Coloration depth of opaque materials can be measured with radiant reflectance spectroscopy, which gives information about the absorption features in the material. Preferably, the measurement is carried out in an integrating sphere where only the sample is illuminated with a calibrated light source. An integrating sphere enables the collection of all reflected light, losing all directional information of the reflection. The inner lining of the integrating sphere is a Lambertian [103] surface, which reflects the light coming from the sample uniformly inside the hollow cavity. The detector coupled to an integrating sphere then collects this light. In hackmanite, the coloration is measured in the visible range since the absorption band is centered around ~540 nm. The coloration depends on the total UV photon fluence, but in addition to this, the observed color depth of hackmanite is dependent on the color center concentration, which can be estimated by using Smakula's formula. [30,104] This equation, however, is originally developed for color center absorption bands (F bands) with a Lorentzian shape [105], thus a more accurate, Lorentz field-corrected equation introduced by van den Brom *et al*. (Eq. 1) is preferred [3,106]:

$$fN_c = 5.0 * 10^{15} * \alpha_{\mathrm{m}}(\mathrm{cm}^{-3}) \qquad \text{(Eq. 1)}$$

where f = oscillator strength (0.3 atomic units for hackmanite [23]), N_c = color center concentration, α_m = maximum value of the absorption coefficient α, which is calculated using Beer–Lambert law from a fully colored sample. [106] The color center concentration can be converted between volume and mass with hackmanite's density, which is essentially sodalite's density 2.3 g cm^{-3} [7].

An additional way to estimate the color center concentration is to use mass magnetization measurements σ (unit A·m^2 kg^{-1}) of the white and colored forms by

subtracting the former with the latter and dividing it with the magnetic moment of the triplet state $^3[S_2^-,V_{Cl}^-(\mathbf{a_1})]$, i.e. 2.1 Bohr magnetons μ_B [19]:

$$N_c = \frac{\sigma}{\mu_B} = \frac{[A*m^2kg^{-1}]}{\left[\frac{J}{T}\right]} = \frac{[A*m^2kg^{-1}]}{\left[\frac{kg*m^2s^{-2}}{kg*s^{-2}A^{-1}}\right]} = [kg^{-1}] \quad \text{(Eq. 2)}$$

Eq. 2 possibly produces less variation in different samples with the same amount of color centers since it excludes the optical characteristics of the sample: mainly the size of reflecting crystal surfaces and their orientation. Some reported color center concentrations using Eq. 1 and 2 are in the order of 10^{16} g^{-1} (synthetic $Na_8Al_6Si_6O_{24}(Cl,S)_2$) [19], 10^{17} g^{-1} (natural hackmanite) [3], 10^{18} cm^{-3} (synthetic Cl, Br, and I sodalites) [30].

2.6 X-rays, nuclear and particle radiation

2.6.1 X-rays and gamma rays

There is no distinctive division between X-ray and gamma ray photons, however a typical classification of X-rays is that they originate from electrons, whereas gamma rays originate from nuclei. The two types' energy ranges overlap in the electromagnetic spectrum, and as the photons' qualities are described using the Planck–Einstein relation $E=h\upsilon$, they are energetically indistinguishable from each other: if the origin of the photon is not known, a photon of e.g. 80 keV cannot in any way be determined to be a gamma or X-ray photon. However, as a convention, X-rays have been described to occupy the electromagnetic spectrum's range of 0.01–100 Å, or 10^6–100 eV in quantum energy, but the limits vary between sources from different times. X-rays can be emitted from the deceleration of electrons, resulting in broad, continuous spectrum or characteristic emission. The former, *bremsstrahlung* (German for "braking radiation") is a phenomenon in which a charged particle is accelerated or decelerated as it interacts with the electric field of another charged particle, such as an atomic nucleus. This acceleration or deceleration causes the charged particle to emit electromagnetic radiation in the form of photons, which can be detected and measured. The working principle of synchrotrons' and cyclotrons' adjustable X-ray energies are based on bremsstrahlung: the desired energy can be achieved by simply monochromatizing the beam. [107,108]

In detail, bremsstrahlung radiation is produced when a charged particle, such as an electron, passes near a charged nucleus or other charged particle and experiences a change in direction due to the electromagnetic force. As the charged particle changes its direction, it emits radiation in the form of photons, which have energy

proportional to the energy lost by the charged particle as it interacts with the electric field of the nucleus. [107,108]

Bremsstrahlung radiation is important in a variety of contexts, including in medical imaging, where it is used in X-ray machines to produce images of the human body. It is also an important process in astrophysics, where it can be responsible for the emission of high-energy photons from sources such as supernova remnants and black holes. [109,110]

Another X-ray emission route is the abrupt absorption of X-rays photons, leading to the excitation or ionization of core electrons. When an electron is excited, an X-ray photon is emitted when the resulting hole is filled with an electron from a higher orbital energy level, i.e. the energy of the emitted X-rays is equal to the energy difference between the initial and final energy levels of the electron. This leads to characteristic radiation, which manifests itself as sharp peaks in the X-ray region of the electromagnetic spectrum. [108,111]

The characteristic X-ray emission spectrum of an element is unique and can be used to identify the element present in a sample. This is because the energy levels of the electrons in each element are specific to that element, meaning that the energy of the emitted X-ray is also specific to that element. By measuring the energies of the X-rays emitted from a sample, the elements present in a sample can be determined; this method is called X-ray fluorescence spectroscopy. [108]

Under the aforementioned classification, a gamma ray is a quantum of electromagnetic radiation emitted from an event where the atomic nucleus undergoes a transition from a higher energy level to a lower one. It can occur by nuclear fission, α or β particle decay, or by orbital electron capture, if the daughter nuclide is left to an excited state. [108,111]

2.6.2 Alpha and beta radiation

Alpha radiation is a type of ionizing radiation that is made up of positively charged particles called alpha particles, which are made up of two protons and two neutrons, also called doubly ionized helium nuclei (He^{2+}). Alpha particles are emitted by decay of certain types of radioactive materials, most notable probably being ^{241}Am, which is used in ionization smoke detectors. Alpha particles have a relatively low penetration power and are not able to pass through e.g. paper or clothing. However, they can be harmful if ingested or inhaled, as they can damage cells and tissues in the body. Alpha radiation is mostly emitted by heavy elements, such as uranium and plutonium via radioactive decay. It is also emitted by some types of particle accelerators and nuclear weapons. [108,112–114]

Beta radiation is a type of ionizing radiation that is made up of high-energy electrons or positrons, which are emitted by certain types of radioactive materials as

they undergo radioactive decay, e.g. ^{18}F, ^{137}Cs and ^{32}P. Beta particles are smaller and more penetrating than alpha particles, and can pass through paper, clothing, and some types of shielding materials. Like alpha particles, beta particles can be harmful if ingested or inhaled, as they can damage cells and tissues in the body. However, the penetration power of beta particles makes them more harmful than alpha particles when they are externally exposed to the body. Usually, beta radiation occurs in lighter radioactive elements, such as carbon and tritium. [108,115]

2.6.3 Absorption and scattering

X- and gamma rays are classified as radiation qualities capable of completely detaching an electron from its nucleus. The energy needed to produce an ion pair has been experimentally tested to be 34 eV, i.e. energies equivalent or higher than this give rise to the production of ion pairs. [111,116,117] Sometimes, the liberated electron may have enough energy to induce other ionizations in the material, leading to a cluster of ions and subsequent reactions until all energy has been lost in the resulting processes. A rule of thumb in the absorption of X-rays and gamma rays is that the higher the energy, the less the absorption when the elemental composition of the material is constant. However, a spectrum with photon energy as the x axis and the absorption in the y axis shows an abrupt discontinuity in the data points due to the discrete nature of electron energy levels leading to an absorption edge. In solid-state materials, the amount of absorption can be expressed using a physical quantity, mass attenuation coefficient, μ with units in $cm^2\ g^{-1}$ [118]. Figure 7 clarifies the matter with a plot of mass attenuation coefficient as a function of energy: at ~2.8 keV there is a sudden change in the attenuation due to the presence of Cl, which has a K edge (from the X-ray notation where K signifies the innermost electron shell) at that energy [119]. This means that at ~2.8 keV the X-ray energy is higher than the binding energy of Cl's K-shell electrons, which gives rise to their excitation. Sulfur has a K edge at ~2.5 keV [119], but it does not show in the image due to its low relative amount compared to the overall molar mass of hackmanite. Hackmanite's other elements' absorption edges (Na K edge at 1.1 keV, Al ~1.6 keV, Si ~1.8 keV, and O ~0.5 keV [119]) also do not show since their absorption edges lie outside the plotted region in the graph.

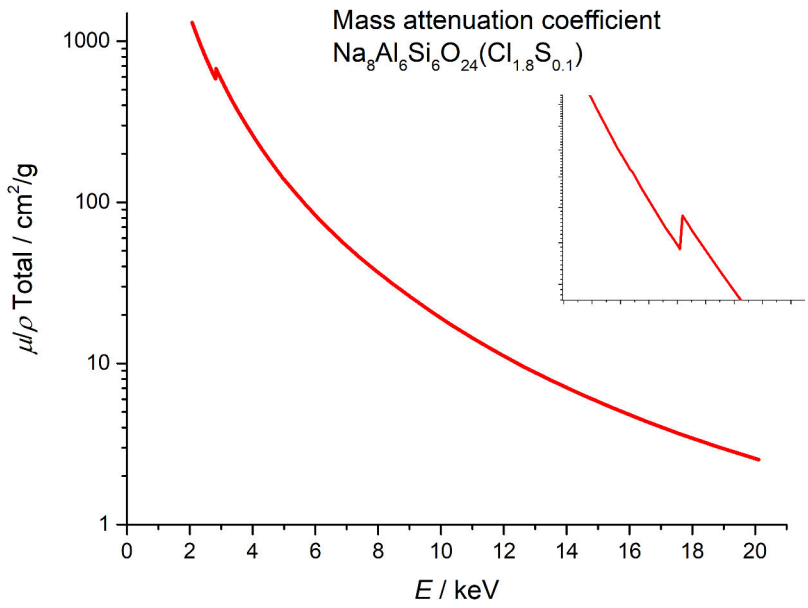

Figure 7. Mass attenuation coefficient of hackmanite as a function of energy. Inset: the absorption edge region zoomed in. [118]

A general rule is that the higher the element's Z is, the better it absorbs radiation with the inverse cube relation Z^3/E^3 where E = photon energy. [120] This is due to more dense packing of the atoms, which in turn increases the probability of a photon hitting an atom. The interaction types are (from [108,111,121,122]):

1. Photoelectric absorption leading to the excitation of an electron when the energy of the X-ray or gamma ray photon is transferred to an electron in the atom, causing the electron to be ejected from its orbit. This process is the dominant mechanism of absorption for low-energy X-rays. The probability of absorption depends on the energy of the X-ray and the atomic number of the material, with higher atomic numbers leading to greater absorption.
2. Compton (incoherent) scattering where part of the photon energy is transferred to a recoiling electron.
3. Thomson (coherent) scattering where the photon is deflected without it losing its energy.
4. Pair production where the annihilation of a high-energy photon leads to the formation of an electron and a positron.
5. Photodisintegration where the nucleus absorbs the energy of the photon.

The nature in which alpha particles are absorbed and scattered depends on the material they are interacting with, however in general they interact with matter with the following ways (from [108,123]):

1. As alpha particles pass through a material, they can ionize the atoms and molecules in their path due to the alpha particle being positively charged. This can cause the material to become electrically charged, which can then inflict damage in the matter or tissue.
2. Alpha particles can excite atoms in the material they are passing through, causing them to become unstable and emit secondary particles (such as electrons). These secondary particles can then interact with other atoms in the material, leading to further ionizations. The excitation is due to the alpha particle being positively charged, but not having enough influence to ionize the atom.
3. Coulomb scattering: The positive charge of the alpha particle causes it to interact with the negatively charged electrons in the material it is passing through. This can cause the alpha particle to scatter in different directions, losing energy in the process.

Because of these mechanisms, alpha particles have a very short range in most materials. For example, in air, alpha particles can travel only a few centimeters before being stopped. This makes alpha particles much less penetrating than beta or gamma radiation, but also much more damaging if they are inhaled or ingested, as they can inflict significant damage to living tissue.

2.6.4 Scintillation and XEOL

Scintillation is a phenomenon in which certain materials emit light when they are exposed to ionizing radiation, such as X-rays, alpha particles, beta particles, or gamma rays. This emission of light is known as scintillation light, and it is produced as a result of the interaction of the ionizing radiation with the material. The process can be simplistically described as follows [124–127], also depicted in Figure 8:

1. Ionizing radiation is absorbed by a scintillator material.
2. Core-shell electrons of an atom are excited, leading to the formation of electron–hole pairs and a cascade of secondary electrons and holes.
3. After a thermalization event, electrons and holes of the excited atoms recombine in a luminescence center in the bandgap, releasing energy in the form of a photon.

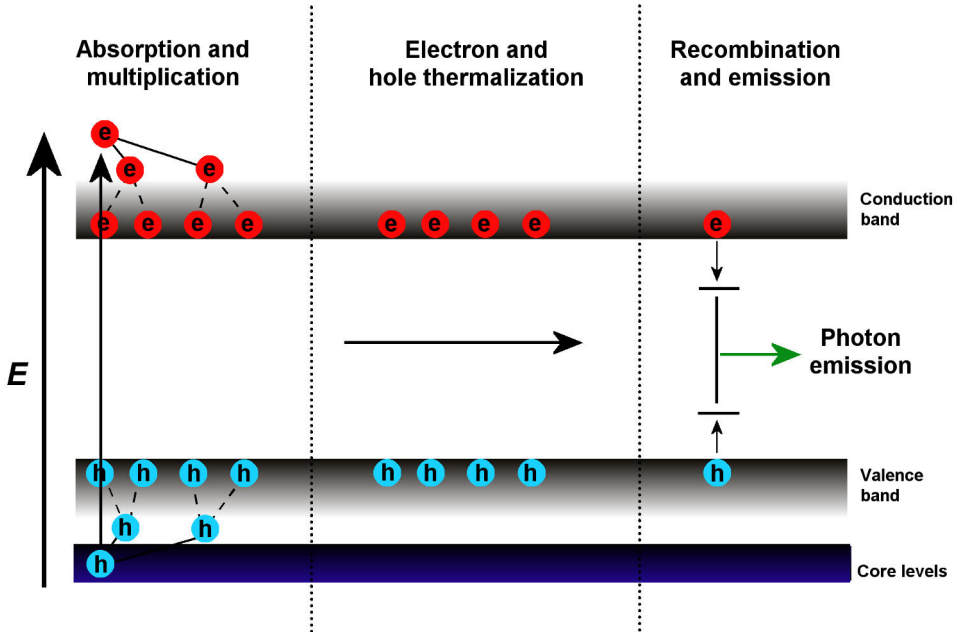

Figure 8. The mechanism of scintillation. When a scintillator is exposed to high-energy radiation, a core-level (e) electron is excited or ionized leaving a hole (h), which leads to the multiplication of both charge carriers due to collisions inside the material. After thermalization the two recombine in a luminescence center, and a photon is emitted.

The light can then be detected by a photosensor, such as a photomultiplier tube or a silicon photomultiplier, which converts the light into an electrical signal that can be measured and analyzed.

Scintillation creates a number of electron–hole pairs that depends on the initial incident photon energy, with higher energies producing more pairs. In XEOL – which is essentially a technique where scintillation of the material can be used to study its optical properties upon X-ray irradiation – the creation of electron–hole pairs follows the relation $E_{\text{X-ray photon}}/2E_{\text{bandgap}}$ in ionic crystals. However, most scintillator materials follow ideal behavior only in a limited energy range, typically at the lowest energies. While ideally the intensity of the emission relative to the X-ray energy plotted against the X-ray energy (i.e. I/E versus E) is a horizontal line, it mostly follows an ascending series since the scintillation luminescence intensity grows with energy. [125,128]

The scintillation process is important in a variety of fields, including nuclear physics, particle physics, and medical imaging. Scintillation detectors are commonly used in these fields to detect and measure ionizing radiation. For example, scintillation detectors are used in positron emission tomography (PET) scanners, which are used to image the distribution of radioactive tracers in the body for medical diagnosis and research. Some scintillator materials are e.g. CeF_2, $Bi_4Ge_3O_{12}$, CsI,

BaF_2, LaF_3, $CdWO_4$, $YTaO_4$, CsF, BaF_2, $KMgF_3$, $Gd_2O_3:Eu^{3+}$, $Gd_2O_2S:Pr^{3+}$, $Gd_2O_2S:Tb^{3+}$, $CaF_2:Eu^{2+}$, $Lu_2SiO_5:Ce^{3+}$, $LaF_3:Nd^{3+}$, $NaI:Tl^+$, $CsI:Tl^+$, $CsI:Na^+$, $CdS:Te^{2-}$, ZnS:Ag, CuI, and PbI_2. [108,113,114,127,129]

2.6.5 Detection methods

The detection of high-energy radiation is based on its interaction with matter, mainly by using the following methods.

1. Photographic film: the photon excites an electron in a silver halide crystal to a nearby crystal defect, which in turn attracts a nearby silver ion. The recombination event produces silver metal, which appears as an opaque spot in the film, contrary to the transparent silver halide. [130]
2. Optically stimulated luminescence (OSL): upon photon irradiation, an electron from the dopant material is excited to a crystal defect in the host lattice, e.g. $BaFBr:Eu^{2+}$ in which the europium ion is oxidized to Eu^{3+} and the electron is trapped inside a vacancy energy level residing in the bandgap of the material. The electron is liberated from the vacancy using laser stimulation, after which the electron emits a photon in the visible range. Other examples are e.g. α-Al_2O_3:C [131,132], $CaSO_4$:Mn [133], opal ($SiO_2 \cdot nH_2O$) [134], spodumene ($LiAlSi_2O_6$) [135], ZrO_2 + PTFE [136], $RbCdF_3:Mn^{2+}$ [137], AlN-Y_2O_3 [138], KBr:Eu [138], KCl:Eu [138], $LiAl(SiO_3)_2$ [138] and MgS:Ce,Sm [139].
3. Thermoluminescence: the method works similarly with OSL, but the electron is liberated from the trap with heat stimulation. Example materials are CaS:Ce and Dy_2O_3 nanophosphors, $Li_2B_4O_7$, $CaSO_4$, Mg_2SiO_4, LiF [140], NaCl [141] , $KMgF_3$ crystals [142], CaF_2 [143], diamonds [144], AlN [144] α-Al_2O_3:C, α-Al_2O_3:C,Mg, and $Gd_2O_3:Eu^{3+}$. [145–153]
4. Fluoroscopy: this method does not require a material with defects, as it is based on fluorescence. The high-energy photon excites an electron in the material's valence band, after which the electron recombines immediately with its hole, emitting a visible photon. This enables either intermittent (computed tomography, CT) or real-time surveillance of the functioning of tissues and organs. Even though the radiation exposure is rather low due to the method being only a supporting tool and not a diagnostic scan in itself, it still contains the risk of exposing the subject to large doses of ionizing radiation if used for prolonged times. In fluoroscopy, along with more rarely used gadolinium-based materials, mostly organic iodinated contrast agents such as diatrizoate, iothalamate, ioxaglate, iohexol,

ioversol, iopamidol, and iodixanol are used to make a radiodensity gradient inside the body. [154–159]

5. Semiconductor detectors: a high-energy photon impinges upon a semiconductor material and converts the electron excitation either directly or indirectly (through scintillation-induced visible light detection) to electrical signal. The advantage with these materials, e.g. lithium-drifted Si, Ge, GaAs or Si, is their fast speed and sensitivity. [160–163]
6. Gas ionization detectors: a high-energy photon creates an ion pair in a gas chamber with an external electric field. The electrons moving in different directions induce a dose rate-proportional current, which is detected by the instrument. These detectors are classified into three categories: ion chambers, proportional counters, and Geiger–Müller counters. [164]
7. Radiochromic films: a film where the high-energy photon alters the structure of the material so that there is visible color change which can be measured e.g. densitometrically or with reflectance spectroscopy. [165–167]

Some recently discovered radiation detection materials are based on metal-organic frameworks that are sensitive and show a clear response [168–173], but due to their organic nature they are less robust than crystalline inorganic materials.

2.6.6 Photochromic minerals and high-energy radiation

Since inorganic crystalline materials exhibit intrinsic defects where charge carrier trapping can occur, many experiments have been conducted since the invention of X-rays by Wilhelm Röntgen in the late 19th century. The plethora of reports about X-ray-colorable inorganic materials emerged soon after the invention:

1. Barium platinocyanide pastilles developed by Raymond Sabouraud, Henri Noiré, and Léonard Bordier were one of the first commercial materials for detecting radiation. Upon exposure they changed their color from green to dark yellow or orange. [129]
2. Doelter's coloration experiments with spodumene ($LiAl(SiO_3)_2$), topaz ($Al_2SiO_4(F,OH)_2$), and quartz (SiO_2). The conclusion to the color change was given as the change of oxidation and reduction states of metallic oxides. [174]
3. Stuhlman & Daniel's kunzite ($LiAl(SiO_3)_2$) experiments where the color change was a side discovery of phosphorescence research. [175]

4. After these, the level of interest grew further, and when a high-brilliance X-ray source was developed in 1947, Pough & Rogers published their broad experiments with gem stones spodumene ($LiAlSi_2O_6$), beryl ($Be_3Al_2Si_6O_{18}$), corundum (Al_2O_3), tourmaline (complex silicate), quartz (SiO_2), topaz ($Al_2SiO_4{\cdot}(F,OH)_2$), diamond (C), spinel ($MgAl_2O_4$), phenakite (Be_2SiO_4), apatite ($Ca_5(F,Cl)(PO_4)_3$), fluorite (CaF_2), opal ($SiO_2{\cdot}nH_2O$), scapolite (complex silicate), brazilianite ($Na_2Al_6P_4O_{14}{\cdot}4H_2O$), simpsonite ($Al_{10}Ta_6O_{20}$), dioptase ($H_2CuSiO_4$), hackmanite ($Na_8Al_6Si_6O_{24}(Cl,S)_2$), cancrinite ($(Na,Ca,\square)_8Al_6Si_6O_{24}(CO_3,SO_4)_2{\cdot}2H_2O$), lapis lazuli (complex Na aluminosilicate containing lazurite), zircon ($ZrSiO_4$), chrysoberyl ($BeAl_2O_4$), and oligoclase ($(Na,Ca)(Si,Al)_4O_8$). [176]
5. During the next decade, Claffy experimented with hiddenite ($LiAl(SiO_3)_2$) and spodumene ($LiAl(SiO_3)_2$), and Medved and Kirk carried out their groundbreaking work focusing on hackmanite and its underlying coloration mechanism. [8–10]

The phenomenon of high-energy radiation-induced coloration in gemstones has long been a subject of fascination and intrigue, yet it has not been given the level of scientific attention it deserves in terms of exploring its underlying mechanisms and details. Despite the efforts of some researchers listed above who have treated gemstones with high-energy radiation to gain insights into the mechanism, this field remains largely unexplored. There are still many unanswered questions regarding the fundamental mechanisms and processes that lead to the generation of color centers in gemstones under the influence of high-energy radiation. As such, there is a pressing need for more systematic and rigorous scientific investigations to unlock the secrets of this intriguing phenomenon and to deepen the understanding of the physical and chemical principles underlying the coloration of gemstones induced by high-energy radiation.

2.6.7 Commercial passive high-energy detection materials

Current commercial X-ray and gamma radiation detectors, i.e. radiochromic films, are mainly based on polydiacetylene and lithium-10,12-pentacosadiynoate (LiPCDA), which go under the trade name family GAFchromic™. The usable range of these materials is 0.01−2500 Gy [177–179], although the American Association of Physicists in Medicine's radiochromic film dosimetry task group suggests not to exceed 1 kGy with these films. [180] On the more higher dose scale, radiochromic films with hydrophobic-substituted tripentylmethane leucocyanides work with dose ranges up to 10^6 Gy. [181–186]

These materials work as passive dosimeters since there is a clear color change that does not need to be converted to an electrical signal, however, practically the dose is read densitometrically. [187] The disadvantage of these materials is that they are single-use only, they show darkening under ambient light and should be protected from temperatures over 60 °C to avoid non-desirable molecular transformations of the radiochromic material. [180] Thus, there is a need for research of reusable materials.

3 Materials and methods

3.1 Synthesis of hackmanite samples

3.1.1 X-ray coloration experiments

Five different hackmanite samples were tried in the coloration experiments, abbreviated as Na, Li, K, Br, and Rb. Their full meanings are given below:

1. Na = $Na_8Al_6Si_6O_{24}(Cl,S)_2$ i.e. standard or pristine hackmanite. This material was synthesized by weighing 0.700 g of zeolite A (Sigma Aldrich, dried at 500 °C for 1 h prior to weighing), 0.240 g of NaCl (J. T. Baker, >99.5%), and 0.0600 g of Na_2SO_4 (Merck, >99%). First, the NaCl crystals were crushed into powder form in an agate mortar, after which the Na_2SO_4 was added and ground together with the NaCl, and finally the zeolite was added and the mixture was ground together for a few minutes by hand. The mixture was then poured into an alumina crucible (Ceramic Oxide Fabricators model CB-0005) and heated in air atmosphere at 850 °C for 48 h, the ramp rate being 10 °C/min. After the furnace had cooled down to room temperature passively, the mixture was ground once again in the agate mortar and given the same temperature treatment in a flowing H_2/N_2 (12%/88%) atmosphere. Then, after cooling passively to room temperature, the finished product was ground once more.
2. Li = $LiNa_7Al_6Si_6O_{24}(Cl,S)_2$ i.e. Li-doped hackmanite. This was made with the same procedure as Na, but with the following reagents: 0.700 g of zeolite, 0.0850 g of LiCl (Acros, 99%), 0.1200 g NaCl, and 0.0600 g Na_2SO_4.
3. K = $(K,Na)_8Al_6Si_6O_{24}(Cl,S)_2$ i.e. K-doped hackmanite. This was made with the same procedure as the previous ones, but with the following reagents: 0.700 g of zeolite, 0.306 g of KCl (E. Merck, Suprapur), and 0.0600 g Na_2SO_4.
4. Br = $Na_8Al_6Si_6O_{24}(Br,S)_2$ i.e. Br-doped hackmanite. This was made with the same procedure as the previous ones, but with the following reagents:

0.700 g of zeolite, 0.427 g of NaBr (J. T. Baker, reagent grade), and 0.0600 g Na_2SO_4.

5. Rb = $(Na,Rb)_8Al_6Si_6O_{24}(Cl,S)_2$ i.e. Rb-doped hackmanite. This was made with the same procedure as the previous ones, but with the following reagents: 0.700 g of zeolite, 0.496 g of RbCl (Sigma, ≥99.0%), and 0.0600 g Na_2SO_4.

To make the handling, measurement, and transportation easy, the hackmanite powders were mixed with a binder and plasticizer to make flexible tapes. First, a mixture of 40 m-% of hackmanite, 30 m-% of 2-butanone, 15 m-% of ethanol and 2 m-% of Triton X-100 was mixed in a Philips Minimill PW4018/00 ball mill at speed 1 for 10 minutes, after which 7 m-% of polyvinyl butyral and 6 m-% of benzyl butyl phthalate were mixed with the mill operating at speed 5 for 2 minutes. Then, the ready mixture was cast onto a 0.1-mm thick Folex® Premium Universal Copy Film X-100 A4 (art no. 39100.100.44000) polyethylene film with an Erichsen Coatmaster 510 film applicator using 300 µm wet thickness. After drying in room temperature, the finished film consists of ~73% of hackmanite when the 2-butanone and ethanol have completely evaporated.

3.1.2 Gamma radiation coloration experiments

In gamma coloration experiments, another batch of Na, Li, K, Br, and Rb hackmanites were synthesized with the same procedure as in the X-ray coloration experiments, but the heating in air atmosphere was shortened to 2 h after it was noticed that the Na hackmanite does not need 48 h of first heating, but only 2 h suffices to produce the tenebrescence effect.

3.1.3 Photography

The hackmanite sample used for photography was synthesized with the same procedure as the Na sample in the gamma coloration experiments.

3.1.4 Upscaled batches

The hackmanite samples used for researching an upscaled synthesis process were as follows:

1. A 1-kg batch was made by pouring 700 g of zeolite A (Sigma Aldrich, dried at 500 °C for 1 h prior to weighing), 240 g of NaCl (J. T. Baker, >99.5%, crushed into a powder prior to weighing), and 60 g of Na_2SO_4 (Merck, >99%) into a 2-litre ziplock bag and shaking the bag for

5 minutes. Then, the mixture was poured into a custom-made clay (Kerasil product number 525205, 267 vaalea/keltainen AR-267 koulusavi 0–0,2 mm samotilla) crucible coated with Cotronics Resbond® 989 aluminium oxide paste. The paste was used to prevent the leaching of clay minerals from the container to the sample at high temperatures. The temperature treatment was 2 h in a Thermolyne F30400 furnace at 850 °C (ramp rate 18 °C/min), then after passive cooling to room temperature, the sample was crushed with a mallet and poured into the container again. It was then reduced at the bottom of a steel-lined heavy-duty retort furnace in Hilamet Oy, Ylihärmä, Finland for 2 h at 850 °C, the ramp rate being 10 °C/min. Prior to heating, the furnace was flushed with 2.5 m^3 of Formier® 10 gas with a flow rate of 83 l/min, and during the synthesis the gas flow was lowered to 1.0 l/min.

2. A 100-g batch was made similarly as the 1 kg batch, but the amount of reagents were $1/10^{th}$ of the 1-kg batch. In addition to this, a lid was made for the clay container to see if it could protect the batch from impurities from the oven. The heating steps and equipment were the same as in 1.

3.2 Characterization methods

3.2.1 Reflectance and XEOL spectroscopy

One of the most important tools to compare and quantify the tenebrescence feature in hackmanites was measuring the coloration's reflectance spectrum. At Karlsruhe's synchrotron facility and Swedish Defence Research Agency, the spectra were collected using Avantes AvaSpec ULS2048CL-EVO CCD spectrometer coupled with an Avantes FC-IR600-1-ME-HTX optical fiber, and Ocean Optics LS-1 Cal lamp providing a continuous spectrum for the measurements. For UV- and XRF-induced coloration experiments, the spectra were collected using Avantes AvaSpec HS-TEC CCD spectrometer coupled to a FC-IR600-1-ME-HTX optical fiber. The light source was either a 60-W incandescent lamp or Ocean Optics LS-1 Cal calibration lamp. Konica Minolta CM-2300d was used for the gamma coloration experiments at the Finnish Radiation & Nuclear Safety Authority's premises. In further gamma radiation-induced coloration experiments, the reflectance measurements were carried out with an Avantes AvaSpec ULS2048CL-EVO CCD spectrometer coupled to an Avantes FC-IR600-1-ME-HTX optical fiber. The light source was either a 60-W incandescent light bulb (color fading measurements) or an Ocean Optics LS-1 Cal calibration lamp (other measurements) directed towards the sample 20 cm away. In all figures showing reflectance spectra, individual spectra

show the difference between a non-irradiated and irradiated sample. The irradiation wavelength for inducing the color change was 254 nm (lamp UVLS-24 254 nm 4 W).

When measuring the bleaching spectra, the sample was irradiated with a 150 W xenon arc lamp. A LOT MSH300 monochromator was used to select the wavelengths, and the irradiation time at each wavelength was 10 min for the Li sample, 1 min for Br and Na, and 30 s for Rb. The different times were due to material-specific differences in the optical energy needed to induce large enough a change in the reflectance spectrum.

For the XEOL measurements, an Avantes AvaSpec ULS2048CL-EVO CCD spectrometer coupled with an Avantes FC-IR600-1-ME-HTX optical fiber was used in scope mode.

3.2.2 VUV measurements

Vacuum ultraviolet spectroscopy (VUV) measurements were performed at the Toroidal Grating Monochromator [188] beamline in the Brazilian Synchrotron Light Laboratory. The system uses quartz filters to avoid higher harmonic excitation. The emission spectra were measured with an optical fiber coupled to an Ocean Optics QE65000 spectrometer.

3.2.3 Cathodochromism

Cathodochromism, i.e. electron beam-induced coloring, was induced with a Nuclide Corporation ELM2EX luminoscope coupled to a Nuclide Corporation ELM2B vacuum chamber. The color intensity was determined outside the vacuum chamber from reflectance spectra measured using Avantes AvaSpec HS-TEC CCD spectrometer coupled to a FC-IR600-1-ME-HTX optical fiber, with Ocean Optics LS-1 Cal lamp acting as the light source.

3.2.4 Thermotenebrescence

Thermotenebrescence [19,21] curves were constructed by measuring the reflectance spectra of a fully colored sample as a function of temperature using Avantes AvaSpec HS-TEC CCD spectrometer coupled to a FC-IR600-1-ME-HTX optical fiber, with Ocean Optics LS-1 Cal lamp as the light source. MikroLab Thermoluminescent Materials Laboratory Reader RA'04 programmed at a heating rate of 3 °C/s was used for the heating. The curves were corrected for spontaneous fading in the lighting conditions used.

3.2.5 X-ray analysis methods

3.2.5.1 X-ray diffraction (XRD)

In this work, PXRD was used to obtain information about the purity of the products, and also to see if there were any changes in the crystal structure after exposure to high-energy photons. The X-ray diffractograms were obtained with PANalytical Aeris operating at 40.0 kV and 7.5 mA using Cu $K_{\alpha 1,2}$ radiation, and Huber G670 position sensitive detector and $CuK_{\alpha 1}$ radiation from a Rigaku Geigerflex X-ray source using 40 kV and 30 mA. The detector in Aeris was PIXcel1D-Medipix3, and the optical setting was a 13 mm mask, 1/2° divergence slit, 0.04 rad soller slits, 9 mm anti-scatter slit, nickel beta-filter, high beam knife, 1 rounds per second spinner speed. The data acquisition was obtained using a scan rate of 0.201 °/s with a step size of 0.0217°. Quantitative phase analyses and unit cell parameter refinements were conducted with Rietveld refinements using PANalytical HighScore Plus 4.9.0.27512 with the following settings:

1. Background was determined with a bending factor of 2 and granularity 20 using smoothed input data.
2. Peaks were searched with a minimum significance of 2.00, minimum tip width 0.01, maximum tip width 1.00, peak base width 2.00, method Minimum 2nd derivative.
3. The search & match pattern list was used from a subset that contained PDF-4+ 2021 4.21.0.2 (database version 4.2103) database occurrences 04-016-5475 (NaCl) and 04-017-7136 ($Na_8Al_6Si_6O_{24}Cl_{1.8}S_{0.1}$). The peaks were fitted with a default profile fit and finally refined with default Rietveld using available background as the method in global variables.

The Micro-XRD patterns were measured with a PANalytical Empyrean diffractometer with $CuK_{\alpha 1,2}$ radiation. The setup yielded a 0.4 mm × 0.5 mm irradiation beam on the sample surface. Gamma-colored films' X-ray diffraction measurements were carried out using PANalytical Empyrean using $CuK_{\alpha 1,2}$.

3.2.5.2 X-ray fluorescence (XRF)

XRF (PANalytical Epsilon 1 with internal Omnian calibration) was used to gain knowledge about the upscaled batch's washing procedure; mainly the levels of NaCl and hackmanite in the washing water.

The micro-XRF line sweep scan was conducted using a Bruker Tornado M4 micro-XRF spectrometer.

3.2.5.3 XANES and XAS

The XANES spectra were collected at Karlsruhe Institute of Technology's Synchrotron Laboratory for Environmental Studies (Synchrotron Umwelt-Labor) SUL-X beamline [189] with an adjustable X-ray energy of 2.3–20 keV. The SUL-X beamline employs a wiggler radiation source and a Si(111) fixed exit double crystal monochromator for tuning the X-ray energy. In Li sample's case, the X-ray beam was focused with a Kirkpatrick–Baez mirror system to *c.a.* 50 µm (vertical) and 150 µm (horizontal), and when irradiating the Na, Rb, and Br samples the beam was collimated to *c.a.* 0.5 mm (vertical) 1.3 mm (horizontal) at the sample distances. When tracking the pre-edge peak maximum, a focused beam of about 50 µm × 50 µm was used. The energy level was calibrated to 2481.4 eV at the highest point of the sulfate peak on the S K-edge XANES spectrum of a Scotch tape. Using a seven-element silicon drift diode detector equipped with 12.5µm DuraBeryllium windows (model SiriusSD-M7x65133-BE-INC-V, Rayspec) at xMAP and Falcon electronics (XIA), the S K_α fluorescence emission intensities were measured. The S K_α fluorescence emission was utilized to measure the intensities of the pre-edge maximum during irradiation, the whole pre-edge peak, and the S K XANES spectra. The energy step width across the pre-edge and absorption edge was set at 0.2 eV. All measurements were performed under vacuum.

3.2.5.4 X-ray photoelectron spectroscopy (XPS)

XPS measurements were carried out using Perkin Elmer PHI 5400 ESCA and Thermo Scientific NEXSA XPS systems using Mg and monochromated Al X-ray sources respectively.

3.2.6 Electron paramagnetic resonance (EPR)

X-band (9.43 GHz) EPR spectra were measured with a Magnettech GmbH MS-200 Miniscope high resolution spectrometer equipped with a XL Microwave frequency counter (Model 3200) at 77 K by submerging the sealed samples in liquid nitrogen. The spectra were calibrated against 2,2-diphenyl-1-picrylhydrazyl (DPPH, $g = 2.0036$).

3.2.7 Raman spectroscopy

The Raman spectra were recorded using an inVia Qontor confocal Raman microscope (Renishaw, Gloucestershire, UK) using 785 nm continuous wave laser excitation.

3.3 Irradiation methods

In the X-ray induced coloration experiments, the irradiation was conducted at Karlsruhe Institute of Technology's Synchrotron Laboratory for Environmental Studies (Synchrotron Umwelt-Labor) SUL-X beamline. In X-ray imaging experiments, PANalytical Epsilon 1 XRF instrument that probes the sample with Ag K_α radiation (*ca*. 22 keV) was used.

In nuclear radiation coloration experiments, the quantitative dose series samples were subjected to a collimated ^{60}Co gamma ray beam at Finnish Radiation and Nuclear Safety Authority's premises in Helsinki, Finland. The air kerma values (0.2, 1.0, 3.0, 5.0, and 7.0 kGy) and thus gamma radiation doses at the samples' positions were controlled by placing the samples at different distances from the source. The gamma radiation qualities were established according to ISO standard 4037-1:2019. Qualitative nuclear and particle radiation coloration experiments were conducted with ^{109}Cd, ^{133}Ba, ^{137}Cs, ^{210}Pb, ^{241}Am, ^{238}U, and ^{18}F at the Swedish Defence Research Agency (Totalförsvarets forskningsinstitut, FOI), Sweden. Table 1 lists the used nuclides and their predominating emission energies.

Table 1. The radiation sources used in the nuclide coloration experiments. Reproduced from **II** with permission from the Royal Society of Chemistry.

NUCLIDE	RADIATION	ACTIVITY (Bq)	ENERGY (keV)
Co-60	γ γ β	$215 \cdot 10^3$	1173 1333 318
Co-60	γ γ β	$4.2 \cdot 10^9$	1173 1333 318
Cd-109	γ X β	$87 \cdot 10^3$	88 22 126
Ba-133	γ X β	n.a.	356 and 80 31 80
Cs-137	γ β	$80 \cdot 10^6$	662 514
Pb-210	γ β α	$20 \cdot 10^3$	46 17 3720
Am-241	γ X α	$2 \cdot 10^3$	60 12–22 5486
U-238*	α	n.a.	4198
F-18	Positrons γ**	$2.4 \cdot 10^6$	634 511

* depleted uranium
** annihilation photon

Exposure to beta radiation (positrons) was performed by pipetting ^{18}F-water (3 µl in triplicate) with a measured activity concentration (Veenstra VDC-405 dose calibrator) directly on the film at the Radiochemistry Turku PET Centre, University of Turku, Finland

3.4 Computational details

3.4.1 Geometry optimization in X-ray coloration

Using the ab initio CRYSTAL17 code [190], geometry optimizations were conducted with periodic boundary conditions (PBC) in the framework of density functional theory (DFT). The global hybrid functional PBE0 [191] was selected along with a localized (Gaussian) basis, which is known to give accurate geometrical parameters for sodalites. [23] All-electron double-ζ basis sets with polarization functions were used for all hackmanite elements except sulfur, which received treatment with all-electron triple-ζ basis sets with polarization functions. The reciprocal space was sampled according to a sublattice with a 12×12×12 k-points mesh for the geometry optimization of the bulk system, and a single k-point (the Γ point) was used for geometry optimization of the 2×2×2 supercells containing the default sulfur species. The convergence criterion for the SCF cycle fixed to 10^{-7} Ha per unit cell.

3.4.2 Geometry optimizations in gamma coloration

The calculations for optimizing geometry were carried out using PBC in the DFT framework. To perform these calculations, the ab-initio CRYSTAL17 code [190] was used in conjunction with localized (Gaussian) basis sets and the global hybrid functional PBE0 [191].

All-electron double-ζ basis sets with polarization functions were employed for Si ([4s3p1d]/(20s12p1d)), Al ([4s3p1d]/(17s9p1d)), O ([3s2p1d]/(10s4p1d)), and Cl ([4s3p1d]/(16s10p1d)), while all-electron triple-ζ basis sets with polarization functions were employed for Na ([4s3p1d]/(15s7p1d)). Additionally, to accurately describe the trapped electron present in all structures, a basis set optimized with the 111G(d) structure was utilized. The optimized coefficients can be found in the Supporting Information of **I**. For the geometry optimization of the bulk system, the reciprocal space was sampled using a sublattice with a 12×12×12 k-points mesh. For the geometry optimization of the 2×2×2 supercell, only a single k-point (the Γ point) was utilized. The convergence criterion for the SCF cycle was set to a fixed 10^{-7} Ha per unit cell. In the case of considering the formation of a sodium vacancy as the deformed color center ($Na_4V_{Cl} \rightarrow Na_3V_{Cl}$), the resulting loss of electroneutrality was

offset by substituting one Al^{3+} with one Si^{4+} in the β-cage situated around the vacancy.

TD-DFT calculations were carried out using the B3LYP functional and the Gaussian 16 code [192]. To perform these calculations, clusters were extracted from the geometries optimized in PBC and embedded in a sphere of pseudopotentials, along with an array of point charges [24]. These point charges were used to simulate the Madelung potential of the crystal and were generated through the Ewald package [193], utilizing a 5×5×5 supercell. The fitting procedure led to an RMS error of less than 1 μV on the Ewald potential.

3.4.3 XANES simulations

To perform XANES calculations, a TD-DFT formalism was utilized, which was implemented in the ORCA program [194–196]. These calculations were performed at the B3LYP/def2-SVP level of theory. Relativistic corrections were taken into account utilizing the ZORA method, and to accelerate the calculations, the RIJCOSX approach was employed. The energy convergence criterion for the SCF cycles was set to a fixed 10^{-8} Ha per unit cell. For these calculations, the excitation window was limited to the 1s core orbital of the relevant sulfur species, along with virtual orbitals that possessed energies higher than the first virtual orbital of the sulfur species. A total of 240 transitions were computed, and these calculations were carried out on a cluster that was extracted from the optimized geometry. The cluster employed in this study comprises the sulfur impurity, the Na_4 tetrahedron, and the surrounding β-cage. To model the cage, pseudopotentials were employed to describe the cations, and a cloud of point charges was utilized. The point charges were generated using the Ewald package [193] to simulate the Madelung potential of the crystal. To generate the point charges, a 5×5×5 supercell was utilized, and the fitting procedure resulted in an RMS error of less than 1 μV on the Ewald potential. This methodology is consistent with prior work reported in [24].

4 Results and discussion

4.1 X-ray-induced color centers

Reversible color centers can be studied with a) the energy required to induce coloration b) the absorption spectrum c) the optical energy required to bleach the coloration d) the thermal energy to bleach the coloration and e) the spontaneous fading of the coloration at a steady temperature. These properties were studied with X-ray- and UV-colored Li, Na, Rb, and Br samples. The reflectance spectra in Figure 9 show that the X-ray- and UV-induced color centers show similar characteristics in terms of absorption bands, which the optical fading spectra in Figure 10 support. There are some discrepancies that, however, are within the boundaries of experimental inaccuracy and effects that are likely caused by inhomogeneities from the tape casting process and the differences in coloration depth.

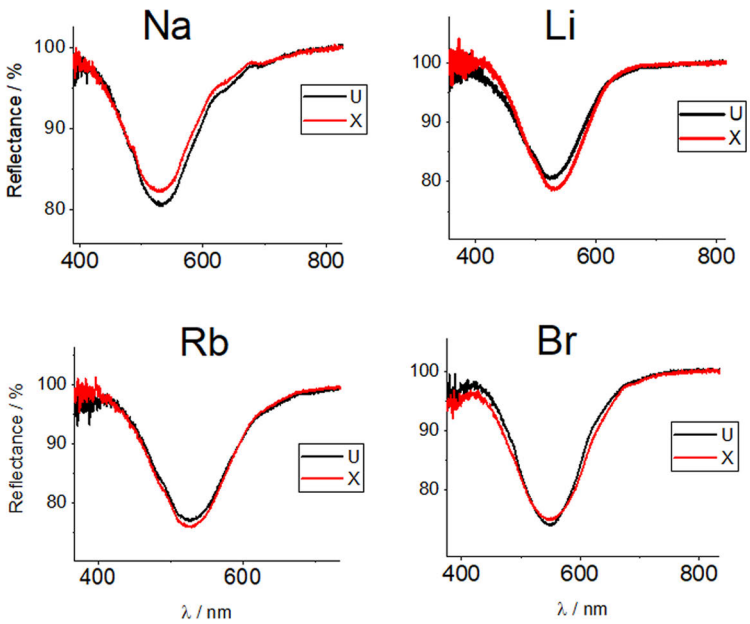

Figure 9. Reflectance spectra of all studied samples, showing similar absorption characteristic for 254 nm UV- (U) and ~22 keV X-ray-induced (X) coloration. Figure adapted from **I** with permission from John Wiley & Sons, Inc.

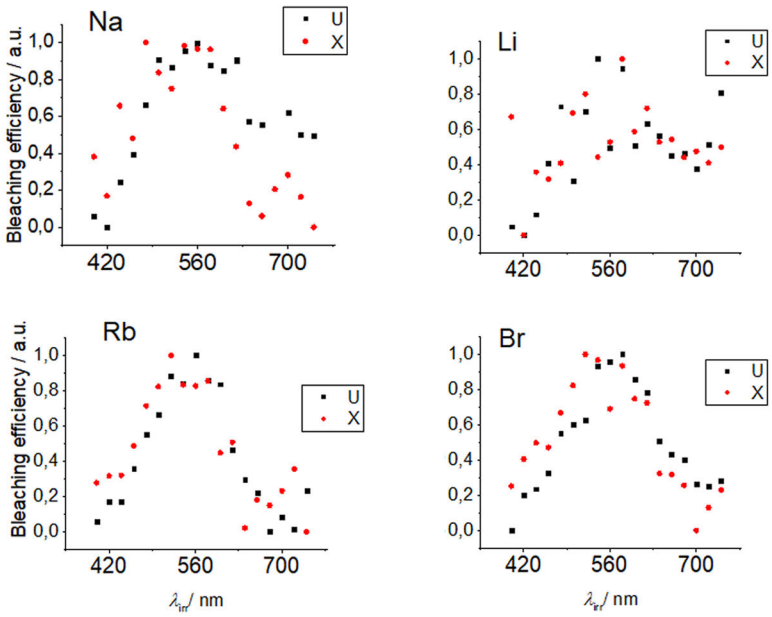

Figure 10. Optical bleaching spectra of 254 nm UV- (U) and ~22 keV X-ray-induced (X) coloration. Figure adapted from **I** with permission from John Wiley & Sons, Inc.

Figure 11's thermotenebrescence (thermal activation energy of the coloration's bleaching [19,21]) curves, i.e. thermal liberation of the trapped color center electrons, have some variation but are very close when the activation energies are calculated from the curves (Table 2). The different linear regions in the thermal fading curves when the natural logarithm of the coloration is plotted as a function of inverse temperature (see Supporting Information of **I**) give very close results that have normal variance of experimental experiments. This suggests that the formed color centers are the same as after UV coloration.

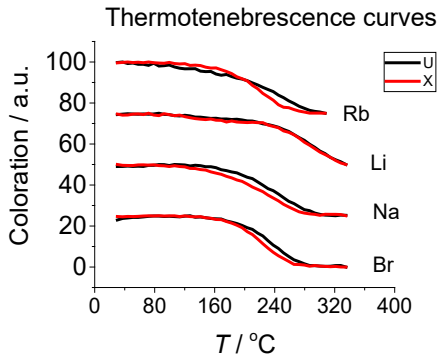

Figure 11. Thermal bleaching spectra of 254 nm UV- (U) and ~22 keV X-ray-induced (X) coloration, corrected for spontaneous fading. Figure adapted from **I** with permission from John Wiley & Sons, Inc.

Table 2. The thermal activation energies of Li, Na, Rb, and Br samples calculated from the data shown in Supporting Information of **I**. Numbers 1 and 2 signify different linear regions in the thermal fading curves when the natural logarithm of the coloration is plotted as a function of inverse temperature. Table adapted from **I** with permission from John Wiley & Sons, Inc.

	ACTIVATION ENERGY / eV			
SAMPLE	**UV 1**	**X-RAY 1**	**UV 2**	**X-RAY 2**
Li	0.23	0.21	0.41	0.42
Na			0.44	0.36
Rb	0.12	0.09	0.26	0.28
Br			0.61	0.56

In UV-induced coloration, the color saturates fast with a simple handheld 254 nm lamp. The saturation is reached after a UVC dose of 200 mJ/cm^2, which translates to 1 minute of irradiation at a 20-mm distance from the lamp, as is shown in Figure 12. The dose calculations are based on irradiance values measured with Opsytec Dr. Gröbel Radiometer RM 12 equipped with RM12 sensor calibrated for UVC.

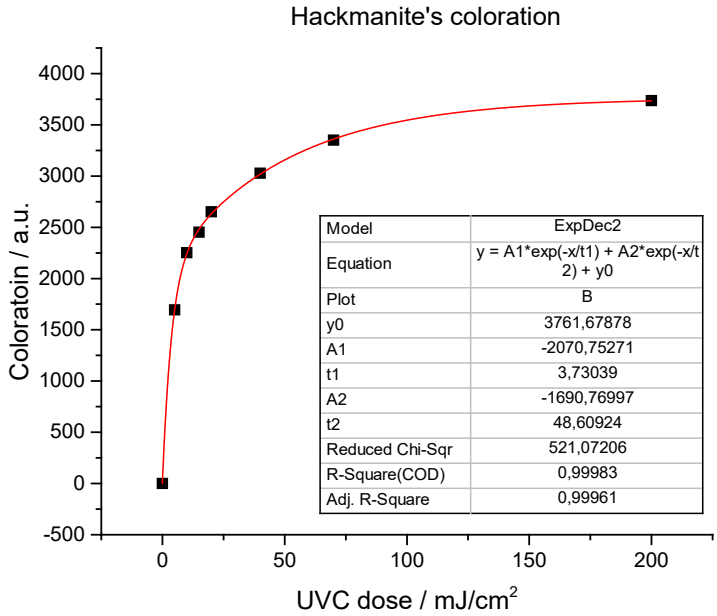

Figure 12. Hackmanite's coloration rise curve as a function of UVC dose.

However, the results from X-ray-induced coloration indicate that even a high-brilliance synchrotron X-ray beam is not enough to saturate the coloration after 1 hour of irradiation, as depicted in Figure 13a, which suggests that the coloration has a different mechanism than in UV-induced coloration. The coloration rise curves seen in Figure 13b are plotted against absorbed X-ray photons (incident photons divided by the mass attenuation coefficient, μ_M), which shows that the coloration rise rate is dependent on the energy of the X-ray beam: the lower the energy, the faster the coloration rate. This decreased coloration efficiency is proposed to be due to a stronger bleaching effect of the sample in the intense X-ray beam due to heat generation, as reported by Warren *et al*. [197], Kastengren [198], and Wallander and Wallentin [199] for various materials in different X-ray irradiation setups.

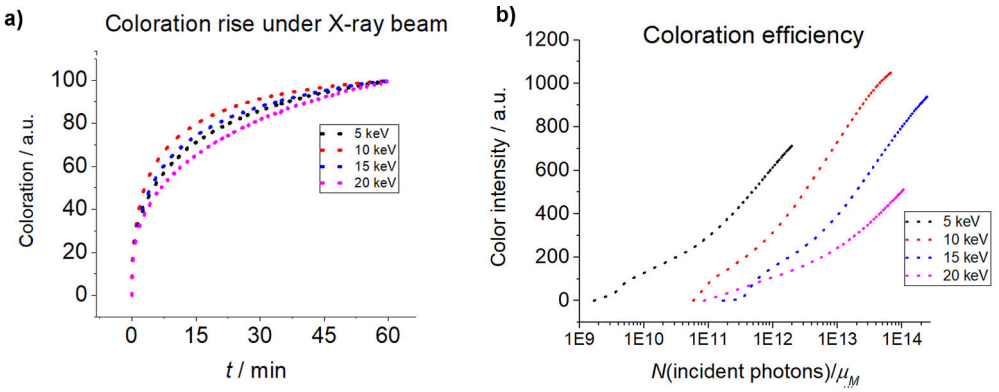

Figure 13. a) The coloration rise curves of Li hackmanite sample under different X-ray energy beams. **b)** Coloration rise curves as a function of absorbed X-ray photons (incident photons divided by the energy-dependent mass attenuation coefficient of Li hackmanite). Figures adapted from **I** with permission from John Wiley & Sons, Inc.

Figure 14a shows the same general behavior: the higher the X-ray energy, the lower the coloration. In scintillation, the dependence is reversed; if the flux is being kept at the same level, a higher energy translates to a higher signal output. The energy–intensity relationship in hackmanite was confirmed by irradiating a sample with electrons with different energies and measuring the coloration, which can be seen in Figure 14b. Since this cathodochromism behaves in a way that scintillation does, then there are other parameters that affect X-ray-induced coloration.

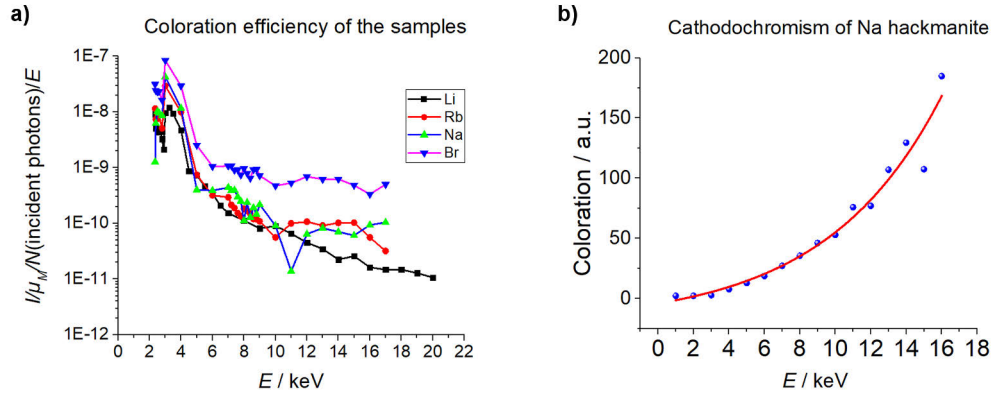

Figure 14. a) X-ray-induced coloration spectrum of Li, Na, Rb, and Br hackmanites. **b)** Coloration as a function of electron bombardment energy, i.e. cathodochromism. Figures adapted from **I** with permission from John Wiley & Sons, Inc.

One phenomenon that affects the coloration is radiation damage, which is a known effect that has also been reported for barium and strontium aluminates, which are

certain persistent luminescence materials. [200,201] This was observed in the measured samples (Figure 15a). An irradiated spot that had received a dose of 467 kGy of 6.5 keV X-rays showed to be solarized to a point where it did not change its color anymore under 254 nm UV irradiation (Figure 15b). Probing this spot with a micro-XRF sweep scanning (Figure 15c) showed no changes in the elemental composition of the hackmanite film, but micro-XRD (Figure 15d) surprisingly revealed an increased NaCl's (220) reflection, suggesting preferred orientation of NaCl that has crystallized with the (220) plane parallel to the surface, which means that the NaCl has left the sodalite structure and, as a result, created Na and Cl vacancies. An identical behavior is reported by Oliva-Ramirez *et al*. [202] in vapor-deposited NaCl.

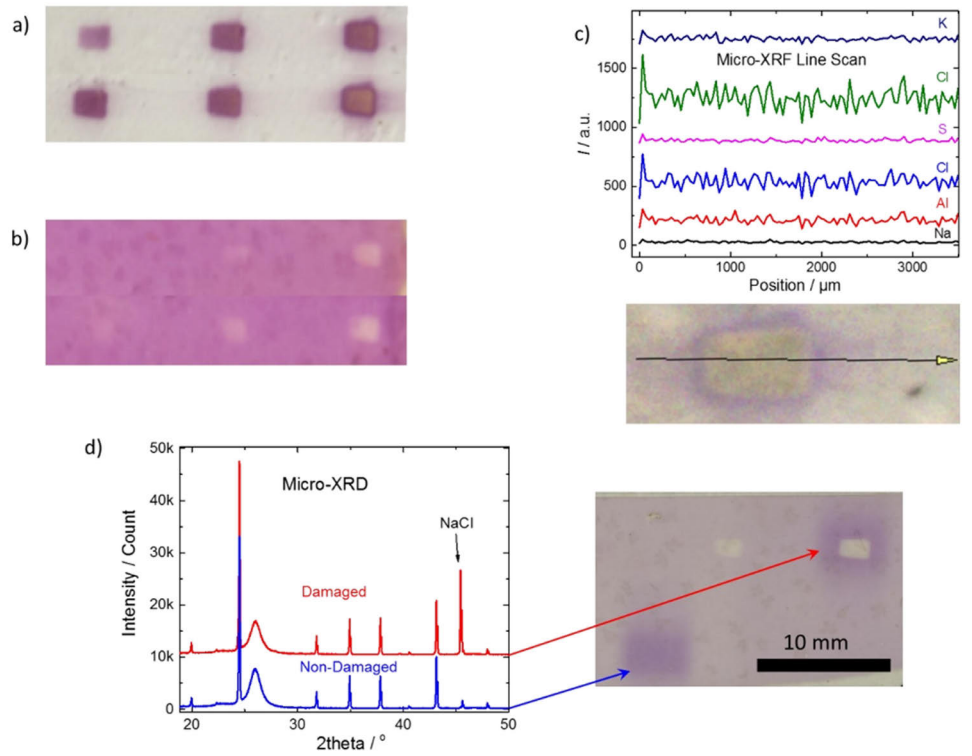

Figure 15. a) Heavily irradiated spots of Na hackmanite sample in the synchrotron X-ray beam. **b)** The same sample film colored with 254 nm UV. **c)** Micro-XRF sweep scan over a spot showing coloration fatigue. **d)** Micro-XRD measurement of a spot showing coloration fatigue. Image from **I**, licensed under CC BY 4.0 (https://creativecommons.org/licenses/by/4.0/).

During X-ray irradiation, a XEOL signal was observed in the UV range, peaking at c.a. 400 nm (Figure 16a). By looking at Figure 16d's vacuum-ultraviolet–ultraviolet emission measurements, it can be seen that the excitation energy nearing hackmanite's bandgap (7.7 eV [18]) shifts the emission from the Ti^{3+}–V_O pair in a hypsochromic fashion to the range which should be able to color hackmanite. To

study whether this scintillation-related emission could induce tenebrescence, this was later simulated in laboratory by using the same intensities of UV irradiation and seeing whether there is any tenebrescence from this emission (Figure 16e). After 30 minutes of irradiation there was no visible tenebrescence signal in the reflectance spectrum, therefore it was concluded that XEOL is not responsible for the coloration. Figure 16b and c show that hackmanite's XEOL behaves in scintillation's manner (the higher the energy, the higher the XEOL signal), but decreases as a function of time. This is another result that suggests that there is radiation-induced damage in the structure which affects the coloration process.

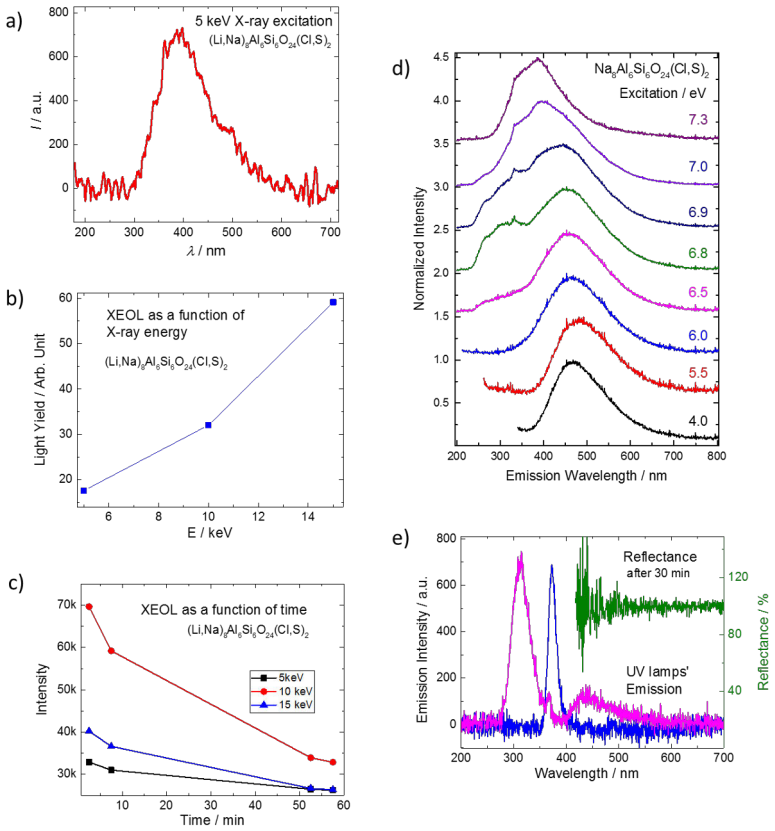

Figure 16. a) XEOL under 5 keV irradiation in the Li sample, peaking at c.a. 400 nm. **b)** XEOL as a function of X-ray energy, showing increasing XEOL intensity. **c)** XEOL as a function of time under a steady X-ray beam, showing intensity decrease. **d)** VUV-induced emission spectra. **e)** Spectra of UV lamps that were used in XEOL coloration simulations and hackmanite's reflectance spectrum after 30 minutes of this irradiation. Image from I, licensed under CC BY 4.0 (https://creativecommons.org/licenses/by/4.0/).

The Li, Na, Rb, and Br samples were probed with XANES measurements over sulfur's K edge region. In Figure 17a's XANES spectra, the edge and pre-edge

peaks' intensities are changing as a function of measurements (i.e. X-ray exposure), which is shown more clearly in Figure 17b and c: the intensity of the pre-edge peak increases, while the edge peak decreases. Since the increase of the pre-edge peak has a multicomponent rise function (Figure 18) similar to the deepening of tenebrescence (Figure 12), the pre-edge peak can be attributed to the rise of the coloration.

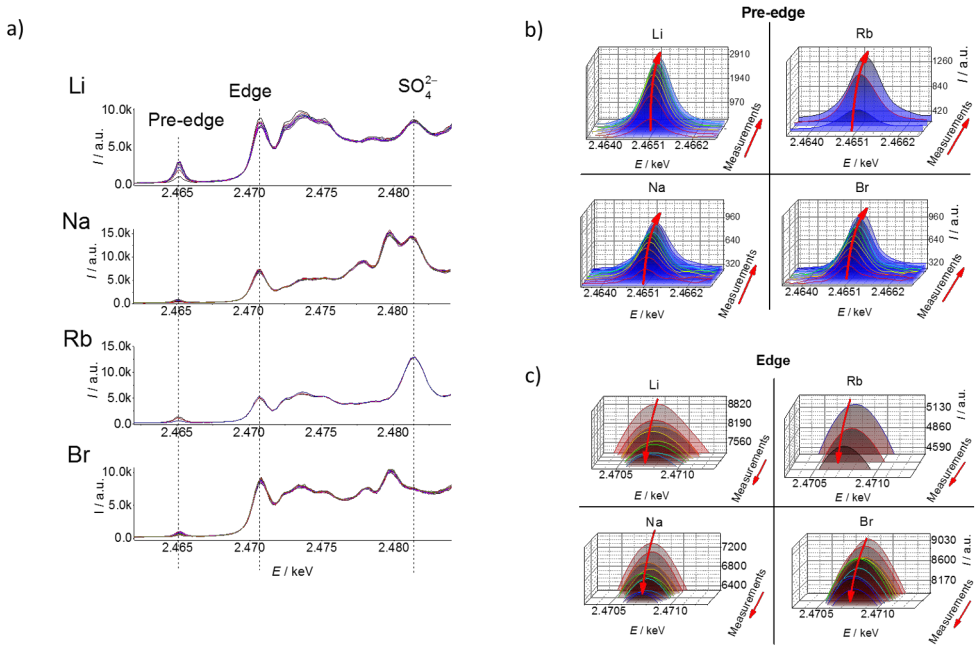

Figure 17. a) XANES spectra of Li, Na, Rb, and Br samples. **b)** The evolution of the pre-edge peak at ~2.465 keV as a function of measurements. **c)** The evolution of the edge peak at ~2.470 keV as a function of measurements. Image from **I**, licensed under CC BY 4.0 (https://creativecommons.org/licenses/by/4.0/).

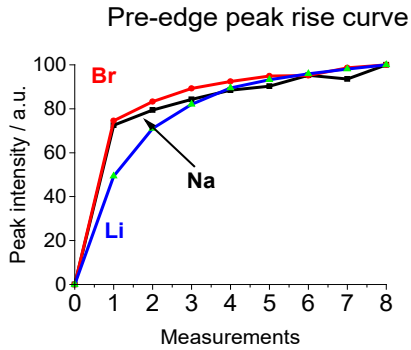

Figure 18. The pre-edge peak rise as a function of measurements. The Rb sample has been excluded since there were only three data points. Figure adapted from **I** with permission from John Wiley & Sons, Inc.

To study the correlation deeper, quantum chemistry calculations were conducted by substituting a chloride ion with S_2^- and S_2^{2-} ions inside sodalite's β-cage and a Na_4 tetrahedron, and calculating their transition properties under X-ray irradiation. The bandgap (Figure 19) of hackmanite contains the energy levels of an S_2^{2-} and V_{Cl} electron trap, which are the basis of the coloring process. The σ* is the empty orbital in S_2^{2-}, whereas π and π* are occupied.

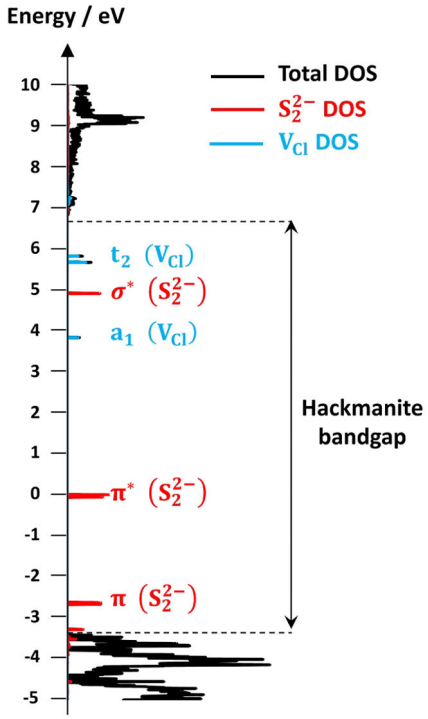

Figure 19. The density of states of an S_2^{2-} and V_{Cl} in hackmanite's bandgap. Image from **I**, licensed under CC BY 4.0 (https://creativecommons.org/licenses/by/4.0/).

According to the calculation results, the lower energy pre-edge signal is due to a 1s→π* transition of S_2^-, indicating that there has already been this sulfur species readily available for the transition to occur prior to the XANES measurement. The coloration of hackmanite by energies below the K edge of sulfur (2.4720 keV [119]) was confirmed from a coloration matrix where the X-ray energy started from 2.35 keV (Figure 20). This suggests that the excitation of sulfur's core shell electrons does not directly play a role in inducing the coloration.

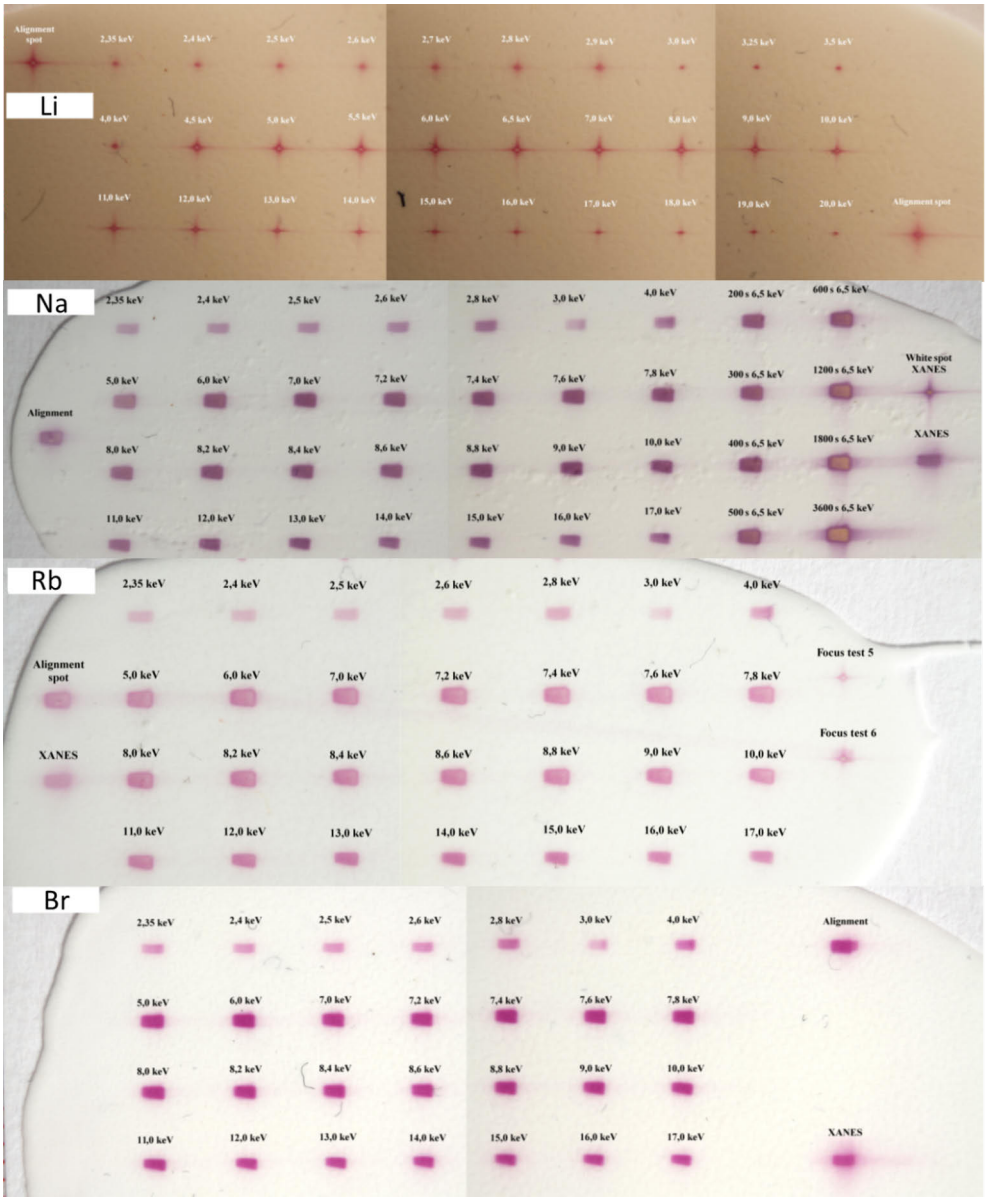

Figure 20. An X-ray coloration matrix with steady-state X-ray beams with different energies, starting from 2.35 keV and ending at 17.0 keV (20.0 keV for the Li sample). Image from **I**, licensed under CC BY 4.0 (https://creativecommons.org/licenses/by/4.0/).

Although the computational spectra in Figure 21a are not aligned perfectly with the experimental (Figure 21b), the qualitative features of pre-edge and edge bands explain the electronic transitions. Contrary to the differences of 1s→σ* transitions of S_2^{2-} and S_2^{-} seen in the computational spectra, the experimental energy difference

has been established to be ~1 eV for S^{2-} and S^0 [203]. This means that for the species seen in the spectra, i.e. S_2^- and S_2^{2-} (which correspond to $S_{0.5}^-$ and S^-, respectively), the K edge energy differences can be deduced to be ~0.25 eV. Thus, this energy difference cannot be seen in the experimental spectrum, i.e. the signals overlap in a way that the edge signal is a sum of 1s→σ* transitions of S_2^{2-} and S_2^-. The transitions, however, give different intensities, and by calculating their linear combinations the peaks' evolution directions can be estimated. The calculation results of the contributions from different mixtures of S_2^{2-} and S_2^- reveal that the pre-edge peak rises (Figure 21e) as there are more S_2^- ions, which is a result of a loss of one valence electron that subsequently leads to the coloration of the material. The edge peak, however, decreases as a function of relative S_2^- content (Figure 21e). In Figure 21f there is an estimate of the relative amount of the different disulfide species during the first XANES scan (blue) and after the sixth scan (blue), confirming that the same oxidation occurs in the crystal lattice as in UV-induced tenebrescence. These results are in total agreement with experimental measurements, and it is thus evident that the S_2^{2-} ions transform to S_2^- ions upon X-ray irradiation.

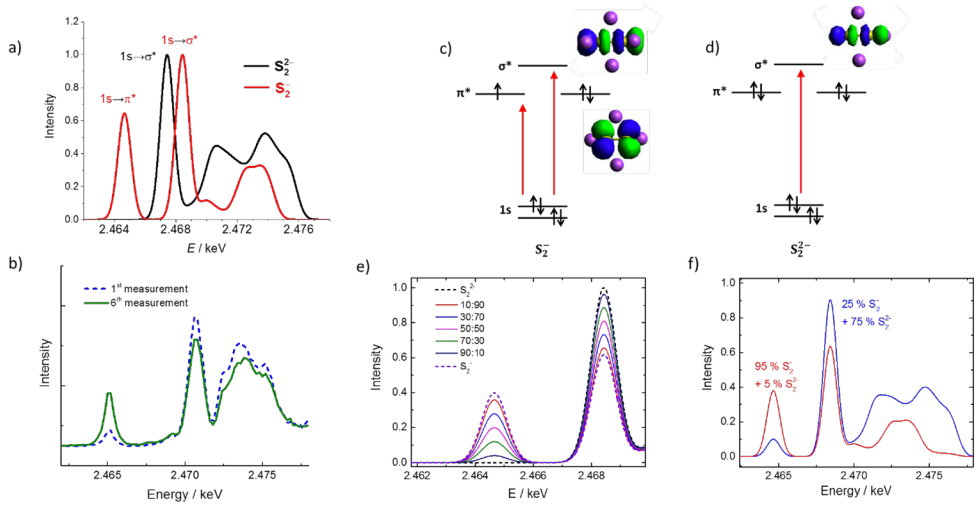

Figure 21. a) The computational XANES spectra of S_2^{2-} (black) and S_2^- (red). **b)** Actual measured XANES spectra of the Li sample. **c)** Possible electronic transitions of S_2^-. **d)** Possible electronic transition of S_2^{2-}. **e)** Computed XANES spectra of different mixtures of S_2^{2-} and S_2^- when there is a complete overlap of the 1s→σ* transition. **f)** Computed XANES spectra estimating the S_2^{2-}: S_2^- ratio of the Li sample shown in b). Image from **I**, licensed under CC BY 4.0 (https://creativecommons.org/licenses/by/4.0/).

4.2 Qualitative coloration tests with alpha, beta, and gamma radiation

Hackmanite films were subjected to radiation qualities listed in Table 1. Although the gamma sources were relatively weak, they all induced tenebrescence in the samples (Figure 22a). The coloration with an ^{241}Am source was tested with both gamma and alpha emissions by putting an Al filter in front of one sample and having no filter in front of the other (Figure 22b). Both radiation types induced coloration, which means that alpha radiation colors hackmanite as well. This was also confirmed with depleted uranium (Figure 22c).

Coloration with beta radiation was tested with ^{18}F (Figure 22d), yet there is a possibility that the coloration is due to the photons (gamma) that are produced after the annihilation of the positron after colliding with an electron. During these qualitative tests, it was noticed that these high-energy radiation types not only create the normally observed symmetric, broad 530 nm absorption band, but also two additional bands at ca. 480 and 600 nm, which are especially visible in Figure 22b.

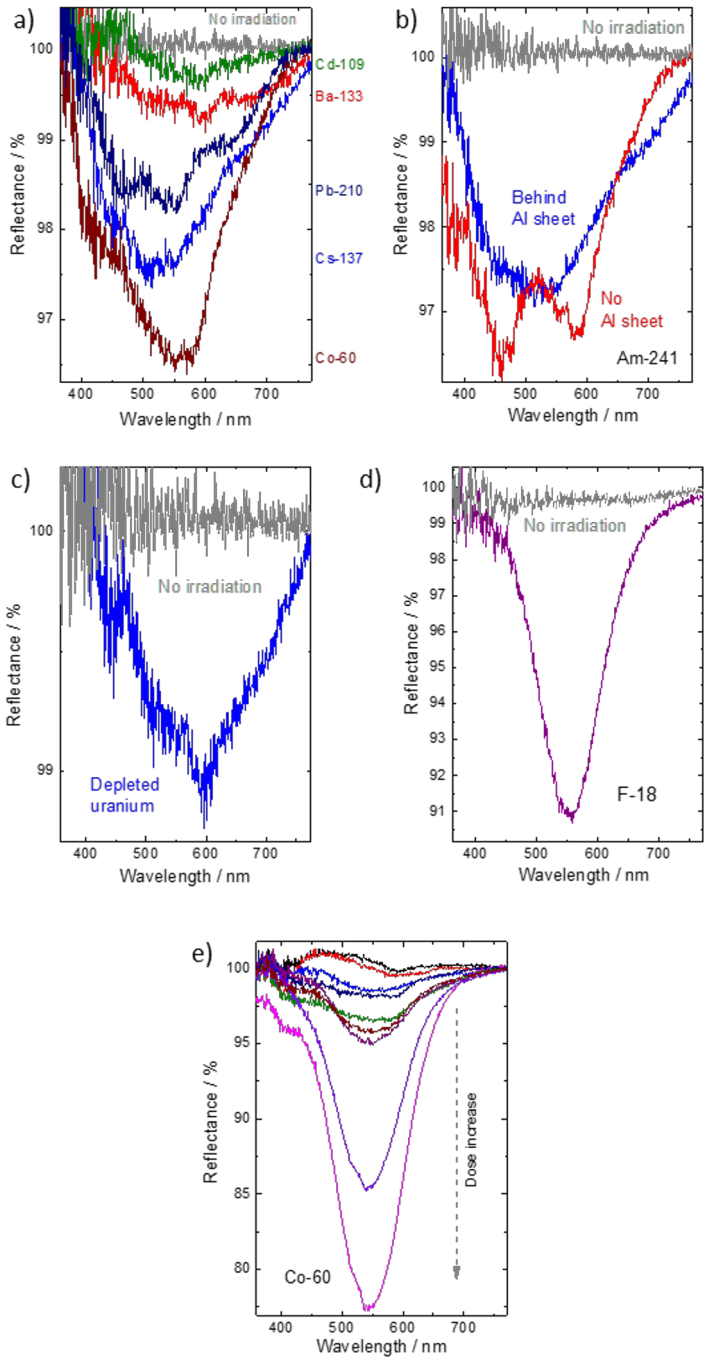

Figure 22. Reflectance spectra of **a)** gamma-irradiated Na hackmanite, **b)** gamma- and alpha-irradiated Na hackmanite from a ^{241}Am source, **c)** gamma- and alpha-irradiated Na hackmanite from a depleted uranium source, **d)** beta radiation-irradiated Na hackmanite, **e)** Na hackmanite with irradiation from a ^{60}Co source. Reproduced from **II** with permission from the Royal Society of Chemistry.

4.3 Gamma radiation coloration effects with ^{60}Co

Na, Br, K, Li, and Rb hackmanite samples were subjected to air kerma values of 200, 1000, 3000, 5000, and 7000 Gy from a ^{60}Co source (gamma photon energies 1.1732 and 1.3325 MeV) and their reflectance spectra were measured within 30 minutes after stopping the exposure. Figure 23 shows the coloration of the samples after the exposure to the high-activity radiation source.

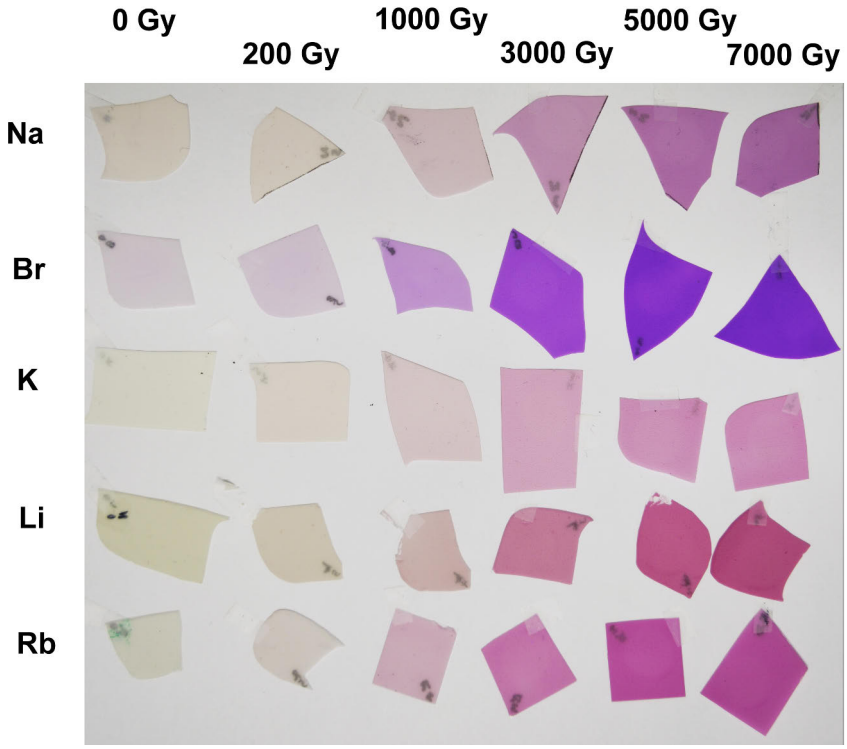

Figure 23. The irradiation matrix of Na, Br, K, Li, and Rb hackmanite films, showing the increase of coloration as a function of air kerma values. Figure adapted from **II** with permission from the Royal Society of Chemistry.

The coloration behaves multiexponentially as a function of dose, as in UV and X-ray coloration (Figure 12, Figure 13a and [19]), and as is visible in Figure 23, the Br hackmanite samples show the deepest coloration. This was also confirmed from the coloration intensities that were calculated from the integrals of the reflectance spectra shown in Figure 24a. When these spectra are normalized (Figure 24b), there is a clear broadening of the typical tenebrescence absorption band as a function of dose. The determination of dose-dependent broadening is shown later in the Applications section, in Figure 36.

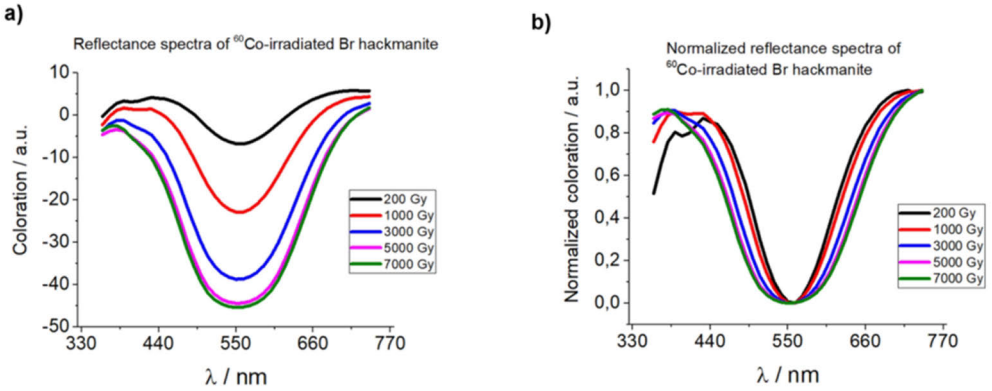

Figure 24. a) Reflectance spectra of Br hackmanite samples that have received 200, 1000, 3000, 5000, and 7000 Gy. **b)** The spectra normalized, showing additional bands.

4.3.1 Spectral characteristics of the absorption band broadening

When looking at the UV-, X-ray-, and gamma-colored samples, initially there seems to be no visible difference in them, as is shown in Figure 25b. However, when the reflectance spectra are measured from these samples, there are quite substantial differences, especially the broadening caused by gamma radiation (Figure 25c). To study the behavior of the gamma-induced broadening of the reflectance spectrum, Na hackmanite's optical bleaching spectra were recorded from a sample that had received a dose of 7000 Gy.

To study the color centers further, the coloration fading spectra (Figure 25d) and curves (Figure 25f) were also measured, which revealed that the red and blue parts in the gamma-colored sample have different bleaching energies and lifetimes compared to UV-colored (Figure 25e): for the UV-colored, the fading of the main peak (530 nm), red part (650 nm), and blue part (450 nm) is a single-component function with lifetimes of 16.4 ±0.1, 14.8 ±0.2, and 13.5 ±0.2 min, respectively. The gamma-colored sample's main peak's fading is at least a two-component function with lifetimes of 14.9 ±1.8 (30% amplitude) and 187 ±67 min (30% amplitude). As can be seen from the values, the former component is similar to the UV-induced fading and can be assigned to the same color center. The interesting red and blue parts in the gamma-colored sample has lifetimes of 206 ±41 and 229 ±66 min, respectively, which leads to the assumption that the main peak's second component and the red and blue bands are interlinked.

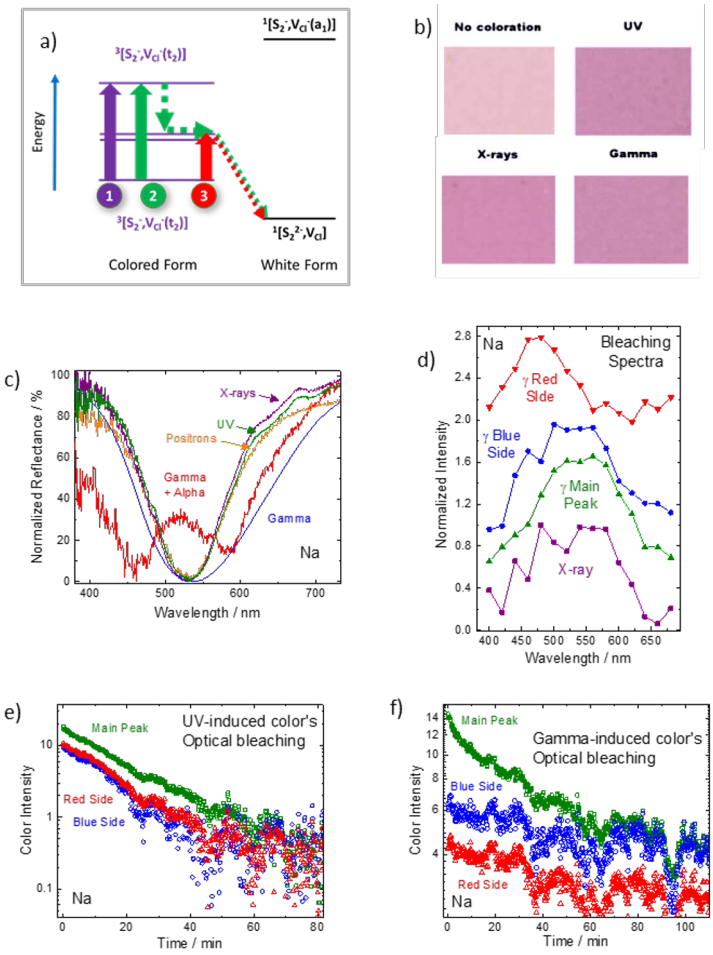

Figure 25. a) The mechanism of tenebrescence in hackmanites. **b)** Photographs of non-colored, UV-, X-ray-, and gamma-colored Na hackmanite. **c)** The normalized reflectance spectra of Na hackmanite that has been subjected to X-rays, UV, gamma + alpha, and gamma radiation, showing the braodening effect in samples with gamma exposure. **d)** The bleaching spectra of Na hackmanites with gamma (different components of the spectrum in red, blue, and green) and X-ray exposure. **e)** The optical fading curves of a UV-colored Na sample. **f)** The optical fading curves of a gamma-colored Na sample. Reproduced from **II** with permission from the Royal Society of Chemistry.

4.3.2 Origin of the red and blue bands

To gain information about the peak broadening effect and origin of the red and blue bands in a gamma-colored sample, the reflectance spectra from the samples presented in Figure 23 were analysed. From the data in Figure 26a, it can be seen that the broadening occurs as a function of gamma radiation dose, and the additional band can be seen especially from the dotted line showing the difference spectrum of a Na hackmanite sample that have received 200 and 7000 Gy. The figure also shows

a reflectance spectrum of a UV-colored sample, which does not possess the additional red and blue bands.

Earlier studies have assigned absorption bands at 465 and 595 nm in ultramarine, $Na_8Al_6Si_6O_{24}(Cl,S)_2$ (S = S_3^-, S_2^-), to S_3^- and S_2^-, respectively. [204] As hackmanite has a similar structure to ultramarine, it is likely that both S_3^- and S_2^- could also exist in hackmanite. However, the computational results suggest that the absorption of these sulfur species in hackmanite would occur at 385 nm for S_2^- and at 585 nm for S_3^-. Therefore, it is unlikely that the two additional peaks observed in hackmanite's spectra are caused by S_3^- and S_2^-. This was verified with EPR and Raman measurements; the EPR spectra of UV, X-ray-, and gamma radiation-colored $Na_8Al_6Si_6O_{24}(Cl,S)_2$ samples (Figure 26b) showed little difference compared to each other, and they all exhibited the F-center signal at *g* value 2.0 [4]. There are also additional and expected signals from an iron(III) impurity at 2.12, 2.17, and 2.24 [205,206]. The most important aspect of the spectra is the absence of signal at ~2.03, which would originate from S_3^- [207,208] The Raman spectra (Figure 26c) also confirm that there is no signal from the S_3^- species, which is expected to manifest at 548 cm^{-1} [207].

In addition to the NaCl results from X-ray irradiation tests showing the NaCl phase leaving the sodalite structure (Figure 15d), previous research on ion mobility in hackmanites has revealed that Na ions can migrate between *β*-cages [21]. While these subtle changes in the color center can hardly be measured with satisfactory accuracy using experimental techniques, a hypothesis where the color center changes from Na_4V_{Cl} to Na_3V_{Cl} was researched with TD-DFT calculations. The *β*-cage with Na_4V_{Cl} and Na_3V_{Cl} are shown in Figure 26d, and their respective simulated absorption spectra in Figure 26e. Similar to what the experimental reflectance spectra have shown in the gamma radiation-exposed samples, the red component from the Na_3V_{Cl} dominates the absorption spectrum compared to the blue component. This thus suggests that the additional bands indeed originate from a distorted color center, Na_3V_{Cl}.

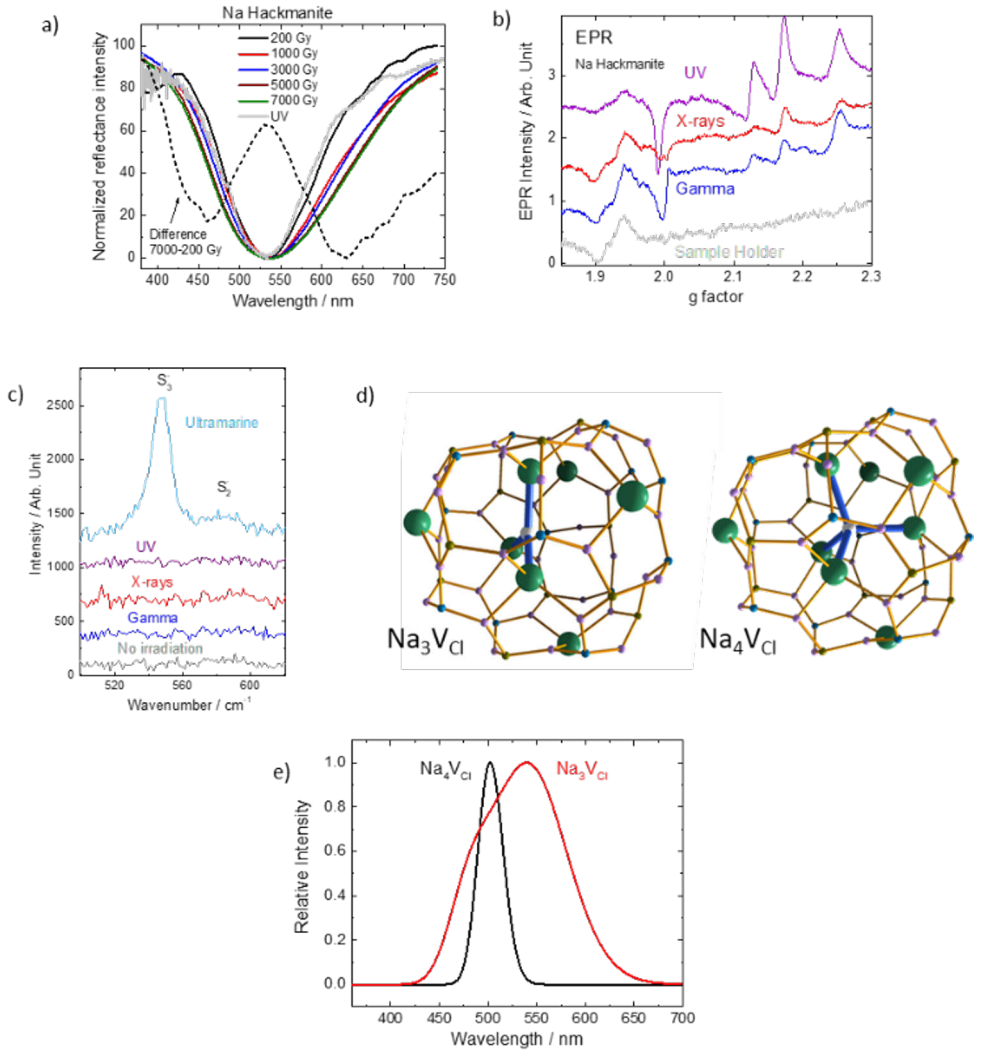

Figure 26. a) The gamma-exposed Na hackmanite's reflectance spectra with a difference spectrum (dotted line) of samples exposed to 200 and 7000 Gy. **b)** EPR spectra of UV-, X-ray- and gamma-irradiated Na hackmanite samples. **c)** Raman spectra of UV-, X-ray- and gamma-irradiated Na hackmanite samples. **d)** The visualisation of computational results of Na_3V_{Cl} and Na_4V_{Cl}. **e)** Simulated absorption spectra of the two color center forms. Reproduced from **II** with permission from the Royal Society of Chemistry.

4.3.3 Gamma radiation-induced color centers

To research the possible mechanism of the coloration, the gamma radiation-induced coloration was compared with X-ray-induced. In the X-ray-induced coloration, the mechanism for high-energy radiation was hypothesized to be caused by a scintillation-type electron–hole torrent that leads to the formation of color centers

after thermalization. The X-ray and gamma radiation coloration yields were compared by investigating the color intensity as a function of absorbed dose using ~22 keV X-rays and ^{60}Co emission. The results (Figure 27a) indicate a difference in the coloration, which can be explained with the fact that the unfiltered X-rays originating from the XRF device's Ag tube that was used in the tests also contains lower-energy bremsstrahlung, whereas the standardized ^{60}Co source only produced two characteristic gamma radiation emission lines accurately, with no other emission. However, despite these differences it seems that the color yield is in the same order of magnitude, which leads to the assumption that the coloration is caused by the same mechanism as with X-rays, which is shown in Figure 27b.

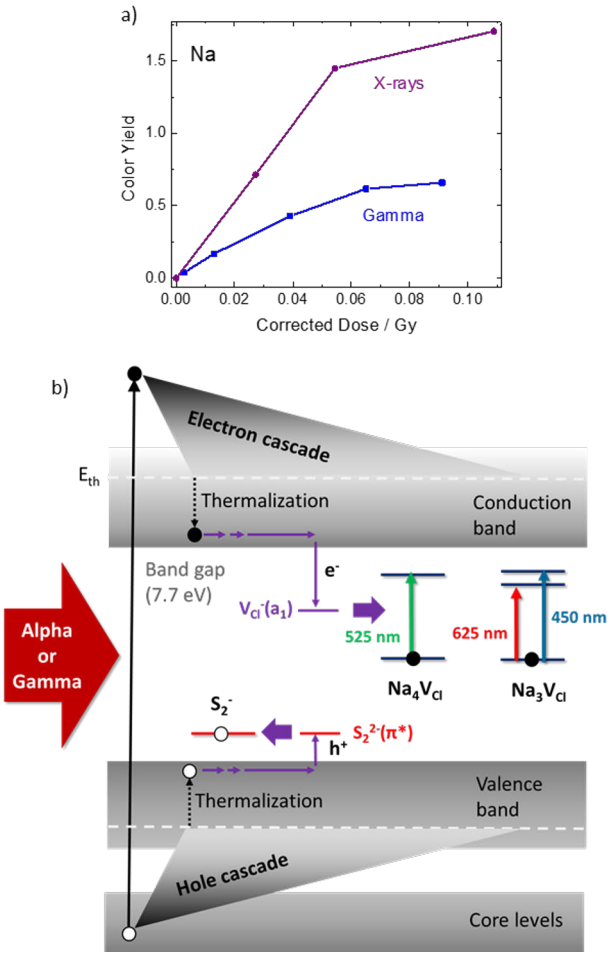

Figure 27. a) The coloration yield of Na hackmanite that has received X-rays and gamma rays, both corrected with the mass attenuation factor of hackmanite. **b)** The mechanism of both high energy radiation-induced coloration in hackmanites. Reproduced from **II** with permission from the Royal Society of Chemistry.

Since alpha and beta radiation have energies much higher than UV, it can be assumed that the coloration induced by them are also caused by the same mechanism as with X-rays and gamma radiation. If the energy is high enough, some of the Na_4V_{Cl} color centers transform into Na_3V_{Cl}, thus it can be assumed that the mechanism of color center formation depends on the energy rather than radiation type.

4.3.4 Gamma exposure memory

When the recolorability of a gamma-exposed Na hackmanite film was tested (Figure 28a–c), a serendipitous finding was discovered: not only does the gamma-colored sample color perfectly normally with UV after bleaching with white light, but also its additional absorption bands manifest again (Figure 28d). This means that the color center distortion caused by gamma radiation is a stable structure that can be harnessed for practical purposes, which is discussed more in detail in the Applications section. To confirm the broadening portion, reflectance of a hackmanite sample from around a Th/U inclusion was measured (Figure 28e). This sample has been assumed to be exposed to gamma emission from Th and U for more than 200–250 million years, which is the latest marble formation age in the basic rock of the inclusion. [209,210]

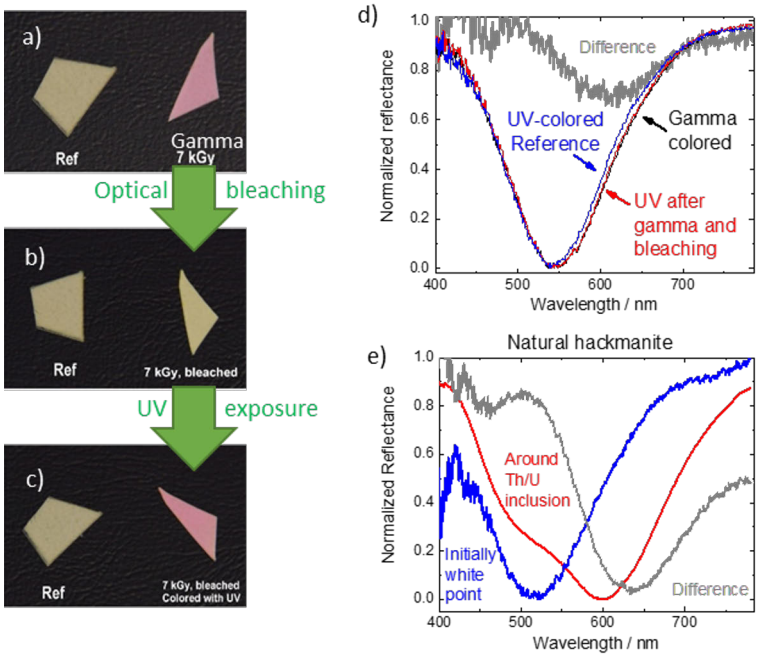

Figure 28. a–c) Photographs of a gamma-colored (7000 Gy) sample being bleached with light and colored again with UV. **d)** Reflectance spectra of a gamma-colored sample, the same sample after bleaching and recoloring with UV, and a UV-colored reference that has not received any gamma radiation showing that the gamma-colored sample ”remembers” the previous gamma exposure. **e)** Reflectance spectra of a natural hackmanite found near a Th/U inclusion. Reproduced from **II** with permission from the Royal Society of Chemistry.

4.4 Upscaled hackmanite synthesis

4.4.1 Purity of batches

The upscaled 100 g and 1 kg batches were analysed with XRD by isolating 19 aliquots from evenly-distributed spots in the sample masses. The purity was determined from the amount of unreacted NaCl as determined with Rietveld refinements. The results in Figure 29 indicate that the 100 g batch is better in terms of ability to color. The intra-batch coloration variation in the sample mass shows that the center parts color better than the edges, which may be due to clay minerals that have leached from the containers, or from the reducing gas not reaching the lower part of the edges like in the porous center. The purity variation shows inconclusive behavior, but the average of NaCl impurities in the 100 g and 1 kg batches are 9.1% and 11.7%, respectively, which means that the 100 g batch’s overall purity is higher. The XRD diffractograms in Figure 30 show that the purity is relatively high in both samples, meaning that the syntheses were successful.

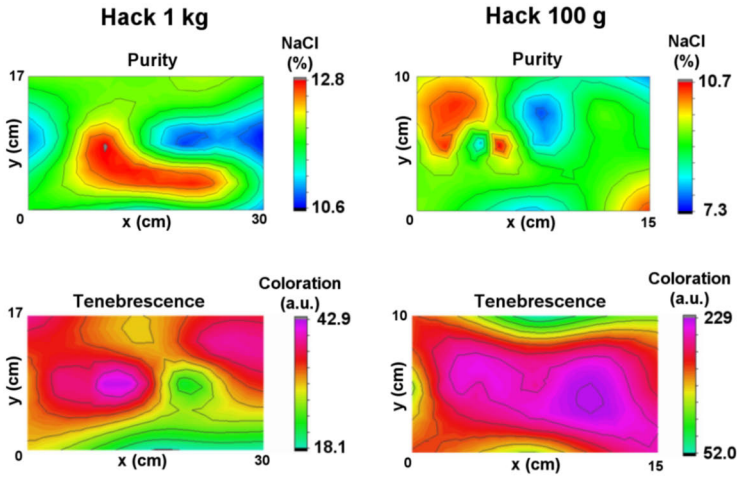

Figure 29. 2D purity and coloration maps of the 1 kg and 100 g batches. Image from **III**, licensed under CC BY 4.0 (https://creativecommons.org/licenses/by/4.0/).

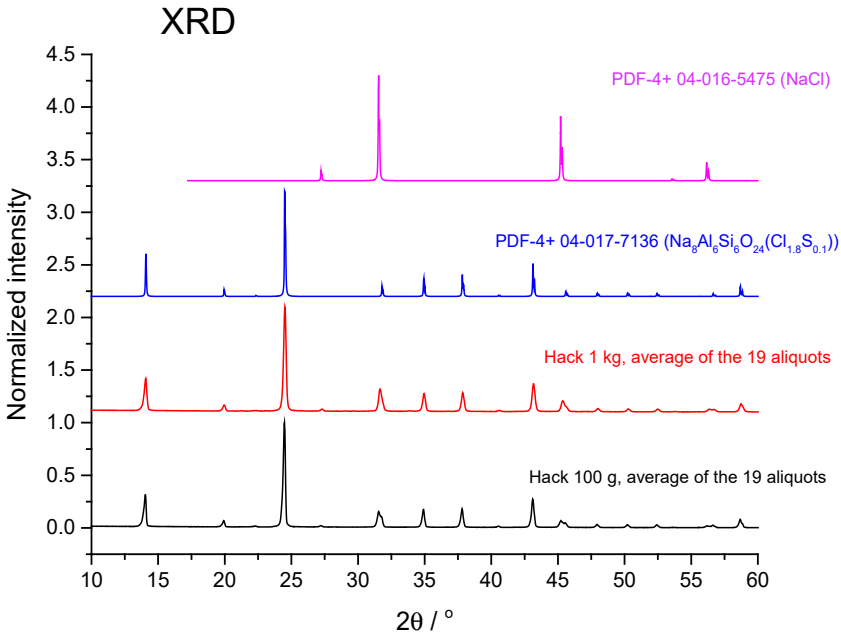

Figure 30. XRD diffractograms of the 100 g and 1 kg batches, and their matching phases from a PDF-4+ database. Image from **III**, licensed under CC BY 4.0 (https://creativecommons.org/licenses/by/4.0/).

In order to remove the excess NaCl, the samples were washed five times with deionized water, their NaCl content Rietveld-refined and coloration measured after

each washing. The washing waters were also measured for NaCl and hackmanite content with XRF; the less hackmanite there is in the water, the more advantageous it is for the washing procedure. In Figure 31a, the purity increases after each successive wash cycle, whereas the coloration is virtually unaffected (there is only ±5% variance, which falls within the boundaries of measurement error). Figure 31b shows the washing water's analyte content, which supports the fact that NaCl indeed leaves the structure, and only a very small part of the hackmanite mass is transferred into the water.

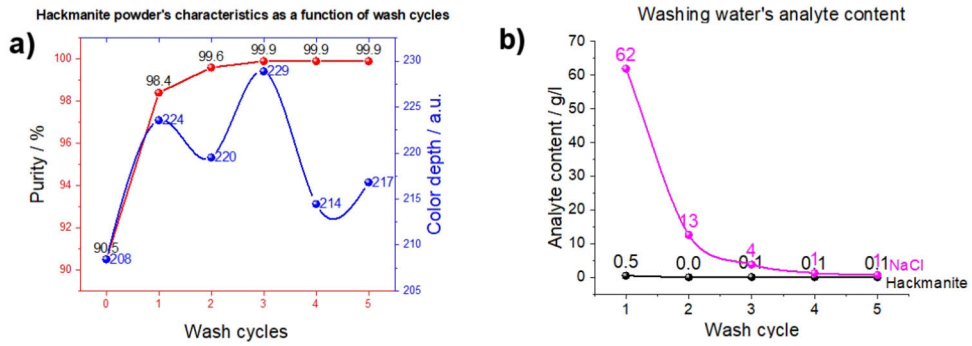

Figure 31. a) The Rietveld-refined purity (red) and coloration depth (blue) as a function of performed wash cycles. **b)** The NaCl and hackmanite contents of the washing waters of a). Images from **III**, licensed under CC BY 4.0 (https://creativecommons.org/licenses/by/4.0/).

4.4.2 Iron as an impurity and its effect on luminescence

Fe^{2+} ions are known to be effective quenchers of luminescence in many luminescent materials, including organic fluorophores and semiconductor quantum dots. This is because iron ions can act as non-radiative deactivators of excited states, leading to a decrease in luminescence intensity and quantum yield. The quenching effect of iron ions can be attributed to their ability to accept electrons from excited states of luminescent materials, which results in the formation of a charge transfer complex, in which the excited state energy is dissipated as heat instead of being emitted as light. In addition, iron ions can also promote the population of non-emissive states, which further contribute to luminescence quenching in several materials, including sodalites. The degree of quenching by iron ions can depend on multiple factors, e.g. the concentration of iron ions, the type of luminescent material, and the nature of the excited states involved. [3,211–213]

The 1-kg batch did not have a lid to protect the sample mass from contaminants in the steel-lined furnace, but the second batch, i.e. 100 g, had one. XRF was used to measure the iron content of the surface and bulk of the 1-kg batch, and the surface + bulk of the 100 g (because the depth of the sample mass was so low that it was not

possible to separate the surface and bulk). The XRF spectra in Figure 32 show that the 1-kg batch suffers from iron contamination at the sample surface, but the bulk's content is almost at the same level as in the 100-g sample. This means that the surface layer of the 1-kg batch has acted as a protective cover for the bulk mass, whereas the actual lid in the 100-g sample has protected the whole sample. Thus, it is advantageous to use a lid when making large batches in a steel-lined oven to mitigate Fe contamination. Also, as an additional detail, in Figure 33 it can be seen that the 1 kg sample's surface layer has severely decreased optical properties.

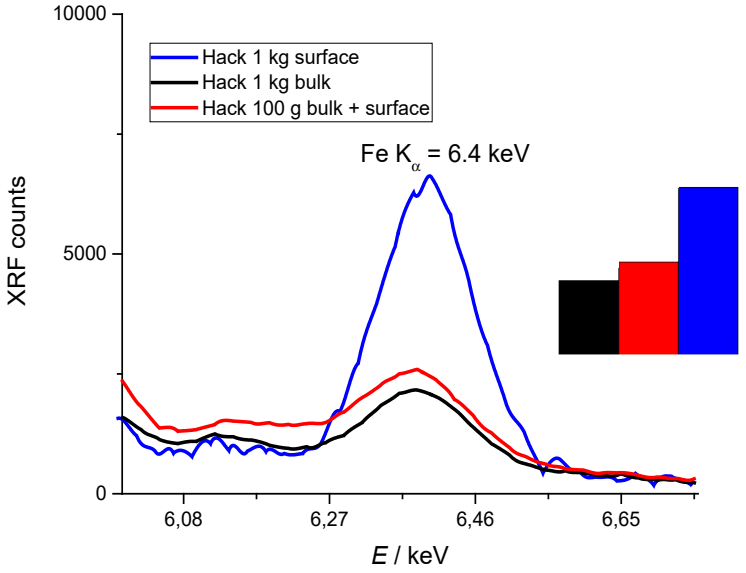

Figure 32. XRF spectra from the Fe K_α region of the 1-kg sample's surface (blue), bulk (black), and 100-g sample's bulk + surface (red). Higher intensity = higher Fe content. Inset: peak integrals taken from the XRF spectra, showing the quantitative relationships of the Fe contents. Image from **III**, licensed under CC BY 4.0 (https://creativecommons.org/licenses/by/4.0/).

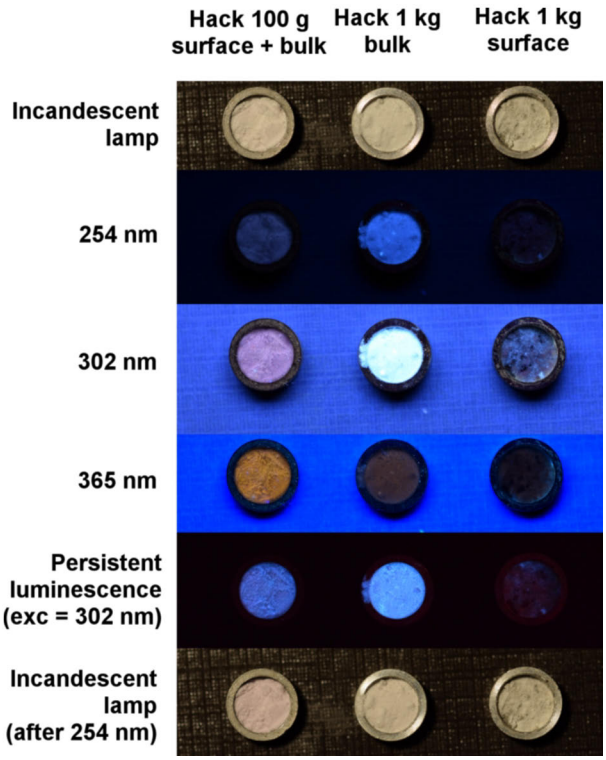

Figure 33. Photographs of the 100-g and 1-kg samples under different exposure conditions. Image from **III**, licensed under CC BY 4.0 (https://creativecommons.org/licenses/by/4.0/).

The differences in coloration could be due to competitive electron excitation processes: the stronger the luminescence, the more there are Ti^{3+}–V_O pairs to absorb the UV radiation [3,18] and the less there are free UV photons for the electron excitation for the S_2^{2-}–V_{Cl} process, which is responsible for the coloration. [18,19]

5 Applications

5.1 Radiation dose determination with hackmanites

As the coloration in hackmanites occurs as a function of X-ray dose logically following a multicomponent function behavior, it can be harnessed as a dose determination device. For measuring the absorbed dose from e.g. a ~22 keV unfiltered X-ray beam, it could be determined by making an irradiation series and plotting the sample's coloration as a function of dose, thus acting as a visual dosimeter. Since there are substantial differences in the absorption of high-energy radiation with different photon energies due to e.g. abrupt changes in the mass attenuation coefficients from absorption edges, the calibration curves must be constructed with individual radiation sources precisely. Figure 34 shows an example where color intensity has been plotted against unfiltered ~22 keV X-ray dose using 8 data points. The doses were measured using a Thermo RadEye B20-ER dosimeter.

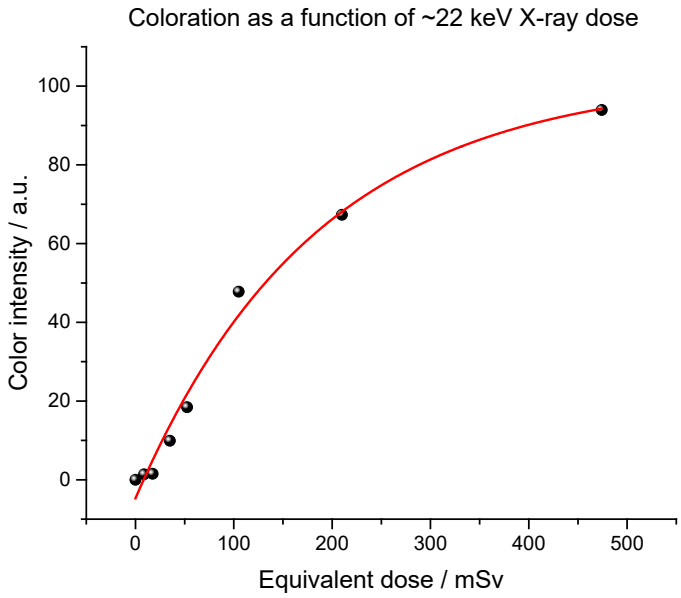

Figure 34. An irradiation series of Na hackmanite using 22 keV X-rays. Figure adapted from **I** with permission from John Wiley & Sons, Inc.

In a synchrotron source, a similar dose response curve can be constructed with air kerma values when the amount of incident photons is known from the photon counter found at the end of the beamline. To convert the photons to doses and dose rates inflicted upon the material, monoenergetic photon conversion coefficients are used. The International Commission of Radiation Units and Measurements (ICRU) has provided a list of air kerma area to unit fluence dose area product coefficients K_a Φ^{-1} (unit pGy cm^2) from 10 keV to 10 MeV [116], but other conversion tables can also be used, e.g. Veinot *et al*. has provided an extended set with a useful fitting function with an accompanying equation [214].

For example, the dose of a 10 keV monoenergetic X-ray beam with a $6.00 \cdot 10^{10}$ photon fluence on a sample area of 0.0500 mm^2 can be calculated with Eq. 3 and Eq. 4:

$$\frac{K_a}{\Phi} = C \Leftrightarrow K_a = C * \Phi \quad \text{(Eq. 3)}$$

$$\Phi = \frac{dN}{da} \quad \text{(Eq. 4)}$$

C = dose area product coefficient (7.43 pGy cm^2 for 10 keV [116])
K_a = air kerma in pGy
Φ = unit fluence
dN = photon count
da = exposure area in cm^2
By placing known values into Eq. 3 the dose can be calculated:

$$K_a = C * \frac{dN}{da} = 7.43 \text{ pGy cm}^2 * \frac{6.00 * 10^{10}}{0.000500 \text{ cm}^2} = 892 \text{ Gy}$$

Similar curves can be constructed with gamma radiation. In Figure 35, the coloration rises as a function of air kerma from a ^{60}Co source exposure. As can be seen from the data, the coloration is different for all samples; as Br hackmanite has the broadest dynamic range in gamma coloration, it is an ideal material for determining multi-kGy doses using the equation from its fitting function. As the material colors in the visible range, the dose can easily and instantly be determined inexpensively e.g. with a digital camera or a mobile application utilizing the phone's camera.

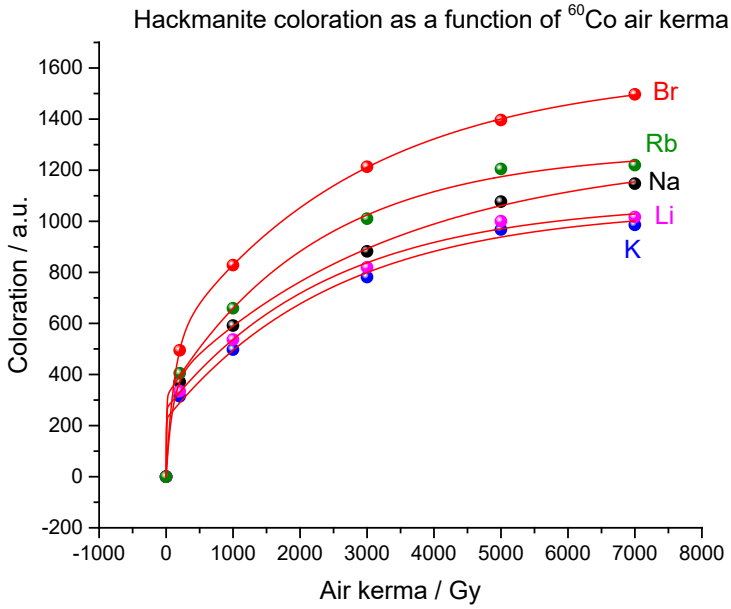

Figure 35. Five hackmanite samples colored with a ^{60}Co source. The coloration rise follows a two-component function for all samples. Figure adapted from **II** with permission from the Royal Society of Chemistry.

However, as the main peak broadening due to the formation of Na_3V_{Cl} also occurs as a function of dose, it can be used as an internal standard in the determination of dose, i.e., the dose is determined from the ratio of different parts of the spectrum (Figure 36). With this method there is no need to construct a batch-specific lookup table since the original trap density (which changes from batch to batch) does not play a role, i.e. the overall coloration information is not needed at all. The disadvantage of this method is the cost, since accurate determination needs a spectrometer to scan the reflectance spectrum from the whole visible range.

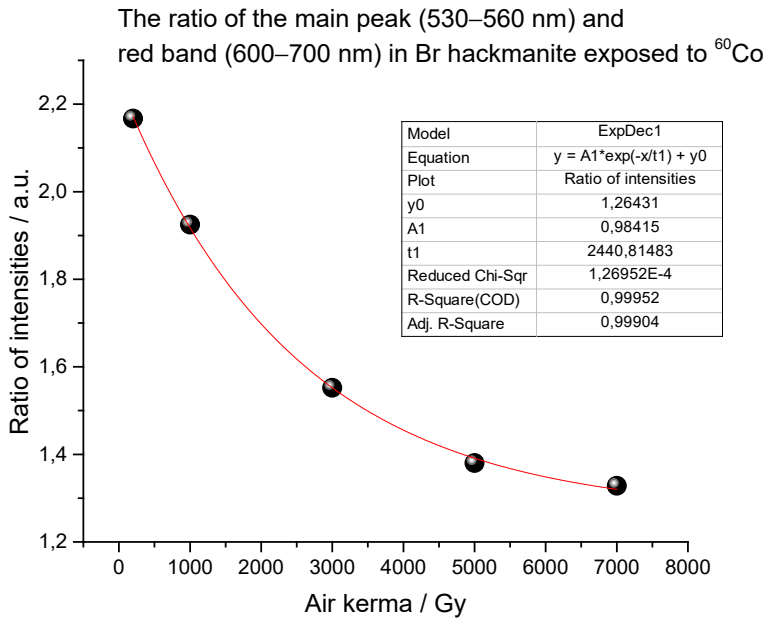

Figure 36. The ratio of the main peak and the red band of the reflectance spectrum in Br hackmanite exposed to 0.2, 1.0, 3.0, 5.0, and 7.0 kGy using a ^{60}Co source. Figure adapted from **II** with permission from the Royal Society of Chemistry.

In radiation settings involving living creatures the use of hackmanite is not applicable due to the coloration occurring only at a kGy level; for comparison, in humans a whole-body ionizing radiation dose has an LD_{50} value of 4.1 Gy [215], and a dose of 90 Gy would result in an instant death [216]. However, the described techniques could be applied for making a radiation dose distribution map in an industrial food irradiation station for e.g. onions and potatoes [217] by having e.g. nine hackmanite films distributed evenly under a radiation source, and then measuring their coloration after the irradiation. The coloration values would then be compared to the calibration series, and the doses would then be solved (an example graph is shown in Figure 37).

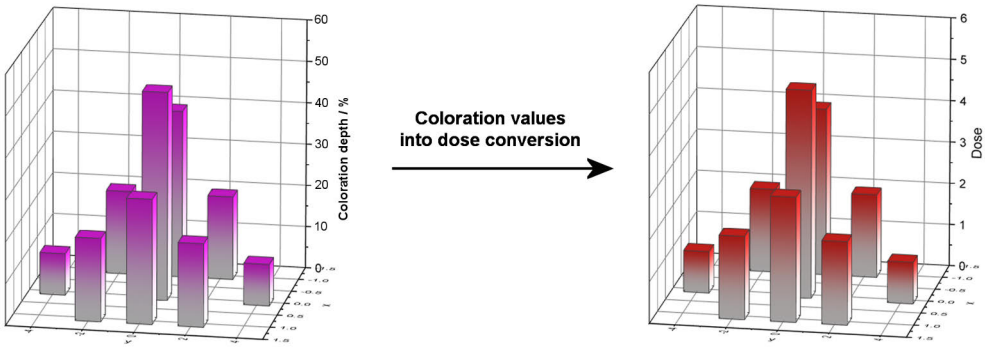

Figure 37. An example of a radiation dose map constructed from coloration values using a calibration series. Figure adapted from **II** with permission from the Royal Society of Chemistry.

5.2 Hackmanite in X-ray imaging

Since X-rays have a tendency to penetrate different materials to different depths depending on their mass attenuation coefficients and hackmanites show a coloration response to X-rays, these materials can be used for X-ray imaging. The imaging capabilities of hackmanite depicted in Figure 38 prove that hackmanite can be used for imaging inanimate objects such as dead insects or electronics.

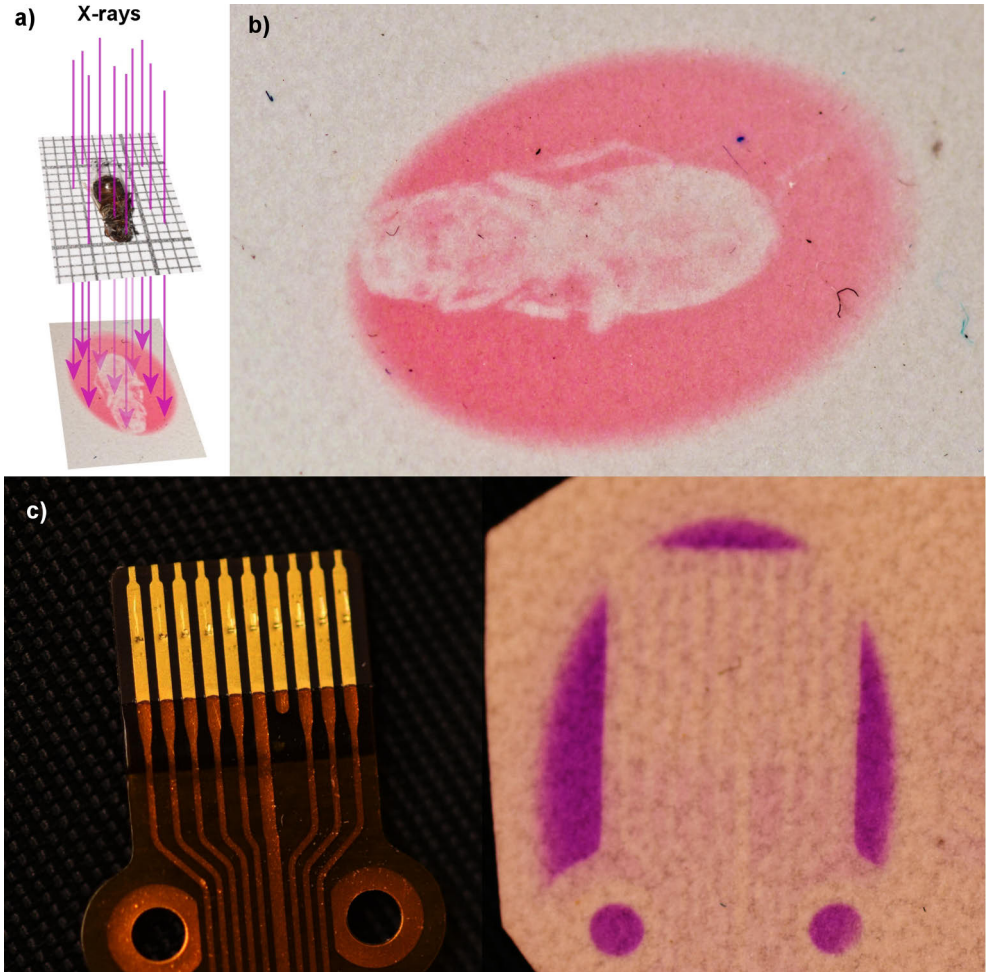

Figure 38. a) The principle of imaging a deceased ant specimen with ~22 keV X-rays using a hackmanite film: the X-ray photons that are absorbed in the creature's body do not hit the hackmanite detector, whereas the transmitted photons color the film. **b)** The X-ray image using Na hackmanite captured with a digital camera. The overall equivalent dose was 105 mSv. **c)** A Nokia 9210 Communicator's data transmission cable imaged using Br hackmanite: the wiring can be seen in the X-ray image.

Since gamma rays color hackmanite in a similar way as X-rays, the X-ray imaging principle can be used in gamma imaging as well. The disadvantage in hackmanite is that it contains only relatively light elements and thus its response requires very high doses due to its gamma radiation transparency.

5.3 Using hackmanite as a photographic film

In previous chapters, hackmanite's use as a detection material for the direct forward reaction, i.e. charge carrier trapping in the crystal defects, has been established for UV and high-energy radiation. However, the backward reaction where the trapped electron is liberated from the trap, can also be used for detection of visible light since the coloration bleaches as a function of photon exposure.

For the applicability of visible light detection, two films were made: mixed in silicone (20% of hackmanite powder and 80% of Dow SYLGARD™ 184) and as an organic film that consisted of ~73% of hackmanite. These films measuring 6 × 9 cm were first colored with a 9-W 254 nm UV lamp (model 博立恩 ZW9D12W-H145) for 5 minutes (Figure 39a) and then put into a VEB KWT Reflekta II medium format camera (Figure 39b and c) equipped with a Meritar 75mm *f*/3.5 lens.

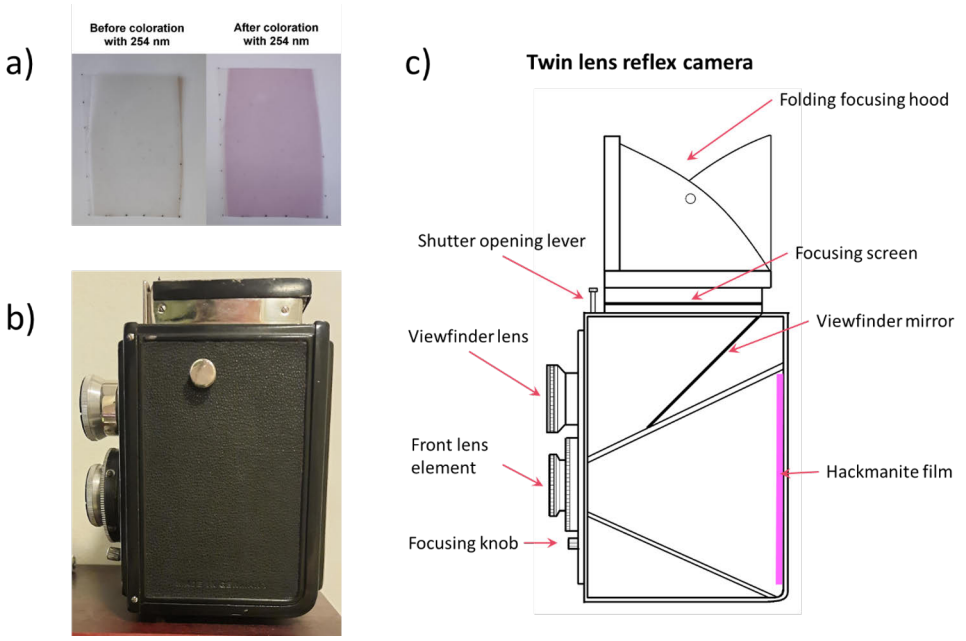

Figure 39. a) A silicone film before and after coloration with 254 nm UV. **b)** A VEB KWT Reflekta II camera. **c)** Schematics of the camera, showing the hackmanite film at the back of the exposure chamber. Image from **III**, licensed under CC BY 4.0 (https://creativecommons.org/licenses/by/4.0/).

The film was exposed for 20 h in Finnish summer. The performance of the silicone film is depicted in Figure 40, showing unsatisfactory results due to heavy Gaussian blur despite the camera lens being in focus.

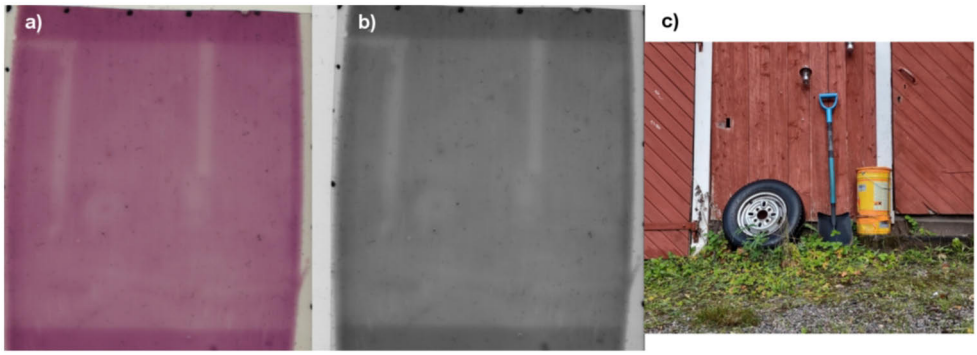

Figure 40. a) A 20-h exposure with the silicone film, showing heavy Gaussian blur. **b)** The image converted to greyscale. **c)** The actual setting. Image from **III**, licensed under CC BY 4.0 (https://creativecommons.org/licenses/by/4.0/).

The origin of the blurring in the silicone film could be due to the silicone itself being a transparent medium where photons scatter due to the distributed hackmanite crystals. This aspect was tested with an image analysis technique where the pixel values across a light-transmitting slit were plotted as a function of x coordinates, and the data in Figure 41 confirm that there is 18% more direct scattering in the silicone film compared to the organic film.

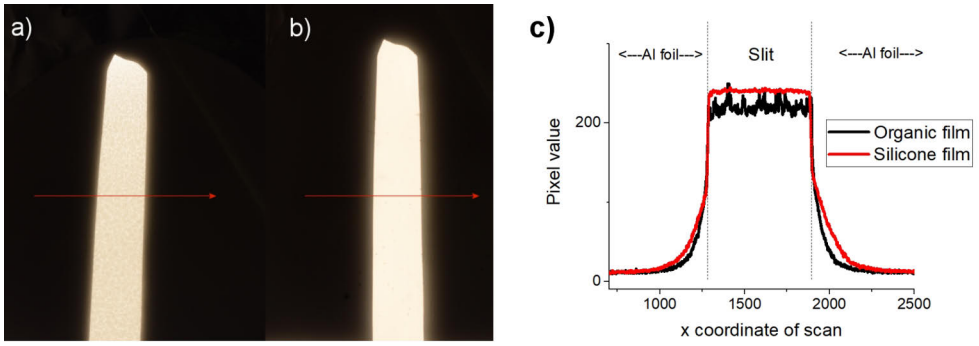

Figure 41. A light scattering test of **a)** the organic film and **b)** the silicone film where the pixel values from across the Al foil slit were taken to form the graph in **c)**. The light scattering is 18% less in favor to the organic film. Image from **III**, licensed under CC BY 4.0 (https://creativecommons.org/licenses/by/4.0/).

There was a substantial difference when the organic film was used as the photographic medium. The 20-h exposure results can be seen in Figure 42. Compared to the silicone film, the clarity and sharpness has increased to a point where details can be seen effortlessly.

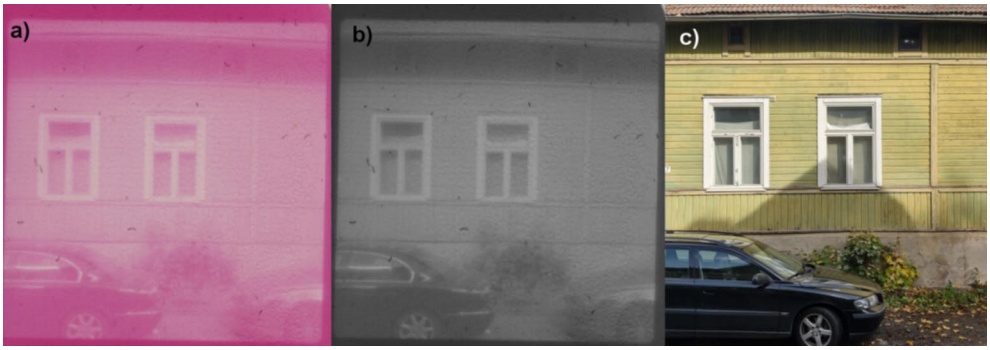

Figure 42. a) A 20-h exposure using the organic film. **b)** The image converted to greyscale. **c)** The actual setting, which was changed slightly due to the photo being taken some hours after the exposure. Image from **III**, licensed under CC BY 4.0 (https://creativecommons.org/licenses/by/4.0/).

After scanning the film, it was colored again and used as a film for taking more photos that are shown in Figure 43. The image a) suffers from overexposure due to lighting condition changes during the exposure, and image c) shows to be underexposed, which may be due to hackmanite's low level of sensitivity to red light (Figure 10a), which is the dominant color in the image. However, all in all the film proved to function as a reusable photographic film. This type of film does not need any development chemicals since the result is easily seen with eyes, and the film base is also gelatin-free. Both of these properties are usable in tackling the sustainability issues in the film photography industry, which has been showing a resurgence for some years now in the 2020s [218].

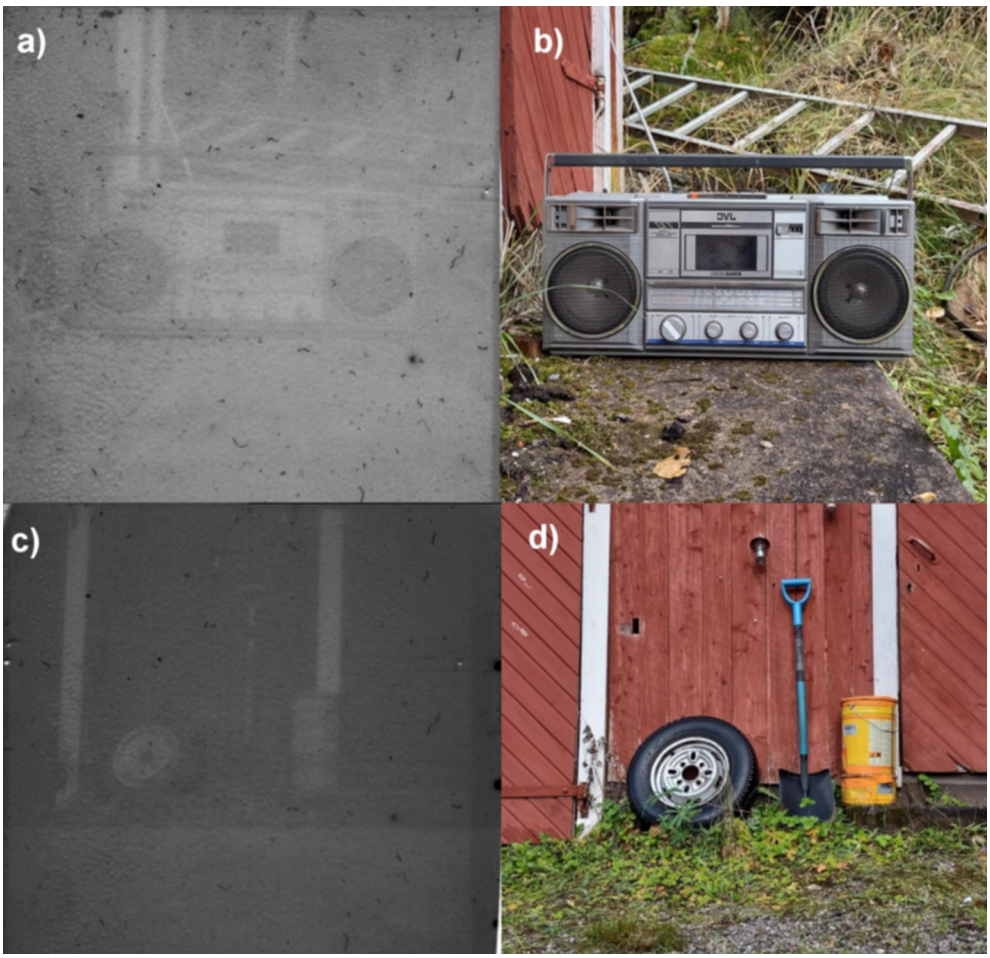

Figure 43. a) A 20-h exposure taken with the same film as in Figure 42. **b)** The actual setting of a). **c)** Another exposure using the same exposure time after scanning the image shown in a). **d)** The actual setting of c). Image from **III**, licensed under CC BY 4.0 (https://creativecommons.org/licenses/by/4.0/).

The photographic exposure speed of the films and the hackmanite powder was determined by measuring their sensitometric Hurter–Driffield curves under a constant light source. Normally, the curves are constructed densitometrically using the optical density of a given wavelength as a function of exposure in lux seconds, but here the curves were constructed from the absorption maxima (540 nm) of the reflectance spectra. As is normal for photographic films, the curves show the characteristic four regions, i.e. the underexposed part, the linear region (the contrast region), the overexposure region and the last dip i.e. the region of solarization. [219,220] The data in Figure 44 show that the organic film is the fastest photographic

medium since its contrast region begins at an earlier exposure region than the others, but the powder has the broadest applicable exposure region.

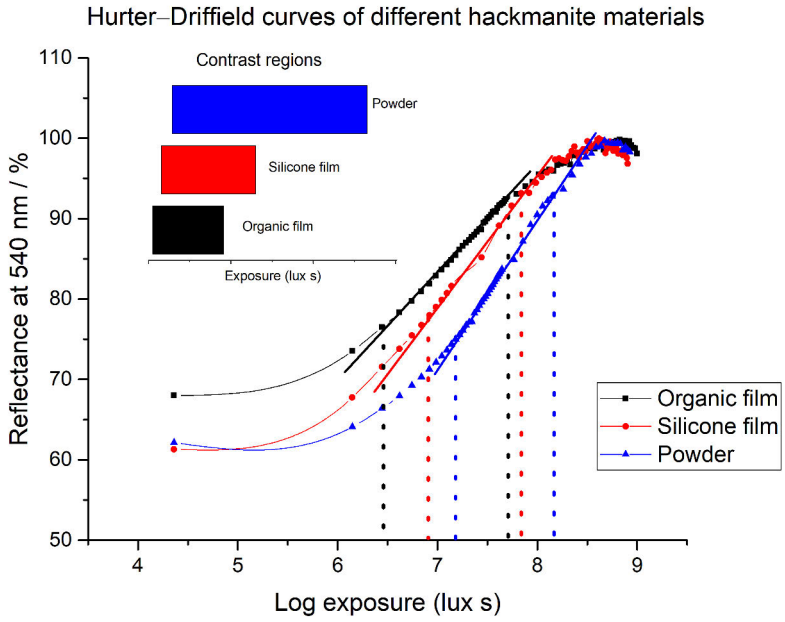

Figure 44. Hurter–Driffield curves of the organic film, the silicone film, and the powder. Inset: The contrast regions (the linear regions of the curves, marked with dotted lines) of the three types of materials. All curves are vertically aligned to 100% level. Image from **III**, licensed under CC BY 4.0 (https://creativecommons.org/licenses/by/4.0/).

If hackmanite would be used in a regular 36-exposure 35 mm film that has an exposure area of 24 mm × 36 mm (with 2-mm margins on each side), the overall exposable area would be 32800 mm^2. One gram of hackmanite cast into the organic film (thickness 300 µm) format spreads to cover 5900 mm^2 (Figure 45), thus there would be a need of 5.6 g of pure hackmanite powder for one roll of film. With the same logic, one medium format 120 film roll (56 mm × 56 mm · 12 exposures) would require 6.6 g of hackmanite.

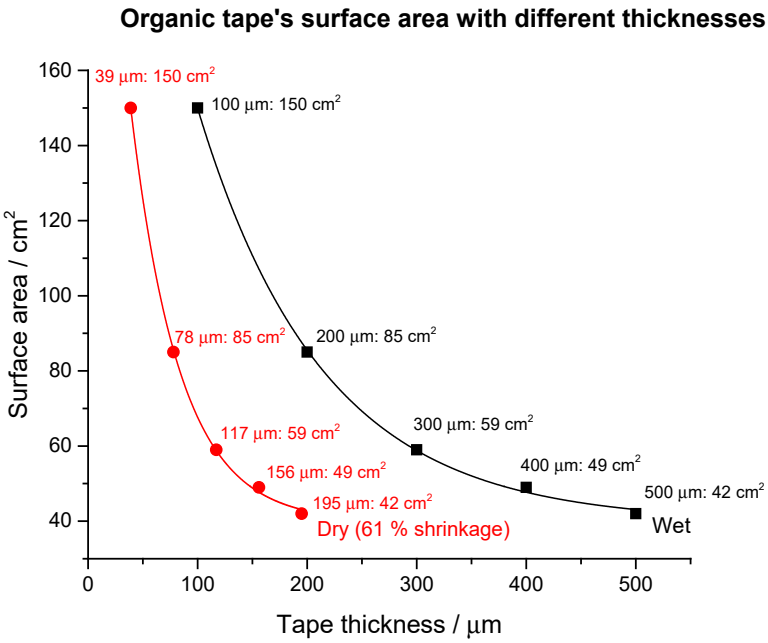

Figure 45. The surface area of the organic film as a function of wet (black) and dry (red) thickness. Image from **III**, licensed under CC BY 4.0 (https://creativecommons.org/licenses/by/4.0/).

6 Conclusions

Even though hackmanite's coloration under high-energy radiation has been known for decades, there have been no mechanistic approaches to study what actually happens during the coloration with these radiation types. The rather slow coloration and low coloration yield under high-energy radiation is due to a different mechanism than what has been established for UV-induced coloration throughout history. With both high-energy photons and nuclear/particle radiation hackmanite shows a mechanism similar to scintillation, yet contrary to typical light-emitting scintillation, part of the thermalized excited electrons and holes eventually recombine in color centers. Exposing hackmanite to X-rays with energies of <20 keV, the color centers show the same characteristics as in UV-induced coloration, however when a high-activity and high-energy gamma source such as ^{60}Co is used, some of the color centers are transformed from the normal Na_4V_{Cl} to Na_3V_{Cl} that shows absorption bands at the edges of the main absorption of ~540 nm. Interestingly, these additional bands can be used to determine the amount of radiation without the need for a coloration-dependent calibration series. Moreover, hackmanite "remembers" the gamma exposure since the deformed color centers are stable and manifest even after complete bleaching of the material; hackmanite only needs to be colored with UV to reveal this intriguing property.

In addition to studying the mechanistic properties, another aim of the experimental work was to focus on possible practical applications. X-rays were shown to color hackmanite well, and an imaging experiment with a deceased ant specimen and an electronic cable showed that hackmanite does possess a capability to function as an imaging material. And since synthetic hackmanite also exhibits strong coloration under gamma radiation, it can be harnessed as a visible dosimeter for high-activity gamma sources used in e.g. food sterilisation.

Hackmanite is increasingly being recognized for its potential applications in a variety of fields. For example, it has shown promise in tenebrescence imaging using X-rays or gamma rays, as well as leisure applications such as incorporating hackmanite into cellulose fibers to produce clothing that reacts to UV radiation or as the primary component in UV index meters. As a result, there is a growing demand for larger-scale production of hackmanite beyond what is feasible in a laboratory,

which was one aspect of the experimental work conducted. Phase-pure 1 kg and 100 g batches of tenebrescent hackmanite were obtained by heating them in an industrial retort furnace normally used for quenching heavy-duty metal objects in Hilamet Oy, Ylihärmä, Finland. Since the furnace was steel lined, it was shown that an unprotected sample mass has severe iron contamination, whereas a sample container that had a lid was shown to have greatly decreased level of impurities.

As a final curiosity, hackmanite was cast as flexible films that were used as gelatine-free photographic medium without the need of development chemicals. Although the exposure time, 20 h, is nowhere near practical ranges, this type of slow photography can be employed when e.g. taking ultra-long exposures from city centres or such. However, the most important aspect of hackmanite films is linked to other presented practical applications as well – the photochromism property does not weaken with repeated use, hackmanite consists of only abundant elements and is non-toxic.

Acknowledgements

This is the end… This thesis is the culmination point of my studies at the Intelligent Materials Chemistry Research Group (IMC) at the University of Turku under the Doctoral Programme in Physical and Chemical Sciences (PCS), which later became the Doctoral Programme in Exact Sciences (EXACTUS).

As with everything requiring personal growth, this journey has had its ups and downs, its more sluggish phases, and some faster ones as well. It would have consumed me completely without the people who have been there for me, assisted me, taught me, helped me, and steered me in the right direction.

First, I want to thank the reviewers of this thesis, Prof. Klára Hernádi and Prof. Andrew Beeby, for finding the time in their schedule to read this thesis and make very valuable comments. I also want to thank Prof. Adrian Finch sincerely for agreeing to be my opponent.

The first person to thank from our university is Prof. Mika Lastusaari who is leading our group's photonics team and knows everything about inorganic chemistry and things presented in this thesis. Mika has answered my questions and doubts with an astonishing level of expertise and supported me throughout the whole process. I got to know Mika's sense of humor during my PhD studies, and I must say that there is a major overlap of our senses of humor. Thanks for making the research not only exciting, but fun as well. Our crazy video projects for the research group were also something that was exciting and educational to do.

My research director, Prof. Carita Kvarnström, has been very helpful and kind with all the paperwork related to the PhD studies. I want to thank her for being so supportive throughout these years.

My colleague Hannah Byron deserves massive praises. She started her PhD work at the same time as me and was co-responsible for our students, who we at some point started calling "lab kids" or "children". She has also carried major burden for many of the students from the Turku Vocational Institute. With Hannah, we came up and improved many of the characterization techniques related to measuring the optical properties of hackmanites and learned a lot during those times. She contributed immensely to the improvement and organization of our lab, especially when we moved to Aurum, which I and the whole IMC are very grateful for.

In addition to Hannah, it was not easy for my other workmates to listen the sounds coming from my bulky 2001 Key Tronic keyboard. That's why I wish to express my apologies and gratitude towards Dr. Emilia Palo, Dr. Isabella Pönkkä, and Dr. Minnea Tuomisto. When you were doing your PhD, you identified yourselves as The Powerpuff Girls. When I came along, I became Mojo Jojo, the main antagonist of the show, because naturally the Professor's position was reserved for Mika! It was great to learn so many skills and draw so much knowledge from you three: Emilia and Minnea, your theses are very detailed, and it clearly shows that you excel in your field as hard-boiled professionals. Emilia took a leap to the unknown by continuing her path in the Faculty of Engineering which was founded just recently, and imagining how tough a job it has been to mould an entire field from scratch with limited resources, I can but give the biggest recognition. Minnea, I can't thank you enough for all the tutoring with lab equipment related to OSL and upconversion luminescence. Thanks to Isabella's important work on hackmanites, Hannah and I were able to carry on and expand the research from there. Isabella is now leading the scientific work as the Chief Scientific Officer in Pure Luminescence Technologies Oy, an example of what can be after the PhD. I'll be coming to collect the ad money for this later, Isabella (hehe just kidding!). I see each of you as a kind of an academic big sister. Thank you for taking me so warmheartedly into the group.

The next entity under the praise siege is IMC's metal-organic team. I would like to express my highest appreciation to Adj. Prof. Ari Lehtonen, Adj. Prof. Anssi Peuronen, Dr. Pasi Salonen, Dr. Esko Salojärvi, and my peer Doctoral Researcher Narhari Sapkota, exceptional individuals whose contributions to IMC's mutual, intelligent mission have been invaluable. Your unwavering dedication, outstanding discipline, and remarkable skills exemplify the finest qualities of the group. Ari's leadership and sense of humor makes the team to strive for metal-organic excellence, and coupled with our photonics team we really shine together. Anssi the XRD expert is a man who I share a mutual interest towards all technical stuff, and it was truly inspirational to visit his previous workplace in Jyväskylä to get the massive single-crystal XRD machine from there and chat about everything interesting during the drive. Narhari is an exceptional individual who always makes the whole room laugh with him, and he's also a hard-working metal-organic smith creating the most beautiful materials, and don't get me started on *hyppy tuntemattomaan*… Pasi and Esko, it was always a nice chat with you fellows. Your brutal humor – especially Esko's, as Pasi stated in his thesis – was very much appreciated while working in the windowless labs in Arcanum. Esko, I hope your Saab runs until at least 999 999 km so that we don't have to eat sillivoileipä anytime soon. He is now running Kemisteri Oy, a rising star in the field of optimizing industrial processes (once again, I'll be coming to get my ad money!). Pasi, you took a leap to the unknown in Jyväskylä just like Emilia, a very bold and admirable move as well!

Dr. Ian Machado and Dr. Leonnam Merízio are the latest additions to IMC, and they assimilated perfectly into the culture of our team from day one. You know it's always going to be a nice day when you meet these buddies in Aurum, not to mention when we go to a pub. Thank you Ian for setting the standard to include the word *serendipity* or some form of it in a thesis. I succeeded (p. 61). Thank you both also for introducing Brazilian delicacies cachaça and – most of all – paçoquitas.

Adj. Prof. Satu Mikkola has also had an impact on my path, and I want to thank her for the support. When I applied to the university as a student who hasn't gone to high school, she held the entrance exam and afterwards praised my answers, which was a really nice and important encouragement. Although we're living in completely opposite chemistry realities, we have still maintained a very good connection.

The two people working tirelessly in the basement of Arcanum, and later at different places in Aurum are one big reason why I got this far. I always thought I am good with technical stuff, but Mauri Nauma and Kari Loikas have such a level of technical knowledge that they just dwarf me completely. This thesis would not have happened without your help; that is something I can say very confidently. It's a pity that one cannot invite an inanimate lathe to one's post-doctoral party because it was the main character when I needed some custom parts for anything. And besides work stuff, thank you for giving advice on things like car repair, home renovation and other tech stuff.

And now that we're in the basement level, I must also thank Kirsi Laaksonen who has always been there to help me with chemical needs and mails. I remember the beautiful moment when were about to send 1 g of beryllium oxide to Tampere, and Kirsi called the shipping company just to hear that it costs about 400 € to send. We literally laughed at the price for 10 minutes after Kirsi hung up the phone.

Then it's time to thank our "kids": Roosa Vastamäki, Teppo Kreivilä, Pinja Santamäki, Sinna Lampinen, Natalia Antonova, Nina Rehnberg, Kirsi Miller, Samu Raunio, Bettiina Muurinen, Claudia Swain, Madara Tomele, Anni Nyman, Julia Kajander, and Ella-Roosa Suni. You have excelled in your own research projects to a point where we are only there to answer your very good, and sometimes very hard, questions. I also want to thank IMC's Doctoral Researchers Cecilia Agamah and Sobia Rashid for the interesting discussions in the lab. Also, thanks to all past members of IMC. Good luck to you all!

Still on the academia side, apart from the whole staff of the department, special mentions go to fellow Doctoral Researchers Ashwini Jadhav, Sachin Kochrekar, Adefunke Koyejo, Majid Al-waeel, and Vinh Nguyen, the next big names in the world of materials chemistry! Aurum's boars Ali Tuna, Randa Mahran and physical chemistry wizard Gabriela Rizzo Piton, who we lost to the academia in Germany, also deserve praises, and also Bioorganic Group's Lange Saleh who I always have great discussions with, as with the next stars of natural chemistry: Dr. Marianna

Manninen, Doctoral Researchers Mimosa Sillanpää, Valtteri Virtanen, Niko Luntamo, Suvi Vanhakylä, and Ilari Kuukkanen. One of the current stars, Prof. Juha-Pekka Salminen, also deserves special mention for his good spirit and the Nokia cellphones he donated to me, a gadget geek.

Thanks also to another NCRG's star Adj. Prof. Maarit Karonen who runs our @chemistry_utu Instagram profile with the gang including Dr. Päivi Poijärvi-Virta, Sachin, Prof. Juha-Pekka, Prof. Pasi Virta, Dr. Veli-Matti Vesterinen, Reetta Rantakokko, and Hilla Nieminen for their work for the Chemistry Dept's Instagram account. We're a good team!

The thanks that cannot be delivered to the person are for Adj. Prof. Jari Sinkkonen who we lost in the beginning of this year very suddenly. We always had interesting discussions when he was around. I think the majority will agree with me when I say that I will remember Jari's work, expertise, teaching, and kind character forever.

Although my use of Chinese has reduced over the years to just simple sentences in basic interactions, I want to thank my Chinese teacher 朱文黎 who has taught me everything about the language and has been there for me and asking about my PhD path regularly. I know that the knowledge of Chinese has not been in vain.

Without Prof. Tangui Le Bahers' and Dr. Pauline Colinet's computational chemistry contribution my articles would have been mere lab reports with a very weak scientific backbone, so thank you both for the valuable work. Thanks to Dr. Jörg Göttlicher, Dr. Ralph Steininger, and Dr. Thomas Spangenberg, who hosted me at the Karlsruhe Institute of Technology's synchrotron facility in Germany and operated the most complex measurement setup I have ever witnessed. Moreover, the scientific impact of my articles would have been very low without the help of various important people who contributed to the articles: Prof. Petriina Paturi, Dr. Heikki Palonen, and Ermei Mäkilä from the Department of Physics and Astronomy of the University of Turku, Prof. Lucas C. V. Rodrigues from Department of Fundamental Chemistry of the University of São Paulo, Brazil, Prof. Timo Saarinen from the Department of Geography and Geology, University of Turku, Adj. Prof. Pekka Laukkanen and Juha-Pekka Lehtiö from the Department of Physics and Astronomy, University of Turku, Prof. Laeticia Petit and Dr. Arnaud Lemiere from the Photonics Laboratory, Tampere University, Micael Granström, Dr. Niklas Brännström, and Göran Ågren from FOI, Swedish Defence Research Agency, Sweden, Prof. Anu J. Airaksinen and Researcher Johan Rajander from the Turku PET Centre, University of Turku, Adj. Prof. Jari Konu from the Department of Chemistry, University of Jyväskylä, Dr. Ludo Van Goethem from the Mineralogical Society of Antwerp, Belgium, Dr. Robin De Meyer and Dr. Nick Schrijvers from EMAT, Antwerp University, Belgium, Dr. Jussi Huikari and Panu Pousi from STUK – Finnish Radiation and Nuclear Safety Authority, Dr. Wenwen Fang, Emma Sairanen, Dr.

Marja Rissanen, and Prof. Herbert Sixta from Aalto University, Dr. Turkka Salminen from Tampere Microscopy Center, Markus Mäkelä, Jouni Rahkola, and Matti Rahkola from Hilamet Oy, Ylihärmä, and Shukri Mahamuud from the Vocational Institute of Turku. More people to thank for interesting collaboration are Dr. Agnieszka Suliga and Dr. Adrian Tighe from the European Space Agency, Dr. Harri Härmä, Adj. Prof. Petri Tähtinen, Hanni Haapsaari and Tytti Taipale from our department, Dr. Kati Laakso and Dr. Miradije Rama from the Geological Survey of Finland GTK, Prof. Kati Miettunen and Alicja Ławrynowicz from the University of Turku's Materials Engineering department, Zahra "Elmira" Jahanshah Rad and Masoud Ebrahimzadeh from the Department of Physics and Astronomy, Dr. Hellen Santos from the Materials Chemistry department of the University of Oulu, Nellie Inkinen from Pure Luminescence Technologies Oy, Anssi Kähkönen from the Department of Economics, Prof. Mark Weller from Cardiff, UK, Prof. Henrik Friis from the Norwegian Center for Mineralogy, Norway, Prof. Esa Heilimo from the Department of Geography and Geology, University of Turku, and Harri Sahinaho and Carl-Erik Guttormsen from Colombier Finland Oy. Thank you all so much.

During my PhD studies I've been the Board Secretary of the Chemist Club of Turku. Being in that position has taught me a lot about time management (where I still am very bad at) and working as a member of the board. Thanks to Dr. Milla Leppä who introduced me to the board in 2019, and thanks to the current and past members Adj. Prof. Petri Tähtinen, Dr. Tero Laihinen, Dr. Meeri Käkelä, Dr. Olli Martiskainen, Timka Lyyra, Tomi Peltonen, Salla Lahti, Joona Anttila, Jussi Suvanto, and the current chairperson Riina Suntioinen.

My family has had a major part in making this whole journey happen. I have spent nine years at the university, throughout which I have received bags of support from my family. Thanks go especially to mom Jenni and dad Tomi who have had a huge role in my life, just like my grandparents Reijo, Marjatta, Harry & Pirjo who paved the road for us. Thanks also to my siblings and their families: Essi, 艺博, Harri, Joni, and Maria, and to my godparents Nanna and Kai and their families. Your support is much appreciated, thanks for everything during these years.

My friends 凯 and Jesse have been good company especially during the rare free time that I've had during my studies. It's always nice to go to hang out with these guys. As is visiting Anton, Outi, and Nani. Miika & Pete, you've kept me in shape with the crushing peer pressure of going to a grill every now and then. Thanks to all the active members of the various groups and forums for interesting daily discussions. Greetings especially to my VOLVO mate Samuli, who also belongs to our original Pepsi & mämmi & runebergintorttu tasting gang with Tommi, Jaakko, Risto, and Laura. Petrus and of course Oliver, your impact has also been very high in my life. Maria and Matias, it has been and will be important that we keep our annual SOPP run so that we see each other at least once a year. As is the annual cabin

weekend in Valkeakoski with people who share a mutual interest in video games, retro computing, and drinking beer. And speaking of leisure trips during the PhD program: Raija, Maija & Tiina, and Carol, what would a trip to Lappeenranta be without meeting you? Katja, Mika, Pasi, Veera, Esa, Päivi, and Markku, thanks for meeting and hosting us whenever we decided to take an *ex tempore* trip near you. And speaking of travelling, greetings to Antti, Jali, Luukas, Sanu, and Mohammed who I shared a small trip with to Shenzhen, China. Thanks also to my contacts who have been supporting me and/or being very helpful with providing procrastination content reels every now and then on IG: Ilkka, Petra, Joakim, Jaana, Christoffer, Jenni, Fanni, Jesse, Pirkko, Katrina, Rizgar, Mirva, Linda, Marco, Kenneth, Suvi-Tuuli, Tarja, Matti, Suvisaara, Marika, Maija, Katja, Pyry, Simo, Lassi, Henna, Salla, Birgitta, Milla, Jorma, Emilia, Aleksi, Sirpa & Tapsa, Seppo, Päivi, Saara, Anu, Anna, Enni, Ibrahim, Jessica, Janita, Jenni, Jorma, Juho, Juuso, Katri, Khalil, Tarek, Krista, Linda, Lucy, Maiju, Teija, Matti, Sami, Virpi, Sara, Jani, Timo, Katja, Veeti, Raimo, Markus, and Sophie. Thanks to our dogs Herkku and Prada for their invaluable, pawsome help. Thanks also to Painosalama Oy's Tomi, Tero, and Kari for their work on the printing side. And thanks to everyone I forgot to mention.

Last, I want to thank Sonja, a person who I met in 2014 when I had just started studying at the university. After all these uncountable years she is still tolerating my busy schedule and crazy ideas and projects. And thanks to Reetta, Kaisa, Susanna, and Osku for keeping her sane with occasional hang-out nights during this process.

I want to thank the Academy of Finland (project GlowTrack), Business Finland (project #6479/31/2019), the European Space Agency, Finnish Chemical Society SKS, and the Finnish Natural Resources Research Foundation (project Soda-lights) for their direct financial support for my PhD studies. The financial and other support of the Academy of Finland (Flagship Programme, Photonics Research and Innovation PREIN-320165), the SYSPROD project, Axelera – Pôle de Compétitivité (PSMN Data Center), the HPC resources of CINES, IDRIS, and TGCC under the allocation 2018–080609 made by GENCI, the French National Research Agency ANR 8 (TeneMod project ANR-17-CE29-0007-21), the Centre Blaise Pascal's IT test platform at ENS de Lyon for its facilities (he platform operates the SIDUS solution developed by Emmanuel Quemener), the FAPESP – São Paulo Research Foundation (project #2018/05280-5), CNPEM for providing the beamtime at the TGM beamline of LNLS (#20180001), Jenny and Antti Wihuri Foundation are also very much appreciated for enabling the data acquisition for the research articles.

...or is this just the beginning?

15.5.2023
Sami Vuori
Paimio

List of References

[1] T. E. Warner, J. H. Andersen, "The effects of sulfur intercalation on the optical properties of artificial “hackmanite”, $Na_8[Al_6Si_6O_{24}]Cl_{1.8}S_{0.1}$; “sulfosodalite”, $Na_8[Al_6Si_6O_{24}]S$; and natural tugtupite, $Na_8[Be_2Al_2Si_8O_{24}](Cl,S)_{2-\delta}$", *Phys Chem Miner*. **39** (2012) 163–168.

[2] L. H. Borgström, "Mineralogiska Notiser", *Mineralogiska Notiser*. **23** (1901) 557–566.

[3] C. Agamah, S. Vuori, P. Colinet, I. Norrbo, J.M. de Carvalho, L.K. Okada Nakamura, J. Lindblom, L. Van Goethem, A. Emmermann, T. Saarinen, T. Laihinen, E. Laakkonen, J. Lindén, J. Konu, H. Vrielinck, D. Van der Heggen, P.F. Smet, T. Le Bahers, M. Lastusaari, "Hackmanite—The Natural Glow-in-the-Dark Material", *Chemistry of Materials*. **32** (2020) 8895–8905.

[4] N. F. Cano, A. R. Blak, S. Watanabe, "Correlation between electron paramagnetic resonance and thermoluminescence in natural sodalite", *Phys Chem Miner*. **37** (2010) 57–64.

[5] R. C. Peterson, "The structure of hackmanite, a variety of sodalite, from Mont St-Hilaire, Quebec", *The Canadian Mineralogist*. **21** (1983) 549–552.

[6] E. R. Williams, A. Simmonds, J. A. Armstrong, M. T. Weller, "Compositional and structural control of tenebrescence", *J Mater Chem*. **20** (2010) 10883–10887.

[7] D. Taylor, "The sodalite group of minerals", *Contributions to Mineralogy and Petrology*. **16** (1967) 172–188.

[8] D. B. Medved, "Hackmanite and its tenebrescent properties", *American Mineralogist*. **39** (1954) 615–629.

[9] R. D. Kirk, "The luminescence and tenebrescence of natural and synthetic sodalite", *American Mineralogist*. **40** (1955) 22–31.

[10] R. D. Kirk, "Role of Sulfur in the Luminescence and Coloration of Some Aluminosilicates", *J Electrochem Soc*. **101** (1954) 461–465.

[11] C. Z. van Doorn, D. J. Schipper, P. T. Bolwijn, "Optical Investigation of Cathodochromic Sodalite", *Journal of Electrochemical Society*. (1972) 85–92.

[12] E. F. Williams, W. G. Hodgson, J. S. Brinen, "Synthetic Photochromic Sodalite", *Journal of the American Ceramic Society*. **52** (1969) 139–144.

[13] T. Takeda, A. Watanabe, "Optically Erasable Cathodochromic Coloration in Sodalites Containing Sulfate", *J Electrochem Soc*. **120** (1973) 1414.

[14] J. A. Armstrong, M. T. Weller, "Structural observation of photochromism", *Chemical Communications*. (2006) 1094–1096.

[15] T. Zahoransky, H. Friis, M. A. W. Marks, "Luminescence and tenebrescence of natural sodalites: a chemical and structural study", *Phys Chem Miner*. **43** (2016) 459–480.

[16] H. Byron, I. Norrbo, M. Lastusaari, "A zeolite-free synthesis of luminescent and photochromic hackmanites", *J Alloys Compd*. **872** (2021) 159671.

[17] I. Norrbo, P. Gluchowski, P. Paturi, J. Sinkkonen, M. Lastusaari, "Persistent luminescence of Tenebrescent $Na_8Al_6Si_6O_{24}(Cl,S)_2$: multifunctional optical markers", *Inorg Chem*. **54** (2015) 7717–7724.

[18] I. Norrbo, P. Gluchowski, I. Hyppänen, T. Laihinen, P. Laukkanen, J. Mäkelä, F. Mamedov, H. S. Santos, J. Sinkkonen, M. Tuomisto, A. Viinikanoja, M. Lastusaari, "Mechanisms of

Tenebrescence and Persistent Luminescence in Synthetic Hackmanite $Na_8Al_6Si_6O_{24}(Cl,S)_2$", *ACS Appl Mater Interfaces*. **8** (2016) 11592–11602.

[19] I. Norrbo, A. Curutchet, A. Kuusisto, J. Mäkelä, P. Laukkanen, P. Paturi, T. Laihinen, J. Sinkkonen, E. Wetterskog, F. Mamedov, T. Le Bahers, M. Lastusaari, "Solar UV index and UV dose determination with photochromic hackmanites: From the assessment of the fundamental properties to the device", *Mater Horiz*. **5** (2018).

[20] I. Norrbo, J.M. Carvalho, P. Laukkanen, J. Mäkelä, F. Mamedov, M. Peurla, H. Helminen, S. Pihlasalo, H. Härmä, J. Sinkkonen, M. Lastusaari, "Lanthanide and Heavy Metal Free Long White Persistent Luminescence from Ti Doped Li–Hackmanite: A Versatile, Low-Cost Material", *Adv Funct Mater*. **27** (2017) 1606547.

[21] P. Colinet, H. Byron, S. Vuori, J.-P. Lehtiö, P. Laukkanen, L. Van Goethem, M. Lastusaari, T. Le Bahers, "The structural origin of the efficient photochromism in natural minerals", *Proc Natl Acad Sci U S A*. **119** (2022) e2202487119.

[22] W. Fang, E. Sairanen, S. Vuori, M. Rissanen, I. Norrbo, M. Lastusaari, H. Sixta, "UV-Sensing Cellulose Fibers Manufactured by Direct Incorporation of Photochromic Minerals", *ACS Sustain Chem Eng*. **9** (2021) 16338–16346.

[23] A. Curutchet, T. Le Bahers, "Modeling the Photochromism of S-Doped Sodalites Using DFT, TD-DFT, and SAC-CI Methods", *Inorg Chem*. **56** (2017) 414–423.

[24] P. Colinet, A. Gheeraert, A. Curutchet, T. Le Bahers, "On the Spectroscopic Modeling of Localized Defects in Sodalites by TD-DFT", *Journal of Physical Chemistry C*. **124** (2020) 8949–8957.

[25] L. T. Todd, E. F. Farrell, Process for preparing cathodochromic sodalite, 1974.

[26] M. Kaiheriman, A. Maimaitinaisier, A. Rehiman, Aierken Sidike, "Photoluminescence properties of green and red luminescence from natural and heat-treated sodalite", *Phys Chem Miner*. **41** (2014) 227–235.

[27] T. E. Warner, Artificial Hackmanite $Na_8[Al_6Si_6O_{24}]Cl_{1.8}S_{0.1}$ by a Structure-Conversion Method with Annealing Under a Reducing Atmosphere, in: Synthesis, Properties and Mineralogy of Important Inorganic Materials, John Wiley & Sons, Ltd, 2011: pp. 240–253. https://onlinelibrary.wiley.com/doi/abs/10.1002/9780470976012.ch16.

[28] J. Goettlicher, A. Kotelnikov, N. Suk, A. Kovalski, T. Vitova, R. Steininger, "Sulfur K X-ray absorption near edge structure spectroscopy on the photochrome sodalite variety hackmanite", **228** (2013) 157–171.

[29] W. Phillips, "Properties of Cathodochromic Sodalite", *Journal of Electrochemical Society*. (1970) 1557–1561.

[30] I. F. Chang, "Synthesis of Photochromic and Cathodochromic Sodalite", *J Electrochem Soc*. **121** (1974) 815.

[31] O. I. Lee, "A new property of matter: Reversible photosensitivity in hackmanite from Bancroft, Ontario", *American Mineralogist*. **21** (1936) 764–776.

[32] R. J. Borg, G. J. Dienes, An Introduction to Solid State Diffusion, Academic Press, Inc., London, UK, 1988.

[33] V. Raghavan, Solid state phase transformations, 4th ed., Asoke K. Ghosh, PHI Learning Private Limited, Delhi, India, 2015.

[34] E. J. Mittemeijer, F. Sommer, "Solid state phase transformation kinetics: a modular transformation model", *International Journal of Materials Research*. **93** (2022) 352–361.

[35] F. Liu, F. Sommer, C. Bos, E. J. Mittemeijer, "Analysis of solid state phase transformation kinetics: models and recipes", *International Materials Reviews*. **52** (2013) 193–212.

[36] H. J. Meyer, "Solid state metathesis reactions as a conceptual tool in the synthesis of new materials", *Dalton Transactions*. **39** (2010) 5973–5982.

[37] I. P. Parkin, "Solid state metathesis reaction for metal borides, silicides, pnictides and chalcogenides: ionic or elemental pathways", *Chem Soc Rev*. **25** (1996) 199–207.

[38] R. Merkle, J. Maier, "On the Tammann–Rule", *Z Anorg Allg Chem*. **631** (2005) 1163–1166.

[39] G. Grube, "Lehrbuch der Metallographie. Chemie und Physik der Metalle und ihrer Legierungen. Von Gustav Tammann. Dritte erweiterte Auflage. XVIII und 450 Seiten mit 249 Figuren. Verlag von Leopold Voß, Leipzig 1923.", *Zeitschrift Für Elektrochemie Und Angewandte Physikalische Chemie*. **30** (1924) 46–47.

[40] A. A. Barde, J. F. Klausner, R. Mei, "Solid state reaction kinetics of iron oxide reduction using hydrogen as a reducing agent", *Int J Hydrogen Energy*. **41** (2016) 10103–10119.

[41] P. Halli, P. Taskinen, R.H. Eriç, "Mechanisms and Kinetics of Solid State Reduction of Titano Magnetite Ore with Methane", *Journal of Sustainable Metallurgy*. **3** (2017) 191–206.

[42] M. Elzohiery, H. Y. Sohn, Y. Mohassab, "Kinetics of Hydrogen Reduction of Magnetite Concentrate Particles in Solid State Relevant to Flash Ironmaking", *Steel Res Int*. **88** (2017) 1600133.

[43] J. V. Badding, "High-pressure synthesis, characterization, and tuning of solid state materials", *Annual Review of Materials Science*. **28** (2003) 631–658.

[44] V. C. Bastron, H. G. Drickamer, "Solid state reactions in organic crystals at very high pressure", *J Solid State Chem*. **3** (1971) 550–563.

[45] E. R. Winkler, J. F. Sarver, I. B. Cutler, "Solid Solution of Titanium Dioxide in Aluminum Oxide", *Journal of the American Ceramic Society*. **49** (1966) 634–637.

[46] N. J. Welham, "Mechanical activation of the solid-state reaction between Al and TiO_2", *Materials Science and Engineering: A*. **255** (1998) 81–89.

[47] W. D. McKee, E. Aleshin, "Aluminum Oxide-Titanium Oxide Solid Solution", *Journal of the American Ceramic Society*. **46** (1963) 54–58.

[48] R. Tällberg, B. P. Jelle, R. Loonen, T. Gao, M. Hamdy, "Comparison of the energy saving potential of adaptive and controllable smart windows: A state-of-the-art review and simulation studies of thermochromic, photochromic and electrochromic technologies", *Solar Energy Materials and Solar Cells*. **200** (2019) 109828.

[49] Y. Li, K. Li, B. Z. Tang, "A photoactivatable photochromic system serves as a self-hidden information storage material", *Mater Chem Front*. **1** (2017) 2356–2359.

[50] M. Hočevar, U. Opara Krašovec, "A photochromic single glass pane", *Solar Energy Materials and Solar Cells*. **186** (2018) 111–114.

[51] H. Tian, Y. Feng, "Next step of photochromic switches?", *J Mater Chem*. **18** (2008) 1617–1622.

[52] G. K. Megla, "Optical Properties and Applications of Photochromic Glass", *Applied Optics, Vol. 5, Issue 6, Pp. 945-960*. **5** (1966) 945–960.

[53] G. P. Smith, "Photochromic Silver Halide Glasses", *The Journal of Photographic Science*. **18** (2016) 41–49.

[54] R. J. Araujo, "Photochromism in glasses containing silver halides", *Contemp Phys*. **21** (2006) 77–84.

[55] G. P. Smith, "Photochromic glasses: Properties and applications", *J Mater Sci*. **2** (1967) 139–152.

[56] H. J. Hoffmann, "Photochromic glass", Large-Area Chromogenics: Materials and Devices for Transmittance Control. **10304** (1990) 92–107.

[57] H. Torres-Pierna, D. Ruiz-Molina, C. Roscini, "Highly transparent photochromic films with a tunable and fast solution-like response", *Mater Horiz*. **7** (2020) 2749–2759.

[58] H. M. Garfinkel, "Photochromic Glass by Silver Ion Exchange", *Applied Optics, Vol. 7, Issue 5, Pp. 789-794*. **7** (1968) 789–794.

[59] S. Nigel Corns, S. M. Partington, A. D. Towns, "Industrial organic photochromic dyes", *Coloration Technology*. **125** (2009) 249–261.

[60] R. Pardo, M. Zayat, D. Levy, "Photochromic organic–inorganic hybrid materials", *Chem Soc Rev*. **40** (2011) 672–687.

[61] J. Lü, J. X. Lin, X. L. Zhao, R. Cao, "Photochromic hybrid materials of cucurbituril and polyoxometalates as photocatalysts under visible light", *Chemical Communications*. **48** (2011) 669–671.

[62] M. Zayat, D. Levy, "Photochromic naphthopyrans in sol–gel ormosil coatings", *J Mater Chem*. **13** (2003) 727–730.

[63] Y. Jin, Y. Hu, Y. Fu, L. Chen, G. Ju, Z. Mu, "Reversible colorless-cyan photochromism in Eu^{2+}-doped $Sr_3YNa(PO_4)_3F$ powders", *J Mater Chem C Mater*. **3** (2015) 9435–9443.

[64] Q. Zhang, Y. Zhang, H. Sun, Q. Sun, X. Wang, X. Hao, S. An, "Photoluminescence, photochromism, and reversible luminescence modulation behavior of Sm-doped $Na_{0.5}Bi_{2.5}Nb_2O_9$ ferroelectrics", *J Eur Ceram Soc*. **37** (2017) 955–966.

[65] Y. Jin, Y. Lv, C. Wang, G. Ju, H. Wu, Y. Hu, "Design and control of the coloration degree for photochromic $Sr_3GdNa(PO_4)_3F:Eu^{2+}$ via traps modulation by Ln^{3+} (Ln = Y, La-Sm, Tb-Lu) co-doping", *Sens Actuators B Chem*. **245** (2017) 256–262.

[66] Y. Jin, Y. Hu, L. Yuan, L. Chen, H. Wu, G. Ju, H. Duan, Z. Mu, "Multifunctional near-infrared emitting Cr^{3+}-doped $Mg_4Ga_8Ge_2O_{20}$ particles with long persistent and photostimulated persistent luminescence, and photochromic properties", *J Mater Chem C Mater*. **4** (2016) 6614–6625.

[67] S. Cao, F. Gao, J. Xu, J. Zhu, Q. Chen, Y. Guo, L. Li, J. Liu, T. Gao, E. Pawlikowska, M. Szafran, G. Cheng, "Photochromic effect of transparent lead-free ferroelectric $KSr_2Nb_5O_{15}$ ceramics", *J Eur Ceram Soc*. **39** (2019) 5260–5266.

[68] L. Liu, F. Gao, Y. Zhang, H. Sun, "Dense $KSr_2Nb_5O_{15}$ ceramics with uniform grain size prepared by molten salt synthesis", *J Alloys Compd*. **616** (2014) 293–299.

[69] L. Liu, F. Gao, G. Hu, J. Liu, "Fabrication of $KSr_2Nb_5O_{15}$ particles with high aspect ratio by two-step molten salt synthesis", *Advanced Powder Technology*. **25** (2014) 219–225.

[70] L. Liu, F. Gao, G. Hu, J. Liu, "Effect of excess Nb_2O_5 on the growth behavior of $KSr_2Nb_5O_{15}$ particles by molten salt synthesis", *Powder Technol*. **235** (2013) 806–813.

[71] M. Akiyama, H. Yamada, K. Sakai, "Photochromism enhancement in reduced tridymite $BaMgSiO_4$ by Fe-doping", *Journal of the Ceramic Society of Japan*. **119** (2011) 338–341.

[72] Y. Ren, Z. Yang, Y. Wang, M. Li, J. Qiu, Z. Song, J. Yu, A. Ullah, I. Khan, "Reversible multiplexing for optical information recording, erasing, and reading-out in photochromic $BaMgSiO_4:Bi^{3+}$ luminescence ceramics", *Science China Materials 2020 63:4*. **63** (2020) 582–592.

[73] S. Kamimura, H. Yamada, C. N. Xu, "Purple photochromism in $Sr_2SnO_4:Eu^{3+}$ with layered perovskite-related structure", *Appl Phys Lett*. **102** (2013) 031110.

[74] S. Kamimura, H. Yamada, C. N. Xu, "Photochromic properties in Eu^{3+} doped Sr_2SnO_4", *MRS Online Proceedings Library (OPL)*. **1492** (2013) 111–115.

[75] Y. Zhang, L. Luo, K. Li, W. Li, Y. Hou, "Light-controlled reversible photoluminescence modulation in photochromic $Sr_2SnO_4:Eu^{3+}$", *J Phys D Appl Phys*. **51** (2018) 365102.

[76] G. Ju, Y. Hu, L. Chen, X. Wang, "Photochromism of europium and gadolinium co-doped barium haloapatite", *ECS Solid State Letters*. **1** (2012) R1.

[77] G. Ju, Y. Hu, L. Chen, X. Wang, "Photochromism of rare earth doped barium haloapatite", *J Photochem Photobiol A Chem*. **251** (2013) 100–105.

[78] S. K. Deb, "Optical and photoelectric properties and colour centres in thin films of tungsten oxide", *The Philosophical Magazine: A Journal of Theoretical Experimental and Applied Physics*. **27** (1973) 801–822.

[79] T. H. Fleisch, G. J. Mains, "An XPS study of the UV reduction and photochromism of MoO_3 and WO_3", *J Chem Phys*. **76** (1982) 780.

[80] B. H. Loo, J. N. Yao, H. Dwain Coble, K. Hashimoto, A. Fujishima, "A Raman microprobe study of the electrochromic and photochromic thin films of molybdenum trioxide and tungsten trioxide", *Appl Surf Sci*. **81** (1994) 175–181.

[81] K. Ajito, L. A. Nagahara, D. A. Tryk, K. Hashimoto, A. Fujishima, "Study of the photochromic properties of amorphous MoO_3 films using raman microscopy", *Journal of Physical Chemistry*. **99** (1995) 16383–16388.

[82] J. N. Yao, Y. A. Yang, B. H. Loo, "Enhancement of photochromism and electrochromism in MoO_3/Au and MoO_3/Pt thin films", *Journal of Physical Chemistry B*. **102** (1998) 1856–1860.

[83] H. Miyazaki, T. Matsuura, T. Ota, "Vanadium oxide-based photochromic composite film", *RSC Adv*. **7** (2017) 2388–2391.

[84] Z. Liu, G. Fang, Y. Wang, Y. Bai, K.L. Yao, "Laser-induced colouration of V_2O_5", *J Phys D Appl Phys*. **33** (2000) 2327.

[85] S. Nishio, M. Kakihana, "Evidence for visible light photochromism of V_2O_5", *Chemistry of Materials*. **14** (2002) 3730–3733.

[86] D. K. Diop, L. Simonot, J. Martínez-García, M. Hébert, Y. Lefkir, G. Abadias, P. Guérin, D. Babonneau, N. Destouches, "Spectral and Color Changes of Ag/TiO_2 Photochromic Films Deposited on Diffusing Paper and Transparent Flexible Plastic Substrates", *Appl Spectrosc*. **71** (2017) 1271–1279.

[87] C. Alcober, F. Alvarez, S. A. Bilmes, R. J. Candal, "Photochromic W-TiO_2 membranes", *J Mater Sci Lett*. **21** (2002) 501–504.

[88] R. Kostecki, T. Richardson, F. McLarnon, "Photochemical and Photoelectrochemical Behavior of a Novel TiO_2 / $Ni(OH)_2$ Electrode", *J Electrochem Soc*. **145** (1998) 2380–2385.

[89] L. Pan, Y. Wang, X.J. Wang, H. Y. Qu, J. P. Zhao, Y. Li, A. Gavrilyuk, "Hydrogen photochromism in Nb_2O_5 powders", *Physical Chemistry Chemical Physics*. **16** (2014) 20828–20833.

[90] W. Chen, H. Shen, X. Zhu, Z. Xing, S. Zhang, "Effect of citric acid on structure and photochromic properties of WO_3–TiO_2–ZnO composite films prepared by a sol–gel method", *Ceram Int*. **41** (2015) 12638–12643.

[91] W. Chen, H. Shen, X. Zhu, H. Yao, W. Wang, "Preparation and photochromic properties of PEG-400 assisted WO_3–TiO_2–ZnO composite films", *Ceram Int*. **41** (2015) 14008–14012.

[92] J. A. Armstrong, M. T. Weller, "New sodalite frameworks; synthetic tugtupite and a beryllosilicate framework with a 3 ∶ 1 Si ∶ Be ratio", *Dalton Transactions*. (2006) 2998–3005.

[93] F. Blumentritt, C. Latouche, Y. Morizet, Y. Morizet, M. T. Caldes, S. Jobic, E. Fritsch, "Unravelling the Origin of the Yellow-Orange Luminescence in Natural and Synthetic Scapolites", *Journal of Physical Chemistry Letters*. **11** (2020) 4591–4596.

[94] "The Periodic Table of Endangered Elements - American Chemical Society", (n.d.). https://www.acs.org/greenchemistry/research-innovation/endangered-elements.html (accessed December 6, 2022).

[95] Y. Jin, Y. Hu, Y. Fu, Z. Mu, G. Ju, "Reversible white and light gray photochromism in europium doped Zn_2GeO_4", *Mater Lett*. **134** (2014) 187–189.

[96] J. Ueda, T. Shinoda, S. Tanabe, "Photochromism and near-infrared persistent luminescence in Eu^{2+}-Nd^{3+}-co-doped $CaAl_2O_4$ ceramics", *Optical Materials Express*. **3** (2013) 787–793.

[97] J. Ueda, Y. Zhuang, S. Tanabe, "Photochromism and white long-lasting persistent luminescence in Bi^{3+}-doped $ZnGa_2O_4$ ceramics", *Optical Materials Express*. **2** (2012) 1378–1383.

[98] T.-H. Tsai, H. Takahashi, Z. Wang, "Reversible photochromic effect in natural gemstone sapphires", *Optics Letters, Vol. 47, Issue 22, Pp. 5805-5808*. **47** (2022) 5805–5808.

[99] K. S. Byrne, J. D. Anstie, J. G. Chapman, A. N. Luiten, "Optically reversible photochromism in natural pink diamond", *Diam Relat Mater*. **30** (2012) 31–36.

[100] K. S. Byrne, J. G. Chapman, A. N. Luiten, "Photochromic charge transfer processes in natural pink and brown diamonds", *J Phys Condens Matter*. **26** (2014) 35501.

[101] Y. Badour, V. Jubera, I. Andron, C. Frayret, M. Gaudon, "Photochromism in inorganic crystallised compounds", *Optical Materials: X*. **12** (2021) 100110.

[102] K. Matsunaga, N. Narita, I. Tanaka, H. Adachi, "Electronic States of F-Centers in Alkali Halide Crystals", *Journal of the Physical Society of Japan*. **65** (2013) 2564–2570.

[103] S. J. Koppal, Lambertian Reflectance, in: Computer Vision, Springer, Boston, MA, 2014: pp. 441–443.
[104] A. Smakula, "Über Erregung und Entfärbung lichtelektrisch leitender Alkalihalogenide", *Zeitschrift Für Physik*. **59** (1930) 603–614.
[105] M. Lax, The Influence of Lattice Vibrations on Electronic Transitions in Solids, Syracuse, NY, US, 1954. https://apps.dtic.mil/sti/citations/AD0043570 (accessed January 3, 2023).
[106] W. E. van den Brom, J. Kerssen, J. Volger, "Electric dipole centres and colour centres in natural sodalite", *Physica*. **77** (1974) 1–26.
[107] W. Nakel, "The elementary process of bremsstrahlung", *Phys Rep*. **243** (1994) 317–353.
[108] G. D. Considine, P. H. Kulik, Van Nostrand's Scientific Encyclopedia, 9th ed., John Wiley & Sons Inc., New York, USA, 2002.
[109] P. Carenza, T. Fischer, M. Giannotti, G. Guo, G. Martínez-Pinedo, A. Mirizzi, "Improved axion emissivity from a supernova via nucleon-nucleon bremsstrahlung", *Journal of Cosmology and Astroparticle Physics*. **2019** (2019) 016.
[110] J. Vink, "Non-thermal bremsstrahlung from supernova remnants and the effect of Coulomb losses", *Astron Astrophys*. **486** (2008) 837–841.
[111] P. P. Dendy, B. Heaton, Physics for Diagnostic Radiology, 2nd ed., Taylor & Francis Group, LLC, New York, USA, 1999.
[112] J. Kónya, N. M. Nagy, Chapter 5 - Interaction of Radiation With Matter, in: J. Kónya, N.M. Nagy (Eds.), Elsevier, 2018: pp. 85–131.
[113] M. F. L'Annunziata, Radioactivity: Introduction and History, 1st ed., Elsevier Science, Amsterdam, Netherlands, 2007.
[114] G. F. Knoll, Radiation Detection and Measurement, 3rd ed., John Wiley & Sons, Inc., New York, USA, 2000.
[115] E. Rutherford, "VIII. Uranium radiation and the electrical conduction produced by it", *The London, Edinburgh, and Dublin Philosophical Magazine and Journal of Science*. **47** (1899) 109–163.
[116] H. Bichsel, D. H. Peirson, J. W. Boring, A. Green, M. Inokuti, G. Hurst, ICRU Report 31: Average Energy Required to Produce An Ion Pair, 1979.
[117] E. Fourkal, A. Nahum, C.-M. C. Ma, K. Paskalev, "Average energy required to produce an ion pair, revisited", *Plasma Physics*. (2017).
[118] M. J. Berger, J. H. Hubbell, S. M. Seltzer, J. Chang, J. S. Coursey, R. Sukumar, D.S. Zucker, K. Olsen, "NIST XCOM", *NIST*. (2010). https://physics.nist.gov/PhysRefData/Xcom/html/xcom1.html (accessed January 23, 2023).
[119] J. A. Bearden, A. F. Burr, "Reevaluation of X-Ray Atomic Energy Levels", *Rev Mod Phys*. **39** (1967) 125.
[120] J. A. Seibert, J. M. Boone, "X-ray imaging physics for nuclear medicine technologists. Part 2: X-ray interactions and image formation", *J Nucl Med Technol*. **33** (2005) 3–18.
[121] J. T. Bushberg, J. A. Seibert, E. M. Leidholdt, J. M. Boone, The essential physics of medical imaging, 2nd ed., Lippincott Williams & Wilkins, Philadelphia, USA, 2002.
[122] W. Huda, R. M. Slone, Review of Radiologic Physics, 2nd ed., Lippincott Williams & Wilkins, Philadelphia, USA, 2003.
[123] J. W. Poston, "Dosimetry", *Encyclopedia of Physical Science and Technology*. (2003) 603–650.
[124] S. N. Ahmed, Physics and Engineering of Radiation Detection, in: S.N. Ahmed (Ed.), Elsevier, 2015: pp. 1–64. http://www.sciencedirect.com/science/article/pii/B9780128013632000012.
[125] D. S. McGregor, "Materials for Gamma-Ray Spectrometers: Inorganic Scintillators", *Annu Rev Mater Res*. **48** (2018) 245–277.
[126] F. Wilkinson, "Scintillators", *Emission Tomography: The Fundamentals of PET and SPECT*. (2004) 229–254.

[127] M. J. Weber, "Scintillation: mechanisms and new crystals", *Nucl Instrum Methods Phys Res A*. **527** (2004) 9–14.

[128] A. Rogalev, J. Goulon, X-Ray Excited Optical Luminescence Spectroscopies, in: T.-K. Sham (Ed.), Chemical Applications of Synchrotron Radiation, 12th ed., World Scientific, 2002: p. 736.

[129] P. W. Frame, "A history of radiation detection intrumentation", *Health Phys*. **87** (2004) 111–135.

[130] P. D. Holt, "The Response of Photographic Film Dosemeters to High Energy Gamma Radiation", *Phys Med Biol*. **10** (1965) 345.

[131] D. Richter, H. Dombrowski, S. Neumaier, P. Guibert, A.C. Zink, "Environmental gamma dosimetry with OSL of α-Al_2O_3:C for in situ sediment measurements", *Radiat Prot Dosimetry*. **141** (2010) 27–35.

[132] E. G. Yukihara, G. Mardirossian, M. Mirzasadeghi, S. Guduru, S. Ahmad, "Evaluation of Al_2O_3:C optically stimulated luminescence (OSL) dosimeters for passive dosimetry of high-energy photon and electron beams in radiotherapy", *Med Phys*. **35** (2008) 260–269.

[133] S. Bahl, V. Kumar, R. R. Bihari, P. Kumar, "Investigations of OSL properties of $CaSO_4$:Mn phosphor exposed to gamma and beta radiations", *J Lumin*. **181** (2017) 36–43.

[134] P. L. Antonio, C. C. Gronchi, R. A. P. Oliveira, H. J. Khoury, L. V. E. Caldas, "TL and OSL dosimetric properties of Opal gemstone for gamma radiation dosimetry", *Radiat Meas*. **90** (2016) 219–223.

[135] R. A. P. O. D'Amorim, D. A. A. de Vasconcelos, V. S. M. de Barros, H. J. Khoury, S. O. Souza, "Characterization of α-spodumene to OSL dosimetry", *Radiation Physics and Chemistry*. **95** (2014) 141–144.

[136] T. Rivera, J. Azorín, C. Furetta, C. Falcony, M. García, E. Martínez, "Green stimulated luminescence of ZrO_2 + PTFE to UV radiation dosimetry", *Nucl Instrum Methods Phys Res B*. **213** (2004) 325–328.

[137] G. V. M. Williams, C. Dotzler, A. Edgar, S. G. Raymond, "Ultraviolet induced absorption and Bragg grating inscription in $RbCdF_3:Mn^{2+}$", *J Appl Phys*. **102** (2007) 113106.

[138] F. Smetana, M. Hajek, R. Bergmann, H. Brusl, M. Fugger, W. Gratzl, E. Kitz, N. Vana, "A portable multi-purpose OSL reader for UV dosimetry at workplaces", *Radiat Meas*. **43** (2008) 516–519.

[139] V. K. Mathur, J. Gasiot, R. J. Abbundi, M. D. Brown, "Optically Stimulated Luminescence in MgS:Ce,Sm", *Radiat Prot Dosimetry*. **17** (1986) 333–336.

[140] R. Pérez Salas, R. Aceves, R. Meléndrez, M. Barboza-Flores, L. P. Pashchenko, "Ultraviolet dosimetric properties of α-Al_2O_3 crystals", *Appl Phys Lett*. **63** (1993) 894.

[141] S. P. Barghare, R. V. Joshi, T. R. Joshi, S. P. Kathuria, "Intrinsic thermoluminescence of NaCl:Tl in UV dosimetry", *Radiat Eff*. **66** (1982) 217–222.

[142] A. V. Gektin, I. M. Krasovitskaya, N. V. Shiran, "UV-dosimetric material based on $KMgF_3$ perovskite", *Radiat Meas*. **29** (1998) 337–340.

[143] H. C. Wulf, M. Gniadecka, "CaF_2:Dy and CaF_2 crystal-based UV dosimeters", *Skin Research and Technology*. **2** (1996) 108–113.

[144] M. Benabdesselam, P. Iacconi, L. Trinkler, B. Berzina, "Potential application of some wide band gap materials for UV dosimetry", *Physica Status Solidi (c)*. **2** (2005) 539–542.

[145] R. K. Tamrakar, D. P. Bisen, I. P. Sahu, N. Brahme, "UV and gamma ray induced thermoluminescence properties of cubic $Gd_2O_3:Er^{3+}$ phosphor", *J Radiat Res Appl Sci*. **7** (2014) 417–429.

[146] M. Chandrasekhar, D. V. Sunitha, N. Dhananjaya, H. Nagabhushana, S. C. Sharma, B. M. Nagabhushana, C. Shivakumara, R. P. S. Chakradhar, "Thermoluminescence response in gamma and UV irradiated Dy_2O_3 nanophosphor", *J Lumin*. **132** (2012) 1798–1806.

[147] G. Sharma, S. P. Lochab, N. Singh, "Thermoluminescence characteristics of gamma irradiated CaS:Ce nanophosphors", *J Alloys Compd*. **501** (2010) 190–192.

[148] J. M. Kalita, M. L. Chithambo, "On the sensitivity of thermally and optically stimulated luminescence of α-Al_2O_3:C and α-Al_2O_3:C,Mg", *Radiat Meas*. **99** (2017) 18–24.
[149] N. M. Trindade, L. G. Jacobsohn, "Thermoluminescence and radioluminescence of α-Al_2O_3:C,Mg at high temperatures", *J Lumin*. **204** (2018) 598–602.
[150] J. M. Kalita, M. L. Chithambo, "Thermoluminescence of α-Al_2O_3:C,Mg: Kinetic analysis of the main glow peak", *J Lumin*. **182** (2017) 177–182.
[151] J. M. Kalita, M. L. Chithambo, "The effect of annealing and beta irradiation on thermoluminescence spectra of α-Al_2O_3:C,Mg", *J Lumin*. **196** (2018) 195–200.
[152] M. S. Akselrod, R. C. Yoder, G. M. Akselrod, "Confocal fluorescent imaging of tracks from heavy charged particles utilising new Al_2O_3:C,Mg crystals", *Radiat Prot Dosimetry*. **119** (2006) 357–362.
[153] M. S. Akselrod, G. J. Sykora, "Fluorescent nuclear track detector technology – A new way to do passive solid state dosimetry", *Radiat Meas*. **46** (2011) 1671–1679.
[154] M. Mahesh, "Fluoroscopy: Patient Radiation Exposure Issues", *RadioGraphics*. **21** (2001) 1033–1045.
[155] S. K. Carlson, C. E. Bender, K. L. Classic, F. E. Zink, J. P. Quam, E. M. Ward, A. L. Oberg, "Benefits and Safety of CT Fluoroscopy in Interventional Radiologic Procedures1", *Radiology*. **219** (2001) 515–520.
[156] T. B. Shope, "Radiation-induced skin injuries from fluoroscopy", *RadioGraphics*. **16** (1996) 1195–1199.
[157] H. T. Benzon, T. P. Maus, H. R. Kang, D. A. Provenzano, A. Bhatia, F. Diehn, A. Nelson, Z. L. McCormick, B. P. Liu, J. De Andres Ares, M. Anitescu, K. Blackham, A. Bhaskar, S. Brill, J. Collins, A. Gulve, R. W. Hurley, Y. H. Jeon, J. Y. Moon, R. L. Rauck, M. Rodes, R. K. Lee, V. Shah, H. Shanthanna, J. Van Zundert, M. Huntoon, J. P. Rathmell, M. S. Borges, S. P. Cohen, P. A. Greenberger, "The Use of Contrast Agents in Interventional Pain Procedures: A Multispecialty and Multisociety Practice Advisory on Nephrogenic Systemic Fibrosis, Gadolinium Deposition in the Brain, Encephalopathy After Unintentional Intrathecal Gadolinium Injection, and Hypersensitivity Reactions", *Anesth Analg*. **133** (2021) 535–552.
[158] M. V. Spampinato, A. Abid, M. G. Matheus, "Current Radiographic Iodinated Contrast Agents", *Magn Reson Imaging Clin N Am*. **25** (2017) 697–704.
[159] J. J. Pasternak, E. E. Williamson, "Clinical pharmacology, uses, and adverse reactions of iodinated contrast agents: a primer for the non-radiologist", *Mayo Clin Proc*. **87** (2012) 390–402.
[160] G. Lutz, Semiconductor Radiation Detectors: Device Physics, 1st ed., Springer-Verlag Berlin Heidelberg, Berlin, 1999.
[161] F.S. Goulding, "Semiconductor detectors for nuclear spectrometry, I*", *Nuclear Instruments and Methods*. **43** (1966) 1–54.
[162] K. M. Wainio, G. F. Knoll, "Calculated gamma ray response characteristics of semiconductor detectors", *Nuclear Instruments and Methods*. **44** (1966) 213–223.
[163] J. M. Hollander, "The impact of semiconductor detectors on gamma-ray and electron spectroscopy", *Nuclear Instruments and Methods*. **43** (1966) 65–109.
[164] G. Steinhauser, K. Buchtela, Gas ionization detectors, in: Handbook of Radioactivity Analysis: Volume 1: Radiation Physics and Detectors, Elsevier, London, 2020: pp. 245–305.
[165] C. G. Soares, "Radiochromic film dosimetry", *Radiat Meas*. **41** (2006) S100–S116.
[166] S. Devic, N. Tomic, D. Lewis, "Reference radiochromic film dosimetry: Review of technical aspects", *Physica Medica*. **32** (2016) 541–556.
[167] S. Devic, "Radiochromic film dosimetry: Past, present, and future", *Physica Medica*. **27** (2011) 122–134.
[168] C. Chen, J.-K. Sun, Y.-J. Zhang, X.-D. Yang, J. Zhang, "Flexible Viologen-Based Porous Framework Showing X-ray Induced Photochromism with Single-Crystal-to-Single-Crystal Transformation.", *Angew Chem Int Ed Engl*. **56** (2017) 14458–14462.

[169] A.-P. Jin, Z.-W. Chen, M.-S. Wang, G.-C. Guo, "[Zn(OOCH)$_2$(4,4′-bipyridine)]$_n$: A metal-organic-framework (MOF) with x-ray-induced photochromic behaviour at room temperature", *Dyes and Pigments*. **163** (2019) 656–659.
[170] S.-L. Li, M. Han, Y. Zhang, G.-P. Li, M. Li, G. He, X.-M. Zhang, "X-ray and UV Dual Photochromism, Thermochromism, Electrochromism, and Amine-Selective Chemochromism in an Anderson-like Zn(7) Cluster-Based 7-Fold Interpenetrated Framework.", *J Am Chem Soc*. **141** (2019) 12663–12672.
[171] H. Zhang, X. Wu, "Calix-Like Metal-Organic Complex for High-Sensitivity X-Ray-Induced Photochromism.", *Adv Sci (Weinh)*. **3** (2016) 1500224.
[172] M.-S. Wang, C. Yang, G.-E. Wang, G. Xu, X.-Y. Lv, Z.-N. Xu, R.-G. Lin, L.-Z. Cai, G.-C. Guo, "A room-temperature X-ray-induced photochromic material for X-ray detection.", *Angew Chem Int Ed Engl*. **51** (2012) 3432–3435.
[173] L. M. Zhang, Y. Kong, R. Zhou, S. F. Yuan, T. Wu, "X-ray photochromism of chalcogenide frameworks linked with metal-amine chelates", *Chemical Communications*. **58** (2022) 13491–13494.
[174] C. Doelter, "Das Radium und die Farben", *Nature*. **85** (1911) 470.
[175] O. Stuhlman, A. F. Daniel, "The X-ray phosphorescent and thermophosphorescenct radiations of kunzite", *J Opt Soc Am*. **17** (1928) 289–293.
[176] F. H. Pough, T. H. Rogers, "Experiments in X-ray irradiation of gem stones", *American Mineralogist*. **32** (1947) 31–43.
[177] T. Santos, T. Ventura, M. do Carmo Lopes, "A review on radiochromic film dosimetry for dose verification in high energy photon beams", *Radiation Physics and Chemistry*. **179** (2021) 109217.
[178] S. Devic, "Radiochromic film dosimetry: Past, present, and future", *Physica Medica*. **27** (2011) 122–134.
[179] S. Devic, N. Tomic, D. Lewis, "Reference radiochromic film dosimetry: Review of technical aspects", *Physica Medica*. **32** (2016) 541–556.
[180] A. Niroomand-Rad, S. T. Chiu-Tsao, M. P. Grams, D. F. Lewis, C. G. Soares, L. J. van Battum, I. J. Das, S. Trichter, M. W. Kissick, G. Massillon-Jl, P. E. Alvarez, M. F. Chan, "Report of AAPM Task Group 235 Radiochromic Film Dosimetry: An Update to TG-55", *Med Phys*. **47** (2020) 5986–6025.
[181] M. J. Butson, P. K. N. Yu, T. Cheung, P. Metcalfe, "Radiochromic film for medical radiation dosimetry", *Materials Science and Engineering: R: Reports*. **41** (2003) 61–120.
[182] W. L. McLaughlin, M. Kosanić, "The gamma-ray response of pararosaniline cyanide dosimeter solutions", *Int J Appl Radiat Isot*. **25** (1974) 249–262.
[183] K. C. Humpherys, W. O. Wilde, A. D. Kantz, "An opti-chromic dosimetry system for radiation processing of food", *Radiation Physics and Chemistry (1977)*. **22** (1983) 291–294.
[184] A. Miller, E. Bjergbakke, W. L. McLaughlin, "Some limitations in the use of plastic and dyed plastic dosimeters", *Int J Appl Radiat Isot*. **26** (1975) 611–620.
[185] W. L. McLaughlin, J. C. Humphreys, H. Levine, A. Miller, B. B. Radak, N. Rativanich, "The gamma-ray response of radiochromic dye films at different absorbed dose rates", *Radiation Physics and Chemistry (1977)*. **18** (1981) 987–999.
[186] W. R. Hendee, "Manual on Radiation Dosimetry", *Radiology*. **99** (1971) 452–452.
[187] P. Casolaro, L. Campajola, G. Breglio, S. Buontempo, M. Consales, A. Cusano, A. Cutolo, F. di Capua, F. Fienga, P. Vaiano, "Real-time dosimetry with radiochromic films", *Scientific Reports 2019 9:1*. **9** (2019) 1–11.
[188] R. L. Cavasso Filho, A. F. Lago, M. G. P. Homem, S. Pilling, A. Naves de Brito, "Delivering high-purity vacuum ultraviolet photons at the Brazilian toroidal grating monochromator (TGM) beamline", *J Electron Spectros Relat Phenomena*. **156–158** (2007) 168–171.
[189] B. Uschold, "KIT IPS - Methods & Facilities - SPECTROSCOPY Cluster", (2022).

[190] R. Dovesi, A. Erba, S. Salustro, B. Kirtman, R. O. C. M. Zicovich-Wilson, B. Civalleri, L. Maschio, M. Rérat, S. Casassa, J. Baima, "Quantum-mechanical condensed matter simulations with CRYSTAL", *WIREs Computational Molecular Science*. **8** (2018) e1360.

[191] C. Adamo, V. Barone, "Toward reliable density functional methods without adjustable parameters: The PBE0 model", *Journal of Chemical Physics*. **110** (1999) 6158–6170.

[192] M. J. Frisch, G. W. Trucks, H. B. Schlegel, G. E. Scuseria, M. A. Robb, J. R. Cheeseman, G. Scalmani, V. Barone, G. A. Petersson, H. Nakatsuji, X. Li, M. Caricato, A. V Marenich, J. Bloino, B. G. Janesko, R. Gomperts, B. Mennucci, H. P. Hratchian, J. V. Ortiz, A. F. Izmaylov, J. L. Sonnenberg, D. Williams-Young, F. Ding, F. Lipparini, F. Egidi, J. Goings, B. Peng, A. Petrone, T. Henderson, D. Ranasinghe, V. G. Zakrzewski, J. Gao, N. Rega, G. Zheng, W. Liang, M. Hada, M. Ehara, K. Toyota, R. Fukuda, J. Hasegawa, M. Ishida, T. Nakajima, Y. Honda, O. Kitao, H. Nakai, T. Vreven, K. Throssell, Montgomery Jr., J. A., J. E. Peralta, F. Ogliaro, M.J. Bearpark, J. J. Heyd, E. N. Brothers, K. N. Kudin, V. N. Staroverov, T. A. Keith, R. Kobayashi, J. Normand, K. Raghavachari, A. P. Rendell, J. C. Burant, S. S. Iyengar, J. Tomasi, M. Cossi, J. M. Millam, M. Klene, C. Adamo, R. Cammi, J. W. Ochterski, R. L. Martin, K. Morokuma, O. Farkas, J. B. Foresman, D. J. Fox, "Gaussian 16", (2016).

[193] M. Klintenberg, S. E. Derenzo, M. J. Weber, "Accurate crystal fields for embedded cluster calculations", *Comput Phys Commun*. **131** (2000) 120–128.

[194] R. Dovesi, C. Roetti, C. Freyria-Fava, M. Prencipe, V. R. Saunders, "On the elastic properties of lithium, sodium and potassium oxide. An ab initio study", *Chem Phys*. **156** (1991) 11–19.

[195] F. Neese, "Software update: the ORCA program system, version 4.0", *WIREs Computational Molecular Science*. **8** (2017) e1327.

[196] F. Neese, "The ORCA program system", *WIREs Computational Molecular Science*. **2** (2012) 73–78.

[197] A. J. Warren, D. Axford, R. L. Owen, "Direct measurement of X-ray-induced heating of microcrystals", *J Synchrotron Radiat*. **26** (2019) 991–997.

[198] A. Kastengren, "Thermal behavior of single-crystal scintillators for high-speed X-ray imaging", *J Synchrotron Radiat*. **26** (2019) 205–214.

[199] H. Wallander, J. Wallentin, "Simulated sample heating from a nanofocused X-ray beam", *J Synchrotron Radiat*. **24** (2017) 925–933.

[200] P. J. R. Montes, M. E. G. Valerio, G. de M. Azevedo, "Radioluminescence and X-ray excited optical luminescence of $SrAl_2O_4$:Eu nanopowders", *Nucl Instrum Methods Phys Res B*. **266** (2008) 2923–2927.

[201] M. V. D. S. Rezende, A. B. Andrade, M. E. G. Valerio, P. J. R. Montes, "The effect of the host composition on the lifetime decay properties of barium/strontium aluminates compounds", *J Appl Phys*. **115** (2014).

[202] M. Oliva-Ramirez, M. MacÍas-Montero, A. Borras, A. R. González-Elipe, "Ripening and recrystallization of NaCl nanocrystals in humid conditions", *RSC Adv*. **6** (2016) 3778–3782.

[203] M. Fleet, X. Liu, S. Harmer-Bassell, P. King, "Sulfur K-edge XANES spectroscopy: Chemical state and content of sulfur in silicate glasses", *The Canadian Mineralogist*. **43** (1605) 1605–1618.

[204] D. Reinen, G.-G. Lindner, "The nature of the chalcogen colour centres in ultramarine-type solids", *Chem Soc Rev*. **28** (1999) 75–84.

[205] E. G. Derouane, M. Mestdagh, L. Vielvoye, "EPR study of the nature and removal of iron(III) impurities in ammonium-exchanged NaY-zeolite", *J Catal*. **33** (1974) 169–175.

[206] E. A. Zhilinskaya, G. Delahay, M. Mauvezin, B. Coq, A. Aboukaïs, "EPR investigation of fe-exchanged beta-zeolites", *Langmuir*. **19** (2003) 3596–3602.

[207] N. Gobeltz-Hautecoeur, A. Demortier, B. Lede, J. P. Lelieur, C. Duhayon, "Occupancy of the sodalite cages in the blue ultramarine pigments", *Inorg Chem*. **41** (2002) 2848–2854.

[208] J. Goslar, S. Lijewski, S. K. Hoffmann, A. Jankowska, S. Kowalak, "Structure and dynamics of S_3^- radicals in ultramarine-type pigment based on zeolite A: Electron spin resonance and electron spin echo studies", *J Chem Phys*. **130** (2009) 204504.
[209] S. W. Faryad, S. Collett, M. Petterson, S.A. Sergeev, "Magmatism and metamorphism linked to the accretion of continental blocks south of the Hindu Kush, Afghanistan", *Lithos*. **175–176** (2013) 302–314.
[210] W. F. Shah, "Metamorphic Conditions and Fluid Compositions of Scapolite-Bearing Rocks from the Lapis Lazuli Deposit at Sare Sang, Afghanistan", *Journal of Petrology*. **43** (2002) 725–747.
[211] H. B. Pascoal, W. M. Pontuschka, H. Rechenberg, "Luminescence quenching by iron in calcium aluminoborate glasses", *J Non Cryst Solids*. **258** (1999) 92–97.
[212] S. M. del Nery, W. M. Pontuschka, S. Isotani, C.G. Rouse, "Luminescence quenching by iron in barium aluminoborate glasses", *Phys Rev B*. **49** (1994) 3760.
[213] M. Gaft, R. Reisfeld, G. Panczer, Modern Luminescence Spectroscopy of Minerals and Materials, Springer, Berlin, 2005.
[214] K. G. Veinot, N. E. Hertel, "Personal dose equivalent conversion coefficients for photons to 1 GeV", *Radiat Prot Dosimetry*. **145** (2011) 28–35.
[215] G. H. Anno, R. W. Young, R. M. Bloom, J. R. Mercier, "Dose response relationships for acute ionizing-radiation lethality", *Health Phys*. **84** (2003) 565–575.
[216] EHSS, The DOE Ionizing Radiation Dose Ranges Chart, 2017.
[217] M. Lacroix, Irradiation of Foods, in: D.-W. Sun (Ed.), Emerging Technologies for Food Processing, Elsevier, Dublin, Ireland, 2005: pp. 353–386.
[218] Kodak Alaris Holdings Limited, "Kodak Alaris Annual Report & Accounts", (2021) 22–22. https://www.kodakalaris.com/getmedia/c920a71f-c9dd-4140-ab56-4c27e7866bc2/FY21-Accounts-Final-and-Signed.pdf.aspx (accessed September 27, 2022).
[219] I. N. Gorokhovskii, T. M. Levenberg, Obshchaia sensitometriia: Teoriia i praktika, 1963.
[220] G. K. Burgess, Scientific Papers of the Bureau of Standards - United States. National Bureau of Standards, Department of Commerce, US, Washington, 1923.

TURUN
YLIOPISTO
UNIVERSITY
OF TURKU

ISBN 978-951-29-9279-9 (PRINT)
ISBN 978-951-29-9280-5 (PDF)
ISSN 0082-7002 (PRINT)
ISSN 2343-3175 (ONLINE)

Painosalama Oy, Turku, Finland 2023